Politecnico di Milano

SCHOOL OF INDUSTRIAL AND INFORMATION ENGINEERING

Master Degree in Engineering Physics

Raman Spectroscopy Using Single-Pixel Time-Domain Single-Photon Counting

Supervisor
Prof. Antonio Giovanni Pifferi

Co-Supervisor
Dr. Pranav Lanka

Candidate
Alessandro Bossi
Matr.920217

Contents

List of Figures

List of Tables

Sommario

La spettroscopia Raman può essere utilizzata per studiare la composizione molecolare di un campione. La conoscenza della composizione molecolare è fondamentale in diversi campi e in clinica.

In questa tesi, abbiamo sviluppato un modello teorico per il Raman nei mezzi diffusivi, costruito uno spettrometro Raman innovativo e finalizzato uno spettrometro Raman diffuso nel dominio del tempo. I due spettrometri utilizzano tecniche nel dominio del tempo per studiare lo scattering Raman utilizzando un rivelatore a singolo pixel. Nel modello teorico, abbiamo studiato la propagazione della luce Raman in un materiale. Abbiamo quindi modellato la propagazione Raman in un materiale a due strati. Abbiamo approssimato il problema e trovato una soluzione analitica. Da questa soluzione troviamo un ritardo temporale dall'istante di arrivo della luce di sondaggio sul primo strato all'istante di uscita del segnale Raman dal materiale.

Il primo spettrometro utilizza una fibra monomodale per separare le diverse lunghezze d'onda. Utilizza la separazione temporale invece della separazione spaziale e ha utilizzato un rilevatore di nanowire superconduttivi. Lo spettrometro costruito ha un intervallo spettrale da 750 a 1100 nm con una risoluzione massima di 1,5 nm. Sono state eseguite diverse misure per testare il sistema e abbiamo anche eseguito alcune misure in vivo. Il secondo è uno spettrometro Raman diffuso nel dominio del tempo e utilizza la separazione temporale del segnale Raman proveniente da diversi strati per ricostruire la profondità originale. Lo spettrometro è stato costruito in lavori precedenti e abbiamo migliorato l'usabilità finalizzando il setup ottico e sviluppando un programma di controllo per un Digital Micromirror Device. Con questo programma e la sincronizzazione del DMD con l'acquisizione del detector, abbiamo migliorato la velocità di allineamento e ridotto i tempi di integrazione.

Lo spettrometro ha una risoluzione spettrale massima di 1,9 nm con un intervallo spettrale di 45 nm in regioni spettrali selezionabili fino a 900 nm. Siamo stati in grado di misurare il segnale Raman del marmo ricoperto da 10 mm di silicone. Abbiamo eseguito alcune misurazioni in vivo.

Abstract

Raman spectroscopy can be used to study the molecular composition of a sample. The knowledge of molecular composition is critical in several fields and in clinics.

In this thesis, we developed a theoretical model for the Raman in diffusive media, built an innovative Raman spectrometer and finalized a time-domain diffuse Raman spectrometer. The two spectrometers use time-domain techniques to study the Raman scattering using a single-pixel detector with Time-Correlated Single Photon Counting.

In the theoretical model, we studied the propagation of the Raman light into a material. We found a different approach to obtain the heuristic approximation. We then modeled the Raman propagation in a two-layer material. We approximated the problem and found an analytical solution. From this solution, we found there is a time delay from the arrival time of the probing light on the first layer to the exit time of the Raman signal.

The first spectrometer we built makes use of a single-mode fiber to separate different wavelengths using temporal separation instead of spatial separation and used a superconductive nanowire detector. The spectrometer built has a spectral range of 750 to 1100 nm with a maximum spectral resolution of 1.5 nm. Several measurements have been performed to test the system and we also performed some in-vivo measurements.

The second one is a time-domain diffuse Raman spectrometer and uses the time separation of Raman signal coming from different layers to reconstruct the original depth. The spectrometer was built in previous works and we improved the usability by finalizing the setup and developing a controlling program for a Digital Micromirror Device (DMD). With this program and the synchronization of the DMD with the acquisition of the detector, we have improved the speed of alignment and resolution of the setup and reduced the integration time. The spectrometer has a maximum spectral resolution of 1.9 nm with a spectral range of 45 nm in selectable wavelength regions up to 900 nm. We have been able to measure the Raman signal of marble covered by 10 mm of silicone. We performed some in-vivo measurements.

Chapter 1

Introduction

Recognizing a material is vital in biology, geology, medicine, security and many other sectors. The use of vibrational spectroscopy allows the detection of a molecular fingerprint of the sample and the chemical composition can be derived.

The study of Raman spectroscopy is commonly limited to the surface of a material without depth probing. However, depth probing with Raman could unlock new frontiers as Raman has several advantages compared to probing techniques commonly used today, firstly the chemical sensitivity. The field that study the propagation of Raman signal in diffusive media is called diffuse Raman.

By using diffuse optical techniques, it is possible to achieve depth probing. In particular, we are interested in biophotonics. We hope in the future new diffuse Raman devices could be developed to be used in clinics, possibly alongside existing depth probing devices that are not chemically sensitive such as magnetic resonance or echography. Today if a doctor needs to understand the chemical composition of a tissue, the only option is a biopsy. A significant advantage of Raman spectroscopy is its non-invasiveness. The doctor will recognize the molecular composition by simply shining a laser light on the patient.

In the introduction, we explain the basics of Raman spectroscopy and diffuse optics. After presenting these two fields, we focus on Diffuse Raman and present some applications that Diffuse Raman hopes to be a significant contributor to in the future.

Our work was focused on time-domain techniques and it is divided into three parts:

- a theoretical part where a model for the propagation of Raman in diffusive media has been developed

- the development of a new Raman spectrometer that uses temporal separation instead of spatial separation

- the finalization of a diffuse Raman spectrometer that uses the temporal distribution for depth probing

1.1   Raman Spectroscopy

Raman spectroscopy is a powerful technique for recognizing a molecular composition of a material. To understand the physics behind Raman spectroscopy, we will need first to introduce some concepts of:

- vibration of the molecules

- elastic scattering

We will then explain what Raman scattering is.

1.1.1   Molecular vibrational levels

A molecule is a collection of atoms held together by chemical bonds. The atoms are formed by protons in the nucleus that are positively charged and electrons that are negatively charged and all the particles will interact with each other with the electromagnetic force. To understand each element's position, movement, and energy, we need to write the Hamiltonian of the system and use a quantum mechanical description to solve the Schrodinger equation.

The Hamiltonian is the sum of the kinetic and potential energy of all the particles' nuclei and electrons. [1] [10]

$$H = V + K = K_{nuclei} + K_{electrons} + V_{N,N} + V_{e,N} + V_{e,e} \qquad (1.1)$$

where K_{nuclei} is the kinetic energy of all the nuclei, $K_{electrons}$ is the kinetic energy of all the electrons, $V_{N,N} = \frac{1}{4\pi\varepsilon_0} \frac{q^2}{|\mathbf{R}_i - \mathbf{R}_j|}$ is the potential energy term for the electromagnetic interaction between the various atom nuclei, $V_{e,N}$ is the electromagnetic interaction between the nuclei and the electrons and $V_{e,e}$ is the electron electron interaction.

the time-independent Schrodinger equation will be

$$H\Phi = \varepsilon\Phi \qquad (1.2)$$

where ε is the energy of the system and Φ is its wave-function. Using the Born - Oppenheimer approximation it is possible to divide the problem for the nuclei and the electrons:

$$
\begin{aligned}
(K_N + V_{eff})\Phi_N &= \varepsilon_{mol}\Phi_N \\
(K_e + V_{e,e} + V_{e,N})\Phi_e &= \varepsilon_e\Phi_e
\end{aligned}
\qquad (1.3)
$$

$V_{eff} = V_{N,N} + \varepsilon_e$ and ε_e being the energy of the electrons. Those are two coupled equations but it is possible to approximate and assume that a new Schrodinger equation has as variables only the position of the Nuclei and no longer the one for the electrons decoupling them.

Finally, by assuming to be in a stable molecule we know that we are in a minimum position of the potential energy therefore:

$$\nabla V = -\frac{\partial V_{eff}}{\partial \mathbf{R}}|_{\mathbf{R}=\mathbf{R}_0} = \mathbf{0} \qquad (1.4)$$
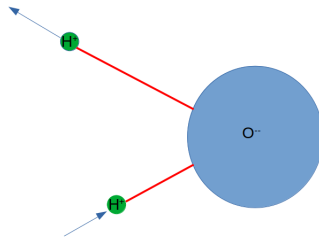
Figure 1.1: Example of a molecular vibration of water

we can use the harmonic oscillator approximation such that:

$$V_{eff} = \frac{1}{2}\frac{\partial^2 V}{\partial R^2}|_{R=R_0}R^2 = \frac{1}{2}kR^2 \tag{1.5}$$

and the problem becomes one of harmonic oscillator. The solution to this problem is known and the energy is

$$\varepsilon_{molecule} = (n + \frac{1}{2})\hbar\omega \tag{1.6}$$

with $n = 0, 1, 2, 3...$ and $\hbar\omega$ the step between each level. The energy level are therefore discrete. We see therefore that the vibration of the nuclei of the molecule gives rise to the different energy levels, and when the molecule is in an exited state it will vibrate similar to a spring. In fig. 1.1 we can see as an example the vibrational mode of water. The discreteness of the energy levels is the basis for Raman scattering and Infrared spectroscopy.

To understand the energy step for every level, one needs to calculate ω from the Schrodinger equation. We will work on well known Raman emitters and we will simply use some Raman spectra that were already published on rruff.info, a repository for Raman spectra.

1.1.2 Elastic Scattering

The main characteristic of Elastic light Scattering is that the wavelength remains unchanged after the event. Two types of scattering are present one is present when the dimension of the scattering center is comparable to the wavelength of light, the second is when the wavelength of light is much larger than the scattering center.

Mie Scattering

The Mie scattering explains the diffusion of a plane wave by a spherical homogeneous particle. Moreover, it can explain the scattering inside biological samples as the dimension of the scattering center can be comparable to the wavelength of light.

Rayleigh Scattering

The Rayleigh scattering is a type of elastic scattering and it is a phenomenon of light propagation in a medium. This effect is present when the wavelength of the

light is much larger than the dimensions of a molecule or particle [41]. The most famous example of this phenomenon is the light propagating in the atmosphere, but it is not prevalent in biological tissues.

A photon will arrive on the molecule and the molecule will act as a dipole. It will excite and re-emit the photon in a random direction giving rise to the scattering effect. This phenomenon is in close correlation to the Raman scattering we will explain later.

1.1.3 Infrared spectroscopy

We have two types of vibrational spectroscopy: Raman and infrared. Infrared is the most consolidated between the two and is also known as absorption spectroscopy. This is because the Vibrational energy gap for vibrational levels of the molecules falls in the infrared range.

In this type of spectroscopy it is used a broad band source in wavelength. An infrared photon will be absorbed by a molecule if the energy gap of the molecule matches the energy of the photon [1]. Once the photons is absorbed the molecule will be in a exited vibrational level. We will measure the absorbance $\mu(\lambda)$ following the Lambert-Beer law

$$I(z, \lambda) = I_0 \exp(-\mu(\lambda)z) \tag{1.7}$$

$$\mu(\lambda) = \frac{\log(\frac{I(z,\lambda)}{I_0})}{z} \tag{1.8}$$

Infrared spectroscopy has some limitations because being in the infrared, some photons will be absorbed too much by common molecules like water and we will lose most information with this process.

1.1.4 Raman scattering

The Raman scattering is a type of inelastic scattering. This effect is present alongside the Rayleigh scattering and the main difference from this is the change in wavelength of the photons. C. V. Raman is the first to document the effect in 1928 [40].

The molecule, when a photon arrives, as in the Rayleigh scattering, will act as a dipole and a virtual level will be exited. The molecules will be de-exited and, differently than Rayleigh, where the initial and final energy of the molecules is the same, the molecule will retain some energy, thus changing the wavelength of the emitted photon. The energy in the molecule will be converted into the vibration of the molecule.

This phenomenon has a very low efficiency of 10^{-6} to 10^{-8}.

As seen in fig. 1.2a for Rayleigh scattering a photon excites a virtual level and then re-emits the same wavelength, in fig 1.2b we have an example of stokes shift where a photon with energy $h\nu$ enters, a virtual level is exited and a photon with energy $h\nu - \Delta$ is re-emitted and finally, in fig. 1.2c we have an example of anti-Stokes scattering where a photon with energy $h\nu$ enters, a virtual level is exited and a photon with energy $h\nu + \Delta$ is re-emitted.

(a) rayleigh scattering.   **(b)** example of stokes shift.   **(c)** example of anti-stokes shift.
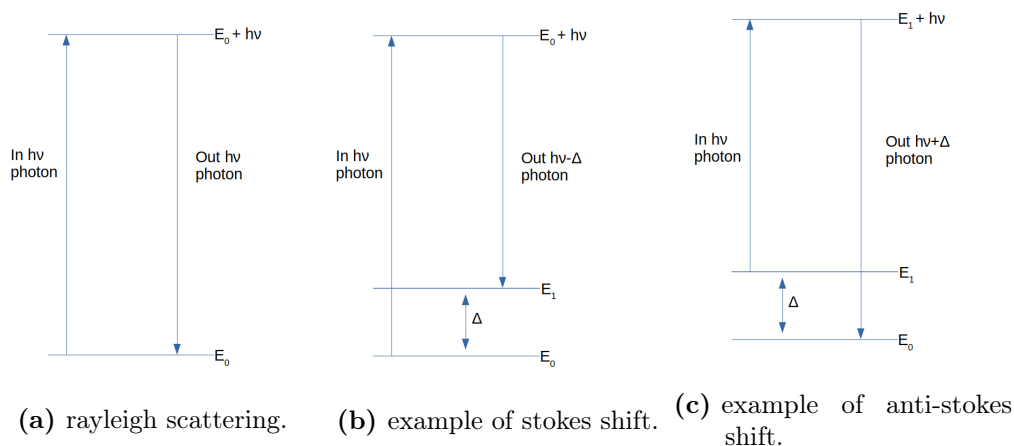
Figure 1.2: Different types of scattering events.

Raman spectroscopy

In Raman spectroscopy, we enter the material with a single wavelength, then the Raman scattering will generate photons at different wavelengths. The wavelength shift is a property of the molecule and by looking at the change in energy of the photons, it is possible to identify a molecule [44].

There are two types of Raman photons:

- If the photon has a higher wavelength it is called a Stokes photon

- if it has lower wavelength is called anti-Stokes

The ratio of Stokes to anti-Stokes photons is given by the population at the excited state of the vibrational level. The population increases with the temperature. Therefore higher temperature means higher prescience of anti-Stokes photons.

At ambient temperature, the presence of those anti-Stokes photons is unlikely therefore, in this work, we will primarily focus our attention on the Stokes photons.

Some useful properties of Raman spectroscopy are:

- the chance to choose the best wavelength where the Raman photons will be less affected by the material absorption(differently from water in IR spectroscopy). Water has a very low absorption in the visible and near-infrared region making it ideal for measurement on biological samples.

- No need to prepare the sample before analyzing it as the light that will be analyzed comes directly from the molecules.

- The Raman emission compared to the time scale of ps is instantaneous

But we have two significant limitations:

- Very low efficiency: at best 1 in every 10^6 photon undergo Raman scattering by a molecule therefore we need to strongly filter the elastic scattered light

- Presence of fluorescence. The lower the wavelength, the higher the amount of fluorescence that will act as noise.

Information from the Raman scattering

The two quantities that will be used to describe the Raman photons will be the wavelength (λ) and wavenumber ($\tilde{\nu}$). The wavelength does not directly give any information on the Raman shift because the shift will be relative to the incidence photons. The wavenumber is the number of repetition of the wave per unit of distance. It linearly represent the energy shift of a molecule as it is defined as $\tilde{\nu} = \frac{1}{\lambda} = \frac{\omega}{2\pi c} = \frac{\varepsilon}{2\hbar\pi c}$.

A Vibrational energy gap will have energy $\varepsilon_R = \hbar\omega_R$, the incoming photon will have frequency $\omega_0 = \frac{2\pi c}{\lambda_0}$ and the final photon will have frequency $\omega_1 = \frac{2\pi c}{\lambda_0} - \frac{\varepsilon_R}{\hbar}$ in wavelength it will be $\lambda_1 = \frac{2\pi c}{\omega_1} = \frac{2\pi c}{\frac{2\pi c}{\lambda_0} - \omega_R}$.

That means that it is difficult to understand the energy distance in the wavelength convention, and for this, the wavenumber convention is introduced.

$$\tilde{\nu} = \frac{\omega}{2\pi c} = \frac{1}{\lambda} = \frac{1}{\lambda_0} - \frac{\omega_R}{2\pi c} \tag{1.9}$$

The wavenumber are usually referred to in cm^{-1}. By knowing the wavenumber shift and looking on a reference table of Raman shift, we can recognize the kind of material being analyzed on a molecular level.

1.2   Diffuse Optics

Diffuse Optics (DO) is the branch of physics that studies the propagation of light through a diffuse medium. In this section, we will present a very short introduction to the diffusive optics field, for additional information, consult [25].

A diffusive media is defined as such if it has much more scattering events as compared to absorption events[25].

Two main parameters are needed to describe the propagation of light in DO:

- the scattering coefficient μ_s

- the absorption coefficient μ_a

From the Lambert-Beer law $l = \frac{1}{\mu_a}$ is the mean free path length for the incident light to be attenuated by a factor e.

Typically $\mu_a \approx 0.1 \ cm^{-1}$ for biological tissues and therefore, we should expect to see through 5-10 cm (biological sample and people would be seen through) of tissue if only the absorption were present. As we said, diffusive media have much more scattering events than absorption events. The presence of scattering is the main reason why most biological samples look opaque. The scattering in biological tissue happens when there is a change in the refractive index n_i and the light changes the direction of propagation. Unlike the Rayleigh scattering, we presented before, which is present when the wavelength is much larger the particle Mie Theory predominately describes the scattering of biological tissues because the wavelength is now comparable to the scattering center.

Mathematical models have been developed to study the propagation of light through diffusive media. The general theoretical explanation of the physics is given

by the Radiative Transfer Equation (RTE). The diffusion approximation should be used when $\mu_s >> \mu_a$, in particular after two assumptions [25]:

- The radiance inside the diffusive media to be isotropic

- The time variation of the flux is slow

from this it is possible to derive the diffuse equation (DE)

$$(\frac{\partial}{v\partial t} + D\nabla^2 - \mu_a)\Phi(\mathbf{r}, t) = q_o(\mathbf{r}, t) \tag{1.10}$$

where:

- $D = \frac{1}{3(\mu_a + \mu'_s)}$

- $v = \frac{c}{n}$ the speed of light in the media

The fundamental quantity to be studied is the fluency rate or fluency Φ $[Wm^{-2}]$ that represents the density of photons passing through a point in any direction of motion

Two different methods exist to study the diffusive properties of materials

- using a continuous wave laser

- pulsed laser, also known as time-resolved

1.2.1 Techniques for DO

After an overview of diffuse optics, we can present the two main techniques for depth probing a material and understanding its diffuse optical properties μ_a and μ_s. From μ_a and μ_s we can image a sample and understand some of its properties.

Continuous wave

A continuous wave source is used to probe inside the material and obtain its optical properties. In this case, the Diffuse optics equation becomes independent of time

$$(D\nabla^2 - \mu_a)\Phi(\mathbf{r}) = q_o(\mathbf{r}) \tag{1.11}$$

The optical characterization of the material can be achieved by changing the injection collector distance or changing the wavelength of the incidence laser (Frequency domain).

It will be possible to have probing capabilities to look into the material by changing the distance of the fiber. As we increase the source collection distance, the scattered photons of the top layers become less important than those that reach the bottom layers making it possible to have depth probing capabilities.

Time Domain

With this approach, we use a pulsed laser source, and the time of arrival of photons will be recorded.

We need to distinguish two types of photons:

- early photons are the first photon to arrive on the detector, the have barely interacted with the material

- late photons are the trailing edge of the photons impulse measured on the detector, they traveled for a long time inside the material

The radiation entering the material due to the scattering is broadened in time. The different photon arrival time is due to the finite speed of light and the travel path took inside the diffusive media [35] That is because some photons will immediately exit the material, but some other photons will travel a longer distance inside the sample and, therefore, exit at a later time, thus broadening the reflected pulse.

In addition to the broadening of the impulse, we will need to consider the absorption of the photons. Using Lambert-Beer law, the attenuation of the photons is $e^{-\mu_a l}$ with l the distance traveled in the object. In time-domain $vt = l$ and $e^{-\mu_a vt}$ therefore the late photons are the ones that will be absorbed.

Using this method, it will be possible to obtain the optical characteristic of the material by looking at the pulse shape. Compared to the continuous wave where it is needed to change the source detection distance with this method, it will be possible to reconstruct such properties by looking at the distribution of the arrival time of the photons [35].

The later photons are the ones that have traveled longer inside the material. Therefore, they are the ones that have the highest probability to have reached the greater depth inside the material [35], but they will also be the ones to have the highest probability for absorption.

As the depth characterization is performed looking at the arrival time, with time-domain it is possible to work at null source collection distance where the photon will travel for the shortest path to reach the depth of the sample.

We will go into more detail in the next section on the setup needed to achieve the time domain and in chapter 2 we will explain better the theory behind the propagation of light into a diffuse material

1.2.2   Time Correlated Single Photon Counting

The main limitation of a time-domain approach was the instrument complexity, such as using Kerr gating or time-gated cameras but the advent of Time-Correlated single-photon counting (TCSPC) simplified the experimental setup required.

In time-resolved approaches, we need to differentiate the arrival time of photons on the order of picoseconds. The detector will only generate a voltage spike at the moment of photons arrival but the issue will be reconstructing the shape of the original signal.

TCSPC [5] is at the basics for the reconstruction of such signal from the detector output voltage change after the detection of a photon.TCSPC traces its origin from

nuclear physics. Such method is used because it allows a high time resolution for the arrival photon on the order of ps.

To use the TCSPC method we need two inputs:

- a signal from the laser, to be used as a reference, refereed as sync

- the signal from the detector

Once the sync has arrived on the TCSPC board, an internal chronometer starts. It waits for the arrival of the electronic signal from the detector. Once the signal from the detector arrives, the chronometer is stopped and in a memory bank on the time gate corresponding to the arrival time, a digital 1 is added, counting how many photons have arrived at each time gate.

This method reconstructs the photon arrival time distribution. After the recording, there is a short dead time for the board when it stores in memory the new photons. If a photon arrives during this dead time, it will not be recorded. For this reason, the system works on the assumption that there are relatively few events on the detector (less than 10^7 cps).

1.3 Diffuse Raman

Diffuse Raman is the field that studies Raman scattering in diffusive materials. This new field has been pioneered by Matousek et al. in 2005 [28].

Conventional Raman techniques easily study the chemical composition on a sample's surface but are limited to the surface. Using Diffusive Raman, it is instead possible to study Raman at depth and therefore understand the chemical composition inside a sample [34].

There are two significant limitations to this field that are in rising order:

- Relatively few photons coming from the depth arrive on the surface of the material and will be collected by the system

- the Raman scattering efficiency is of the order of 10^{-6} to 10^{-8}

Three main methods are available and they can be used in combination.

- Spatially Offset Raman Spectroscopy (SORS) where the probe is moved on the sample.

- Frequency Offset Raman Spectroscopy (FORS) where the probing wavelength is modified

- Time Domain Raman Spectroscopy (TDRS) used a pulsed laser.

TDRS will be the technique used in this thesis.
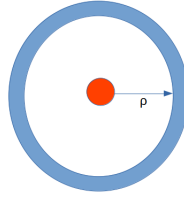
Figure 1.3: Separation of the source collection distance ρ when using a circular illumination for depth probing

1.3.1   SORS

Spatially Offset Raman Spectroscopy (SORS) has been first proposed by Matousek in 2005 [28] and is the most mature of Diffuse Raman techniques. It is already commercially available.

It is a continuous wave technique that uses a spatial offset for the source detection separation for depth probing. As the source detection distance increases, the Raman from the top layer becomes less important and the one from the bottom becomes more prevalent [28]. The spatial separation scheme is shown in fig. 1.3.
 The equipment that is needed to obtain SORS is:

- a continuous wave laser source with a very narrow bandwidth of less than $1cm^{-1}$ and hundreds of milliwatts of power

- a fiber optics cable

- a laser line filter to clean the laser from other unwanted wavelengths

- a probe

- a notch filter or any filter that selects the interested wavelength region and remove the probing wavelength

- a spectrometer that typically uses CCD cameras

Commonly the near-infrared light is used (700nm-1000nm) [30]

Usually for Raman, the source collection distance is null to maximize the light harvested but to achieve the depth probing in SORS is need to add a spatial offset to the point of source collection [29]. For this, multiple methods are possible such as:

- point illumination, point collection

- ring illumination, point collection

- point illumination, ring collection

each one has advantages and disadvantages in Raman collection efficiency, construction and operation of the setup [34] but all achieve the objective of increasing the path of the photon traveled in the sample

A special case of SORS [31] is Transmission spectroscopy Raman where the source and detection are positioned on opposing sides of the detector and the light is forced to pass at depth to reach the second layer

1.3.2 FORS

Frequency Offset Raman Spectroscopy (FORS) is a diffuse Raman technique that exploits the different optical properties (μ_a, μ_s) of the material to achieve the depth profiling first demonstrated in 2017 by Konugolu et al. [42]. It is possible to use this method due to the dependence on wavelength of the scattering and absorption coefficient. As previously explained, only photons that reach the desired depth can be Raman scattered. In this technique, by changing the wavelength the optical properties changes. Therefore the mean photon travel path is changed.

Assuming the absorption and scattering are low at a given wavelength, the photon will penetrate the material and arrive in the bottom layer. If the absorption and scattering are high, the photon will remain in the top layer. Unlike SORS that needed a spatial offset, FORS can work at point source collection equal to zero, thus increasing the spatial resolution. Finally, FORS can be combined with other techniques such as SORS to enhance the depth information using a hybrid SORS-FORS approach.

1.3.3 Time Domain Raman Spectroscopy

Time Domain Raman Spectroscopy (TDRS) technique holds great promise and it is the basis for this thesis. It has been firstly proposed in 2005 by Matousek [27] and later resumed by Konugolu et al. [23] in 2018. This technique was proposed a few months apart from SORS, but before the introduction of TCSPC, this method was limited by a very complex experimental setup [23]. To achieve TDRS, a pulsed laser is needed (at most a few hundreds of ps of FWHM) with a very sharp bandwidth in wavelength, the temporal information, as we previously explained in section 1.2.1 and again will be dealt in chapter 2, holds the depth information. That is due to the delay of the added travel path from one layer to another.

As we said previously, the main limitation of the Continuous wave approach as FORS and SORS is fluorescence. Fluorescence for a Raman measurement is to be considered noise.

In this technique, the Raman measurement has fewer fluorescence problems because Raman is instantaneous and fluorescence has a decay life of the order of ns. That means the signal-to-noise ratio is enhanced.

1.4 Applications

Understanding what is inside an object is useful in many fields. The easiest method to understand the material composition of the inside of an object is to cut it open. This is not an ideal option in several cases, for example with paintings or in clinics.

1.4.1   Non clinical Application

Security

The ability to see inside diffusive objects is useful and could be used in airports, checkpoints, and customs checks or during forensic studies.

Today are employed metal detectors and x-ray scanner yet they cannot differentiate water or other harmless liquids from dangerous acids, drugs or other dangerous fluids [16]. In particular, reference [18] demonstrated its use to detect the presence of concealed ivory.

The ability to see inside a luggage can also determine the presence of explosives without opening the container [24]. In recent decades airports have tried to improve the detection of an improvised explosive device (IED) following counter-terrorism measures.

Food

Seeing inside foodstuff could have interesting finalities such as Qin et al. [38] demonstrated the use of SORS to check the ripening of tomatoes by looking at the lycopene fingerprint. This molecule is generated firstly inside the fruit. Therefore the color is not a completely reliable estimation for the fruit maturation stage.

Other food applications are presented by reference [34]

- nutrient content and origin of potatoes

- concentration of carotene and iodine in fish

- detecting counterfeit products

- presence of additives

Cultural Heritage

When studying history, it is possible that the researcher needs to handle fragile manufacts such as books or amphorae. DIffuse Raman can be used to determine the object's deterioration and the amount of care to be used.

Diffuse Raman can be used to look at paintings and better understand the technique used by the artist or reconstruct a painting hidden composition by a turbid media that the author could have applied during the work, covered in centuries or by graffiti [8].

It has also been demonstrated the measurement of letters covered by a layer of paint [8].

Pharmaceuticals

Analyzing unopened pharmaceutical products can be used to check the quality of the medicine [7].

It is possible to verify the concentration of the active principle and check the quality of the medicine.

The quality control of medicine would require the destruction of some samples and the lack of control for the rest. With diffusive Raman, every sample could be checked.

1.4.2 Clinical Applications

Currently, if it is needed to understand the chemical composition of a patient's tissue, the only option is a biopsy, where a piece of tissue is surgically removed and later analyzed. This is a very reliable method but its main drawback is the invasiveness of the technique.

Another option is the injection of some fluorescence fluid that, upon proper illumination, can be detected. This is less invasive than the biopsy, but the drawbacks are the absence of chemical understanding of the organ and the need to inject some fluorescent fluid requiring a lengthy authorization procedure.

Using a diffusive Raman method by simply shining a laser, it will be possible to probe inside the material with no preparation required to the patient.

Here we will present only a small selection of possible applications that diffuse Raman hopes to contribute significantly.

Diagnosis of bone disease

Raman spectroscopy can differentiate organic components [9], such as collagen, calcite of the bone or phosphate. By analyzing the ratio of the components, it is possible to determine the health of the bone [14] and to diagnose the onset of some bone diseases such as osteoporosis.

The bone is under a layer of a few mm to several cm of skin, lipid and muscle and typical Raman techniques cannot be used on an in vivo subject. Diffuse Raman instead can be applied to obtain the molecular fingerprint at depth.

Diagnosis of breast cancer

Breast cancer is the most diffused cancer in humans. Unfortunately, a significant portion of women is affected by this disease.

The early diagnose of the malignity dramatically lowers the likelihood of death. To diagnose Breast Cancer, mammography is currently commonly used and looks for density changes in the breast that could be linked with malignant lesions [43]. But to obtain it has good sensitivity only for less dense breasts and cannot recognize a malignant tumor to a benign lesion.

For this reason, mammography is used to detect possible malignant tumors and for those reasons, mammography returns a lot of false-positive results.

To confirm the diagnose of breast Cancer, a biopsy is needed.

Breast cancer could instead be identified by looking at the breast lesion and search for calcification.[3] Calcification is present in two types:

- Type I, most commonly associated with benign breast cancer where calcium oxalate is present

- Type II instead is most commonly associated with malignant cancer and hydroxyapatite is present.

It has been demonstrated the use of Diffuse Raman by ref. [45] in a phantom and could solve both of those problems because it will not be limited by the density, since it will depend on the scattering and absorption coefficient of lipid that remains approximately constant between all individuals, and will be able to detect a malignant tumor by looking for the fingerprint for calcification and look for a change in the protein content.

ancer margin

During a cancer removal surgery, a doctor needs to know whether all the tumoral tissue has been removed and limit the extraction of healthy tissue, but differentiating healthy tissue from unhealthy one remains a challenge [21]

Diffuse Raman could be used because it would be able to measure the molecular composition at depth without removing any material and would cover a larger area than a biopsy could allow.

1.5   Overview of the Thesis Work

In Chapter 2, we will present a theoretical model for Raman propagation in a diffusive Media and we highlighted some critical theoretical concepts such as the time broadening inside a fiber. We then estimated the Raman signal collected by a fiber and finally, we presented an approach to find an analytical solution for the Raman signal from a material covered by a diffusive media.

In Chapter 3, an innovative spectrometer that uses wavelength to time mapping (WTT) Raman spectrometer will be presented. It makes use of the different speed of propagation of light inside a fiber. We will first explain its working principle and the setup an then we will present some Raman measurements that were performed with it.

In Chapter 4, we will present a Time-Domain-Diffuse-Raman-Spectrometer that makes use of compressive sensing techniques. This thesis presents some critical improvements of an existing setup to improve its efficiency and resolution and decrease detection noise. We focused our attention on controlling a Digital Micromirror Device (DMD) with the development of a controller program and its synchronization to the TCSPC board. With this spectrometer, we measured the Raman signal coming from some Silicone + Marble phantoms and performed some in-vivo measurements.

Chapter 2

Theory

We need to explain some theoretical concepts of time-domain diffuse Raman before presenting the experimental setup used during the thesis. We will firstly present an alternative approach to the method proposed by Martelli et al. in the article "Time-domain Raman analytical forward solvers" [26] to estimate the Raman fluence. He assumed using Lambert-Beer law, on a first-order approximation that:

$$\Phi_e = \Phi_0 - \Phi_0 exp(-\mu_R vt) \approx \Phi_0 \mu_R vt \tag{2.1}$$

where Φ_e is the Raman fluence and Φ_0 is the probing fluence. This is the heuristic approximation.

We used a different method because we wanted to understand whether the spatial profile was modified or remained unchanged as in the heuristic method. The exact solution had also been presented in reference [2] for the florescence problem in a diffusive media that is equivalent to the Raman propagation.

2.1 Introduction to the Diffuse Raman propagation problem

Starting from the diffuse equation, we want to understand the propagation of the Raman light.

The fluency for the elastically scattered light is described by [25] [26]

$$(\frac{1}{v_0}\frac{\partial}{\partial t} + \mu_{a,0} - D_0\nabla^2)\Phi_0(\mathbf{r}, t) = q_0(\mathbf{r}, t) \tag{2.2}$$

where q_0 is the source light. For the Raman light will be:

$$(\frac{1}{v_e}\frac{\partial}{\partial t} + \mu_{a,e} - D_e\nabla^2)\Phi_e(\mathbf{r}, t) = q_e(\mathbf{r}, t) = \mu_R\Phi_0(\mathbf{r}, t) \tag{2.3}$$

where v_i, $\mu_{a,i}$, D_i are respectively the speed of light, absorption coefficient and scattering coefficient in the media at the specific wavelength, in particular $\mu_{a,0} = \mu_a^0 + \mu_R$ because the inelastic scattering causes the probing light to lose photons.

The source term is proportional to the probing light fluence and so the Raman scattered light is proportional to the probing light intensity, the diffusion operator is linear, so we can compute the flux using the Green function

$$\Phi_e(\mathbf{r}, t) = G_e(\mathbf{r}, t) * q_e = \mu_R G_e(\mathbf{r}, t) * G(\mathbf{r}, t) * q_0 \tag{2.4}$$

The convolution is associative and commutative, so the Green function for Raman is

$$G_R(\mathbf{r}, t) = G_e(\mathbf{r}, t) * G(\mathbf{r}, t) \tag{2.5}$$

APPROXIMATION $n_e = n$ $\mu_a = \mu_a^0 = \mu_{a,e}$ $D = D_e$

This means $G_e = G$ (we will calculate its auto-correlation)

APPROXIMATION we are in an infinite homogeneous medium

$$G(\mathbf{r}, t) = \frac{v}{(4\pi D v t)^{\frac{3}{2}}} exp(-\frac{|\mathbf{r}|^2}{4Dvt} - \mu_a v t) H(t) \tag{2.6}$$

2.2   Derivation

We need to solve the convolution

$$G_R(\mathbf{r}, t) = \int G(\mathbf{R}, \tau) G(\mathbf{r} - \mathbf{R}, t - \tau) d\tau d\mathbf{R} \tag{2.7}$$

$$G_R(\mathbf{r}, t) =$$
$$\int \frac{v}{(4\pi D v \tau)^{\frac{3}{2}}} exp(-\frac{|\mathbf{R}|^2}{4Dv\tau} - (\mu_a + \mu_R)v\tau) H(\tau)$$
$$\frac{v}{(4\pi D v (t - \tau))^{\frac{3}{2}}} exp(-\frac{|\mathbf{r} - \mathbf{R}|^2}{4Dv(t - \tau)} - \mu_a v(t - \tau)) H(t - \tau)$$
$$d\tau d\mathbf{R} \tag{2.8}$$

$$G_R(\mathbf{r}, t) =$$
$$\int \int_0^t \frac{v^2}{(4\pi D v)^3} exp(-\frac{|\mathbf{R}|^2}{4Dv\tau} - (\mu_a + \mu_R) - \frac{|\mathbf{r}\text{-}\mathbf{R}|^2}{4Dv(t - \tau)} - \mu_a v(t - \tau)) \frac{1}{(\tau(t - \tau))^{\frac{3}{2}}}$$
$$d\tau d\mathbf{R} \tag{2.9}$$

We will focus on the exponential:

$$- (\mu_a + \mu_R)v\tau - \mu_a v(t - \tau) = -\mu_a v t - \mu_R v\tau \tag{2.10}$$

NOTE: $\mu_a v t$ is already out of the integral and for ease of writing $\mu_R v\tau$ will be readded at the end

$$-\frac{|\mathbf{R}|^2}{4Dv\tau} - \frac{|\mathbf{r}\text{-}\mathbf{R}|^2}{4Dv(t - \tau)} = -\frac{1}{4Dv}[\frac{|\mathbf{R}|^2}{\tau} + \frac{|\mathbf{r}\text{-}\mathbf{R}|^2}{t - \tau}$$
$$-\frac{1}{4Dv}[\frac{|\mathbf{R}|^2(t - \tau) + \tau|\mathbf{r}\text{-}\mathbf{R}|^2}{\tau(t - \tau)}] = -\frac{1}{4Dv}[\frac{|\mathbf{R}|^2(t - \tau) + \tau|\mathbf{r}|^2 + \tau|\mathbf{R}|^2 - 2\tau\mathbf{r}\mathbf{R}}{\tau(t - \tau)}]$$
$$-\frac{1}{4Dv}[\frac{|\mathbf{R}|^2 t + \tau|\mathbf{r}|^2 - 2\tau\mathbf{r}\mathbf{R}}{\tau(t - \tau)}]$$
$$\tag{2.11}$$

now let's solve for $d\mathbf{R} = dX\,dY\,dZ$

$$\int exp(-\frac{1}{4Dv}[\frac{|\mathbf{R}|^2 t + \tau|\mathbf{r}|^2 - 2\tau\mathbf{r}\mathbf{R}}{\tau(t-\tau)}])d\mathbf{R} =$$
$$= \int exp(-\frac{1}{4Dv}[\frac{|\mathbf{R}|^2 t^2 + \tau t|\mathbf{r}|^2 - 2\tau t\mathbf{r}\mathbf{R}}{t\tau(t-\tau)}])d\mathbf{R} \qquad (2.12)$$

REMEMBER: $\tau t|\mathbf{r}|^2$ can now exit the integral

$$= \int exp(-\frac{1}{4Dv}[\frac{|\mathbf{R}|^2 t^2 + \tau^2|\mathbf{r}|^2 - \tau^2|\mathbf{r}|^2 - 2\tau t\mathbf{r}\mathbf{R}}{t\tau(t-\tau)}])d\mathbf{R} =$$
$$= \int exp(-\frac{1}{4Dv}\frac{|\mathbf{R}t - \mathbf{r}\tau|^2}{t\tau(t-\tau)})d\mathbf{R}\,exp(-\frac{1}{4Dv}\frac{\tau t|\mathbf{r}|^2 - \tau^2|\mathbf{r}|^2}{t\tau(t-\tau)})) \qquad (2.13)$$

we solve the integral in $d\mathbf{R}$ in the Cartesian coordinates X, Y and Z is trivial because it is known that

$$\int_{\infty}^{\infty} exp(-a(x+b)^2)dx = \sqrt{\frac{\pi}{a}} \qquad (2.14)$$

in our case $a = \frac{t}{4Dv\tau(t-\tau)}$ and $\mathbf{b} = \frac{\tau\mathbf{r}}{4Dv\tau(t-\tau)}$ constants with respect to $\mathbf{R}$.
we return to the Green function:

$$G_R = \frac{1}{(4\pi D)^3 vt^{\frac{3}{2}}}exp(-\mu_a vt)\int exp(-\frac{t|\mathbf{r}|^2 - |\mathbf{r}|^2\tau}{4Dvt(t-\tau)})\frac{1}{(\tau(t-\tau))^{\frac{3}{2}}}(4\pi Dv(t-\tau)\tau)^{\frac{3}{2}}$$
$$= \frac{\sqrt{v}}{(4\pi Dt)^{\frac{3}{2}}}exp(-\mu_a vt)\int exp(-\frac{(t-\tau)|\mathbf{r}|^2}{4Dvt(t-\tau)})$$

$$(2.15)$$

readding the exponential $exp(\mu_R v\tau)$

$$G_R(\mathbf{r},t) = \frac{\sqrt{v}}{(4\pi Dt)^{\frac{3}{2}}}exp(-\frac{|\mathbf{r}|^2}{4Dvt})exp(-\mu_a vt)\int_0^t exp(\mu_R v\tau)d\tau \qquad (2.16)$$

focusing on the integral

$$\int_0^t exp(\mu_R v\tau)d\tau = \frac{1}{\mu_R v}(exp(\mu_R vt) - 1) \qquad (2.17)$$

the result is

$$G(\mathbf{r},t) = \frac{v}{(4\pi Dvt)^{\frac{3}{2}}}exp(-\frac{|\mathbf{r}|^2}{4Dvt} - \mu_a vt)(exp(\mu_R vt) - 1)H(t) \qquad (2.18)$$

exactly as the results ref. [26] obtained.
We obtain the same result as the heuristic approximation if we assume $\mu_R vt << 1$ or $\mu_a^0 >> \mu_r$.

$$G_R(\mathbf{r},t) = \mu_R\frac{1}{(4\pi D)^{\frac{3}{2}}}\sqrt{\frac{v}{t}}exp(-\frac{|\mathbf{r}|^2}{4Dvt})exp(-\mu_a vt)H(t) \qquad (2.19)$$
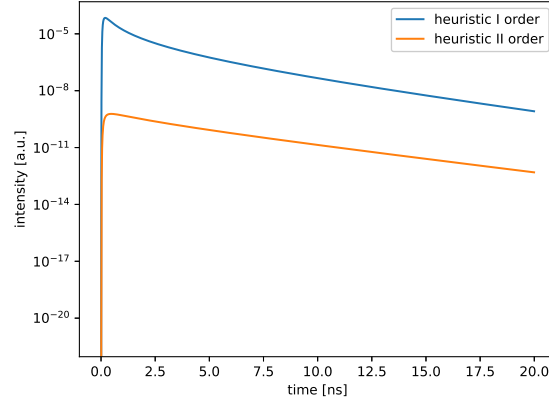
Figure 2.1: Comparison of first and second order heuristic approximation. Assuming $\mu_R = 10^{-6} \ cm^{-1}$, $\mu_a = 10^{-1} \ cm^{-1}$, D = 0.1 cm , comparison between 2.20 and 2.19

2.2.1   The second-order approximation

We can improve the heuristic approximation by including the second-order term such that the refined Green function is $G_R = G_R^I + G_R^{II}$.

The second-order approximation of the heuristic equation shows a reduction in the photon counts of the probing light caused by the removal of the photon by Raman scattering. The second-order term for the Green function is:

$$G_R^{II}(\mathbf{r}, t) = -\mu_R^2 \frac{\sqrt{v^3 t}}{(4\pi D)^{\frac{3}{2}}} exp(-\frac{|\mathbf{r}|^2}{4Dvt})exp(-\mu_a vt)H(t) \qquad (2.20)$$

Even considering a long time and high Raman scattering coefficient, from fig 2.1 we see that the second-order effect is entirely negligible and therefore we should only consider the first term. $\mu_R = 10^{-6} \ cm^{-1}$ is in fact, an extremely high value and by assuming a more reasonable value we would have estimated a lower contribution in the second order.

2.3   Physical meaning

The elastic Green function to the Raman Green function:

$$G_R(\mathbf{r}, t) = \mu_R \frac{1}{(4\pi D)^{\frac{3}{2}}} \sqrt{\frac{v}{t}} exp(-\frac{|\mathbf{r}|^2}{4Dvt})exp(-\mu_a vt)H(t) \qquad (2.21)$$

$$G(\mathbf{r}, t) = \frac{v}{(4\pi Dvt)^{\frac{3}{2}}} exp(-\frac{|\mathbf{r}|^2}{4Dvt} - \mu_a vt)H(t) \qquad (2.22)$$

The ratio $\frac{G_R}{G_0} = \mu_R vt$. The main difference between these two is a factor $\frac{1}{t}$ that causes Raman to be broader in time than the elastic light.
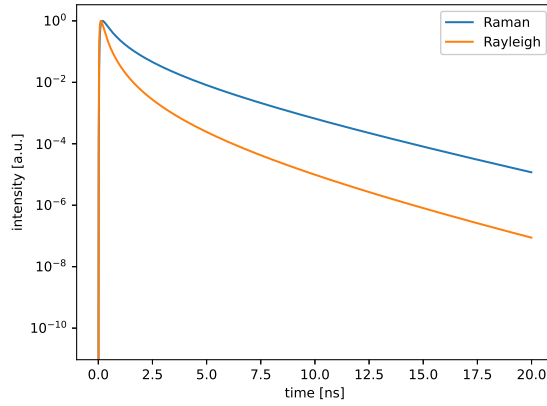
Figure 2.2: Normalized intensity of the reflectivity for the elastic light and Raman

$\rho[cm]$	$FWHM_{elastic}[ps]$	$FWHM_{Raman}[ps]$
0	1.1	1.3
0.5	6	15
1	21	48
2	70	137
4	206	301

Table 2.1: FWHM of the impulse response of the Reflectance as a function of source detection distance

Comparing the two fluences

In particular, the different impulse response functions will cause to broaden the temporal profile of a probing impulse. The final $FWHM$ of the pulse reflected or transmitted will be given approximately by

$$FWHM^2 = FWHM_0^2 + FWHM_{IRF}^2 \qquad (2.23)$$

By calculating the reflectance $R = \frac{\partial \Phi}{\partial z}|_{z=0}$ we can estimate the impulse response of the medium.

From fig. 2.2 we see that the Raman signal has a larger temporal profile than the elastic scattered light. We have estimated assuming typical scattering and absorbtion coefficienct of $\mu_a = 10^{-1}\ cm^{-1}$, D = 0.1 cm. in table 2.1 we present the FWHM estimation from the reflectivity.

The reflected Raman will be distributed on a larger spot relative to the peak intensity because the Raman intensity increases with the travel length and so the likelihood of detecting a Raman photon at a distance increases.

2.4 Estimating the fluence given an illumination source

The fluence is equal to:

$$\Phi_e(\mathbf{r}, t) = q_0(\mathbf{r}, t) * G_e(\mathbf{r}, t) = \int G_e(\mathbf{R}, \tau) q_0(\mathbf{r}\text{-}\mathbf{R}, t - \tau) \tag{2.24}$$

We can only apply $q_0(\mathbf{r}, t)$ on the top surface (z = 0) and we will assume an uniform circular illumination with outer diameter of size d_2 and inner diameter of size d_1 so:

$$q_0(\mathbf{r}, t) = I(x, y, t)\delta(z) = \frac{1}{d_2^2 - d_1^2} A_0 H(\rho - d_1) H(d_2 - \rho) \delta(z) q_0(t) \tag{2.25}$$

where $\rho = \sqrt{x^2 + y^2}$

$$\Phi_e(\rho_0, t) = q_0(\rho, t) * G_e(\rho, z = 0, t) =$$
$$\int \mu_R \frac{1}{(4\pi D)^{\frac{3}{2}}} \sqrt{\frac{v}{\tau}} exp(-\frac{(\rho_0 - \rho)^2}{4Dv(t - \tau)}) exp(-\mu_a v(t - \tau)) H(t - \tau)$$
$$\frac{1}{d_2^2 - d_1^2} A_0 H(\rho - d_1) H(d_2 - \rho) q_0(\tau) \rho d\vartheta d\rho \tag{2.26}$$

NOTE: ρ is the integration variable ρ_0 point in space
we first define the domain of integration:
in τ is from $[-\infty, t]$
for ρ is $\rho - d_1 > 0$ and $d_2 - \rho > 0$
so $[d_1; d_2]$
We first calculate in $d\mathbf{R}$ and then move to $d\tau$

$$\int_{d_1}^{d_2} exp(-\frac{(\rho - \rho_0)^2}{4Dv(t - \tau)}) \rho d\rho d\vartheta \tag{2.27}$$

The solution of the integral (from wolfram Alpha) is:

$$-\sqrt{\pi^3} \rho_0 \sqrt{4Dv}(t - \tau) Err(\frac{\rho_0 - \rho}{\sqrt{4Dv(t - \tau)}}) - exp(\frac{(\rho - \rho_0)^2}{4Dv(t - \tau)}) 2\pi Dvt(t - \tau) \tag{2.28}$$

$$2\pi Dv(t - \tau)(exp(-\frac{(d_1 - \rho_0)^2}{4Dv(t - \tau)}) - exp(-\frac{(d_2 - \rho_0)^2}{4Dv(t - \tau)})) +$$
$$\sqrt{\pi^3 Dv(t - \tau)} \rho_0 (Err(\frac{\rho_0 - d_1}{\sqrt{4Dv(t - \tau)}}) - Err(\frac{\rho_0 - d_2}{\sqrt{4Dv(t - \tau)}})) \tag{2.29}$$

$$\Phi_e = \mu_R \frac{1}{(4\pi D)^{\frac{3}{2}}} \frac{1}{d_2^2 - d_1^2}$$

$$\int_{-\infty}^{\infty} \sqrt{\frac{v}{(t-\tau)}} exp(-\mu_a v(t-\tau))(2\pi Dv(t-\tau)(exp(-\frac{(d_1-\rho_0)^2}{4Dv(t-\tau)}) - exp(-\frac{(d_2-\rho_0)^2}{4Dv(t-\tau)}))+$$

$$\sqrt{\frac{v}{t-\tau}} exp(-\mu_a v(t-\tau))\sqrt{\pi^3 Dv(t-\tau)}\rho_0(Err(\frac{\rho_0-d_1}{\sqrt{4Dv(t-\tau)}}) - Err(\frac{\rho_0-d_2}{\sqrt{4Dv(t-\tau)}}))H((t-\tau))$$

$$q_0(\tau)d\tau$$

$$(2.30)$$

NOTE: For ease of the calculation we will change variable and call $\tau' = (t - \tau)$
$d\tau' = -d\tau$

Looking at the rest:

$$\Phi_e = \mu_R \frac{1}{(4\pi D)^{\frac{3}{2}}} \frac{1}{d_2^2 - d_1^2} \int_0^{\infty} (\sqrt{\frac{v}{\tau}} exp(-\mu_a v\tau)(2\pi Dv\tau$$

$$(exp(-\frac{(d_1-\rho_0)^2}{4Dv\tau}) - exp(-\frac{(d_2-\rho_0)^2}{4Dv\tau}))+$$

$$\sqrt{\frac{v}{\tau}} exp(-\mu_a v\tau)\sqrt{\pi^3 Dv\tau}\rho_0(Err(\frac{\rho_0-d_1}{\sqrt{4Dv\tau}}) - Err(\frac{\rho_0-d_2}{\sqrt{4Dv\tau}}))$$

$$q_0(t-\tau)d\tau$$

$$(2.31)$$

Now we cannot solve this function analytically.

We solve the integral in two parts.

Explaining the exponential term

The spatial distribution we can consider it as a time gate function and similarly to the step function.

$$E(\rho, t) = exp(-\frac{\rho^2}{4Dvt})$$

$$(2.32)$$
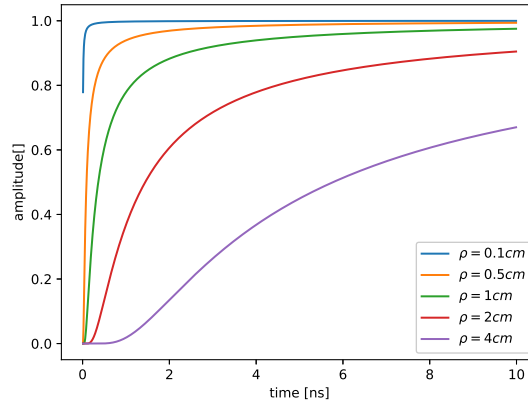
Figure 2.3: Plot of $E(\rho, t)$ assuming $4Dv = 4ns^{-1}$

From fig. 2.3 we see that as we increase the source collection distance the less relevant the early time gates are. This is physically intuitive because there is the time required to propagate the light to the collection point.

Part I

We solve this part:

$$\mu_R \frac{1}{(4\pi D)^{\frac{3}{2}}} \frac{1}{d_2^2 - d_1^2} \int_0^\infty (\sqrt{\frac{v}{\tau}} exp(-\mu_a v\tau)\sqrt{\pi^3 Dv\tau}\rho_0 (Err(\frac{\rho_0 - d_1}{\sqrt{4Dv\tau}}) - Err(\frac{\rho_0 - d_2}{\sqrt{4Dv\tau}}))$$
$$q_0(t - \tau)d\tau$$

$$(2.33)$$

APPROXIMATION

$Err(x) \approx \frac{2}{\sqrt{\pi}}x$ for small x

When $\tau < \frac{(\rho_0 - d_2)^2}{4Dv}$ the function Err to be 1, a constant, otherwise for $\tau > \frac{(\rho_0 - d_2)^2}{4Dv}$
$Err(x) \approx \frac{2}{\sqrt{\pi}}x$

$$\frac{1}{d_2^2 - d_1^2} \int_{\frac{(d_2 - \rho_0)^2}{4Dv}}^\infty \sqrt{\frac{v}{\tau}} exp(-\mu_a v\tau)\sqrt{\pi^3 Dv\tau}\rho_0 \frac{2}{\sqrt{\pi}}(\frac{\rho_0 - d_1}{\sqrt{4Dvt}} - \frac{\rho_0 - d_2}{\sqrt{4Dv\tau}}))q_0(t - \tau)d\tau + A =$$

$$= \frac{1}{d_2^2 - d_1^2} \int_{\frac{(d_2 - \rho_0)^2}{4Dv}}^\infty \sqrt{\frac{v}{\tau}} exp(-\mu_a v\tau)\sqrt{\pi^3 Dv\tau}\rho_0 \frac{2}{\sqrt{\pi}}(\frac{d_2 - d_1}{\sqrt{4Dv\tau}})q_0(t - \tau)d\tau + A =$$

$$= \frac{\pi\sqrt{v}\rho_0}{d_2 + d_1} \int_{\frac{(d_2 - \rho_0)^2}{4Dv}}^\infty \frac{exp(-\mu_a v\tau)}{\sqrt{\tau}}q_0(t - \tau)d\tau + A$$

$$(2.34)$$

We define A as:

$$A = \mu_R \frac{1}{(4\pi D)^{\frac{3}{2}}} \frac{1}{\rho_2^2 - \rho_1^2} \int_{\frac{(d_2-\rho_0)^2}{4Dv}}^{\frac{(d_1-\rho_0)^2}{4Dv}} (\sqrt{\frac{v}{\tau}} exp(-\mu_a v\tau) \sqrt{\pi^3 Dv\tau} \rho_0$$
$$(Err(\frac{\rho_0 - d_1}{\sqrt{4Dv\tau}}) - Err(\frac{\rho_0 - d_2}{\sqrt{4Dv\tau}}))q_0(t-\tau)d\tau$$

(2.35)

Part II

Then solve:

$$\mu_R \frac{1}{(4\pi D)^{\frac{3}{2}}} \frac{1}{\rho_2^2 - \rho_1^2} \int_0^\infty (\sqrt{\frac{v}{\tau}} exp(-\mu_a v\tau)(2\pi Dv\tau(exp(-\frac{(d_1-\rho_0)^2}{4Dv\tau}) - exp(-\frac{(d_2-\rho_0)^2}{4Dv\tau}))$$

(2.36)

APPROXIMATIONS: For the other piece we again assume that the Gaussian is small when the argument is greater than 0
that means for when $\tau > \frac{(d_1-\rho_0)}{4Dv}$

$$\frac{2\pi Dv}{d_2^2 - d_1^2} \int_{\frac{(d_1-\rho_0)^2}{4Dv}}^\infty (\sqrt{\frac{v}{\tau}} exp(-\mu_a v\tau)(\tau(-\frac{(d_1-\rho_0)^2}{4Dv\tau} + \frac{(d_2-\rho_0)^2}{4Dv\tau}))q_0(t-\tau)d\tau + B =$$

$$\frac{2\pi Dv}{(d_2-d_1)(d_2+d_1)} \int_{\frac{(d_1-\rho_0)^2}{4Dv}}^\infty (\sqrt{\frac{v}{\tau}} exp(-\mu_a v\tau)(\tau(\frac{(d_2-d_1)(d_2+d_1-2\rho_0)}{4Dv\tau}))q_0(t-\tau)d\tau + B =$$

$$\frac{\pi\sqrt{v}(d_2+d_1-2\rho_0)}{2(d_2+d_1)} \int_{\frac{(d_1-\rho_0)^2}{4Dv}}^\infty (\frac{exp(-\mu_a v\tau)}{\sqrt{\tau}} q_0(t-\tau)d\tau + B$$

(2.37)

We define B as:

$$B = \mu_R \frac{1}{(4\pi D)^{\frac{3}{2}}} \frac{1}{\rho_2^2 - \rho_1^2} \int \int_{\frac{(d_2-\rho_0)^2}{4Dv}}^{\frac{(d_1-\rho_0)^2}{4Dv}} (\sqrt{\frac{v}{\tau}} exp(-\mu_a v\tau)$$
$$(2\pi Dv\tau(exp(-\frac{(d_1-\rho_0)^2}{4Dv\tau}) - exp(-\frac{(d_2-\rho_0)^2}{4Dv\tau}))))$$

(2.38)

Sum of the two parts

$$\Phi_e(\rho_0, t) = \mu_R \frac{1}{(4\pi D)^{\frac{3}{2}}} (\frac{\pi\sqrt{v}(d_2+d_1-2\rho_0)}{2(d_2+d_1)} \int_{\frac{(d_1-\rho_0)^2}{4Dv}}^\infty (\frac{exp(-\mu_a v\tau)}{\sqrt{\tau}} (q_0(t-\tau)d\tau$$
$$+ \frac{\pi\sqrt{v}\rho_0}{d_2+d_1} \int_{\frac{(d_2-\rho_0)^2}{4Dv}}^\infty \frac{exp(-\mu_a v\tau)}{\sqrt{\tau}} q_0(t-\tau)d\tau)$$

(2.39)

APPROXIMATIONS we assume a ring illumination $d_1 \approx d_2 \approx \rho$
A = B = 0 because the domain of integration is null.

$$\Phi_e(\rho_0, t) = \mu_R \frac{1}{(4\pi D)^{\frac{3}{2}}} \left(\frac{\pi\sqrt{v}(\rho + \rho - 2\rho_0)}{2(\rho + \rho)} \int_{\frac{(\rho-\rho_0)^2}{4Dv}}^{\infty} \frac{exp(-\mu_a v\tau)}{\sqrt{\tau}} (q_0(t-\tau)d\tau \right.$$
$$+ \frac{\pi\sqrt{v}\rho_0}{\rho + \rho} \int_{\frac{(\rho-\rho_0)^2}{4Dv}}^{\infty} \frac{exp(-\mu_a v\tau)}{\sqrt{\tau}} q_0(t-\tau)d\tau) = \tag{2.40}$$

Resulting in:

$$\Phi_e(\rho_0, t) = \mu_R \frac{\pi\sqrt{v}}{(4\pi D)^{\frac{3}{2}}} \int_{\frac{(\rho-\rho_0)^2}{4Dv}}^{\infty} \frac{exp(-\mu_a v\tau)}{\sqrt{\tau}} q_0(t-\tau)d\tau \tag{2.41}$$

This equation shows that if we add a source detection separation, we are not collecting the early photons and will collect only the late photos similarly to a time-gate function.

2.5 Estimating the Reflectance in a semi-infinite media

To obtain a more realistic result we need to consider the semi-infinite geometry. The Green function for the elastic scattered light in the semi-infinite case is:

$$G(\mathbf{r}, t) = \frac{v}{(4\pi Dvt)^{\frac{3}{2}}} exp(-\frac{|\rho|^2}{4Dvt} - \mu_a vt)(exp(-\frac{(z)^2}{4Dvt}) - exp(-\frac{(z + 2z_e)^2}{4Dvt}))H(t) \tag{2.42}$$

where $z_e = AD$ with $A \approx 1$ as seen in ref. [25]

We are interested for now only one calculating $R(\rho, t)$, the reflectivity because the $\Phi_e(z = 0) = 0$ following the boundary condition.

$$R(\rho, t) = D\frac{\partial\Phi}{\partial z}|_{z=0} \tag{2.43}$$

It will be too difficult to obtain the exact solution. For this reason, considering what has been done in section 1 and the heuristic approximation we assume that the Raman Green function is $G_R = G_0\mu_R vt$.

The resulting Green function for reflectance is:

$$R(\rho, t) = \mu_R \frac{2z_e}{(4\pi D)^{\frac{3}{2}} 4v} \sqrt{\frac{v}{t^3}} exp(-\frac{\rho^2 + z_e^2}{4Dvt}) exp(-\mu_a vt)H(t) \tag{2.44}$$

Following the same reasoning made in section 2.4 for the fluency, we get as a result using a ring illumination:

$$R_e(\rho_0, t) = \mu_R \frac{2z_e}{(4\pi D)^{\frac{3}{2}} 4v} \int_{\frac{\rho_0^2 + z_e^2}{4Dv}}^{\infty} \frac{exp(-\mu_a v\tau)}{\sqrt{\tau^3}} q_0(t-\tau)d\tau \tag{2.45}$$

Estimating light collection of a fiber for the Raman scattered light

APPROXIMATION: the excitation time shape (we choose this for the simplicity of integration)

$$q_0(t) = \frac{A_0}{f_w} H(t + \frac{f_w}{2}) H(\frac{f_w}{2} - t) \tag{2.46}$$

APPROXIMATION: assume that $\mu_a v t << 1$

We will get the result avoiding writing the constant $\mu_R \frac{z_e}{3(4\pi D)^{\frac{3}{2}} D v}$

APPROXIMATION: use an analytical time-gate function. $exp(-\frac{a}{t}) \approx H(t - a)$ and by recalling the previous the term $exp(-\frac{\rho^2}{4Dvt})$ previously simplified it is possible to approximate it.

The number of photons collected by a fiber of size d can be estimated by N:

$$N(t) = \int_0^d R(t, \rho) \rho d\rho \tag{2.47}$$

Integrate on ρ to obtain the number of photons per instant.

$$
\begin{aligned}
N &= \int_0^d R\rho d\rho = \int_0^\infty \frac{exp(-\mu_a v \tau)}{\sqrt{\tau^3}} \frac{A_0}{f_w} \\
&H(t - \tau + \frac{f_w}{2}) H(\frac{f_w}{2} - t + \tau) d\tau (-2Dv\tau exp(-\frac{\rho^2}{4Dv\tau}))|_{\frac{z_e^2}{4Dv}}^{\frac{d^2+z_e^2}{4Dv}} = \\
&= \int_0^\infty \frac{2Dv}{\sqrt{\tau}} exp(-\mu_a v \tau) \frac{A_0}{f_w} (exp(-\frac{d^2+z_e^2}{4Dv\tau}) - exp(-\frac{z_e^2}{4Dv\tau})) \\
&H(t - \tau + \frac{f_w}{2}) H(\frac{f_w}{2} - t + \tau) d\tau =
\end{aligned}
\tag{2.48}
$$

By again assuming $exp(-\exp(\frac{z_e^2}{4Dv\tau}))$ to be a time gating function we have for the peak

$$
\begin{aligned}
N_{max} &= \frac{A_0}{f_w} \int_{\frac{z_e^2}{4Dv}}^{\frac{d^2+z_e^2}{4Dv}} \frac{1}{\sqrt{\tau}} \\
&exp(-\mu_a v \tau) H(t - \tau + \frac{f_w}{2}) H(\frac{f_w}{2} - t + \tau) d\tau
\end{aligned}
\tag{2.49}
$$

assume $\frac{d^2}{4Dv} < \frac{f_w}{2}$ and assume $exp(-\mu_a v \tau) \approx 1$

As space we have $exp(-\frac{\rho_0^2+z_e^2}{4Dv\tau})$ and by integrating in ρ we get $4Dv\tau exp(-\frac{2+z_e^2}{4Dv\tau})(-exp(-\frac{d^2}{4Dv\tau}))$

$$N(t) = \int_{\frac{z_e^2}{4Dv}}^{\frac{d^2+z_e^2}{4Dv}} \frac{4Dv}{\sqrt{\tau}} q_0(t - \tau) d\tau \tag{2.50}$$

Assuming $\frac{d^2}{4Dv} < f_w$ the peak number of photons collected is:

$$N_{max} = \mu_R \frac{A_0}{f_w} \frac{z_e \sqrt{v}}{2(4\pi D)^{\frac{3}{2}} v} \frac{\sqrt{d^2 + z_e^2} - z_e}{\sqrt{4Dv}} \tag{2.51}$$

Estimating light collection of a fiber for the elastic scattered light

The number of photons collected by a fiber will be proportional to:

$$N(t) \propto \int_{\frac{z_e^2}{4Dv}}^{\frac{d^2+z_e^2}{4Dv}} \frac{1}{\tau^{\frac{3}{2}}} q(t-\tau)d\tau = \tag{2.52}$$

$$N_{max} \propto \frac{1}{\sqrt{z_e^2}} - \frac{1}{\sqrt{z_e^2+d^2}} \tag{2.53}$$

We can see therefore, from eq. 2.53 and 2.51 that the Raman light is more spatially spread than the elastic light.

2.6 Bilayer

The traction for the bilayer will need to be much approximated due to the complexity of the problem. The main objective of this section will be the understanding of the time dependence for a Raman signal in a bilayer because the time holds the maximum amount of information to solve the problem.

We define L_0 as the diffuse optics operator for material on top and L_1 as the diffuse optics operator for material on the bottom and L_e as the diffuse Raman operator for ease of notation.

- the elastic scattered light propagates through the first media

- the elastic scattered light acts as a source term for the second media

- in the second media the Raman signal is generated

- the Raman signal acts as a source term in the first media

- the Raman signal propagates in the first media

- the Raman signal exits

With no approximation the problem for the bilayer is:

$$\begin{aligned}
L_0\Phi_0 &= q_0, \text{ if } 0 < z < s \\
L_1\Phi_1 &= 0, \text{ if } z > s \\
L_1\Phi_2 &= \mu_R\Phi_1, \text{ if } z > s \\
L_0\Phi_3 &= 0, \text{ if } 0 < z < s
\end{aligned} \tag{2.54}$$

with boundary condition: $\Phi_0(\mathbf{r},0) = 0$ $\Phi_1(\mathbf{r},0) = 0$ $\Phi_2(\mathbf{r},0) = 0$ $\Phi_3(\mathbf{r},0) = 0$ and $\Phi_0(\rho, z = s, t) = \Phi_1(\rho, z = s, t)$ $\Phi_2(\rho, z = s, t) = \Phi_3(\rho, z = s, t)$

But it will be impossible to obtain an analytical solution from this therefore we imagine the process in a bilayer in 3 step:

By calling the reflectance R and Transmittance T

$$R(\rho, t) = \frac{\partial \Phi}{\partial z}\Big|_{z=0} \tag{2.55}$$

$$T(\rho, t) = \frac{\partial \Phi}{\partial z}\big|_{z=s} \tag{2.56}$$

We symplify the problem into:

$$
\begin{aligned}
L_0\Phi_0 &= q_0 + R_1\delta(z - s), \text{ if } 0 < z < s \\
L_1\Phi_1 &= T_0\delta(z - s), \text{ if } z > s \\
L_1\Phi_2 &= \mu_R\Phi_1 + T_3\delta(z - s), \text{ if } z > s \\
L_0\Phi_3 &= R_2\delta(z - s), \text{ if } 0 < z < s
\end{aligned}
\tag{2.57}
$$

We assume that the back-reflection to be a second-order effect we assume it to be negligible.

The bilayer system can be thought as:

$$
\begin{aligned}
L_0\Phi_0 &= q_0, \text{ if } 0 < z < s \\
L_1\Phi_1 &= T_0\delta(z - s), \text{ if } z > s \\
L_1\Phi_2 &= \mu_R\Phi_1, \text{ if } z > s \\
L_0\Phi_3 &= R_2\delta(z - s), \text{ if } 0 < z < s
\end{aligned}
\tag{2.58}
$$

and the final measurement will be performed on $T_3(\rho, t)$
the solution will be, avoiding the constants:

$$T_3(\rho, t) = \frac{1}{t}G_0 * (\frac{1}{t}(G_e * \frac{1}{t}(G_0 * q_0))) \tag{2.59}$$

APPROXMATION: the convolution is not commutative to a function, but we approximate it to be and we will use the reflectance Green function(G_R) and transmittance Green function (G_T)

APPROXIMATION: for the reflection Green function of the Raman we will use the formula calculated using the heuristic approach in section 2.5

$$R(\rho, t) = \mu_R \frac{2z_e}{(4\pi D)^{\frac{3}{2}}4Dv}\sqrt{\frac{v}{t}}exp(-\frac{\rho^2 + z_e^2}{4Dvt})exp(-\mu_a vt)H(t) \tag{2.60}$$

APPROXIMATION: We will use the semi-infinite media approximation(m = 0)

$$G_T = \frac{exp(-\frac{\rho^2}{4Dvt} - \mu_a vt)}{2(4\pi Dv)^{\frac{3}{2}}t^{\frac{5}{2}}}(sexp(-\frac{s^2}{4Dvt}) - (s + z_e)exp(-\frac{(s + z_e)^2}{4Dvt}))H(t) \tag{2.61}$$

DEFINITION: We will call $\frac{s^2}{4Dv} = t_0$ and $\frac{z_e^2}{4Dv} = t_1$
APPROXIMATION: $s >> z_e$

$$G_T = \frac{exp(-\frac{\rho^2}{4Dvt} - \mu_a vt)}{2(4\pi Dv)^{\frac{3}{2}}t^{\frac{5}{2}}}sexp(-\frac{s^2}{4Dvt})H(t) \tag{2.62}$$

We will perform the calculation in two steps:

- Part I $T * R$

- Part II $(T * R) * T$

Part I

$$T * R = \int T(t - \tau) R(\tau) d\tau =$$

$$\int \frac{exp(-\frac{(r-R)^2}{4Dv(t-\tau)} - \mu_a v(t-\tau))}{2(4\pi Dv)^{\frac{3}{2}}(t-\tau)^{\frac{5}{2}}} s exp(-\frac{s^2}{4Dv(t-\tau)})H(t-\tau) \qquad (2.63)$$

$$\mu_R \frac{2z_e}{(4\pi D)^{\frac{3}{2}}4Dv} \sqrt{\frac{v}{\tau}} exp(-\frac{R^2 + z_e^2}{4Dv\tau}) exp(-\mu_a v \tau) H(\tau) d\tau dR$$

from the integral can already exit $\frac{1}{2(4\pi Dv)^{\frac{3}{2}}} s \mu_R \frac{2z_e}{(4\pi D)^{\frac{3}{2}}4Dv} \sqrt{v} exp(-\mu_a v t)$
assuming $exp(-\frac{s^2}{4Dvt} \approx H(t - \frac{s^2}{4Dv})$

$$\int \frac{1}{(t-\tau)^{\frac{5}{2}}} exp(-\frac{(r-R)^2}{4Dv(t-\tau)})H(t-\tau-\frac{s^2}{4Dv})\frac{1}{\tau^{\frac{3}{2}}} exp(-\frac{R^2}{4Dv\tau})H(\tau-\frac{z_e^2}{4Dv}) \quad (2.64)$$

as done previously the integral in $dR = dXdY$ is trivial and is equal to

$$\frac{4\pi Dv(t-\tau)\tau}{t} exp(-\frac{r^2}{4Dvt}) \qquad (2.65)$$

the part outside the integral becomes
$exp(-\mu_a vt) exp(-\frac{r^2}{4Dvt}) \frac{\mu_R z_e vs}{(4\pi Dv)^2 4}$
continuing the integration in $d\tau$

$$\int_{\frac{z_e^2}{4Dv}}^{t-\frac{s^2}{4Dv}} \frac{1}{(t-\tau)^{\frac{5}{2}}} \frac{(t-\tau)\tau}{\tau^{\frac{3}{2}}t} = \int \frac{1}{t(t-\tau)^{\frac{3}{2}}\tau^{\frac{1}{2}}}$$

$$= \frac{\sqrt{\tau}}{t^2\sqrt{t-\tau}}\Big|_{\frac{z_e^2}{4Dv}=t_1}^{t-\frac{s^2}{4Dv}=t-t_0} = \frac{2\sqrt{t-t_0}}{t^2\sqrt{t_0}} - \frac{2\sqrt{t_1}}{t^2\sqrt{t-t_1}}H(t-t_0-t_1) \qquad (2.66)$$

Part II

We need to convolute a second time for the Green function of the transmittance

$$(R * T) * T = \int (R * T)(\tau, R) T(t-\tau, r-R) dR d\tau =$$

$$\int (\frac{2\sqrt{t-t_0}}{\tau^2\sqrt{t_0}} - \frac{2\sqrt{t_1}}{\tau^2\sqrt{\tau-t_1}}) exp(-\frac{R^2}{4Dv\tau})H(\tau-t_0-t_1) \qquad (2.67)$$

$$\frac{1}{(t-\tau)^{\frac{5}{2}}} exp(-\frac{(r-R)^2}{4Dv(t-\tau)})H(t-\tau-t_0) dR d\tau$$

again the solution to dR is $\frac{4\pi Dv(t-\tau)\tau}{t} exp(-\frac{r^2}{4Dvt})$

and the integral will be

$$\int_{t_0+t_1}^{t-t_0} \frac{2\sqrt{\tau-t_0}}{\sqrt{t_0}\tau(t-\tau)^{\frac{3}{2}}} - \frac{2\sqrt{t_1}}{\tau\sqrt{\tau-t_1}(t-\tau)^{\frac{3}{2}}} \tag{2.68}$$

$$\int \frac{\sqrt{\tau-t_0}}{\tau(t-\tau)^{\frac{3}{2}}} = 2\left(\frac{\sqrt{t_0}tan^{-1}\left(\sqrt{\frac{t_0(t-\tau)}{t(\tau-t_0)}}\right)}{t^{\frac{3}{2}}} + \frac{\sqrt{\tau-t_0}}{t\sqrt{t-\tau}}\right) \tag{2.69}$$

$$\int \frac{2\sqrt{t_1}}{\tau\sqrt{\tau-t_1}(t-\tau)^{\frac{3}{2}}} = 2\sqrt{t_1}\left(\frac{\sqrt{\tau-t_1}}{t(t-t_1)\sqrt{t-\tau}} - \frac{tan^{-1}\left(\sqrt{\frac{t_1(t-\tau)}{t(\tau-t_1)}}\right)}{\sqrt{t_1}t^{\frac{3}{2}}}\right) \tag{2.70}$$

the solution is

$$
\begin{aligned}
2\Bigg(&\frac{tan^{-1}\left(\sqrt{\frac{t_0^2}{t(t-2t_0)}}\right)}{t^{\frac{3}{2}}} + \frac{1}{t\sqrt{t_0}}\sqrt{\frac{t-2t_0}{t_0}} - \\
&\frac{tan^{-1}\left(\frac{t_0(t-t_0-t_1)}{tt_1}\right)}{t^{\frac{3}{2}}} - \frac{1}{t\sqrt{t_0}}\sqrt{\frac{t_1}{t-t_0-t_1}}\Bigg) \\
&- 2\sqrt{t_1}\Bigg(2\frac{\sqrt{t-t_0-t_1}}{t(t-t_1)\sqrt{t_0}} - \frac{2tan^{-1}}{\sqrt{t_1}t^{\frac{3}{2}}}\left(\sqrt{\left(\frac{t_1t_0}{t(t-t_0-t_1)}\right)}\right)\Bigg) - \\
&- 2\frac{\sqrt{t_0}}{t(t-t_1)\sqrt{t-t_0-t_1}} + \frac{2}{\sqrt{t_1}t^{\frac{3}{2}}}tan^{-1}\left(\sqrt{\frac{t_1(t-t_0-t_1)}{tt_0}}\right)\Bigg)
\end{aligned}
\tag{2.71}
$$

we need to approximate this:

firstly assume that $s >> z_e$ and therefore $t_0 >> t_1$ knowing that it is possible to say that the term $\frac{1}{t\sqrt{t_0}}\sqrt{\frac{t-2t_0}{t_0}}$ dominates when $t \to \infty$ but at $t = t_{initial}$ we have to be careful

We know that the most relevant in this time region is $\frac{tan^{-1}\left(\sqrt{\frac{t_0^2}{t(t-2t_0)}}\right)}{t^{\frac{3}{2}}} - \frac{tan^{-1}\left(\frac{t_0(t-t_0-t_1)}{tt_1}\right)}{t^{\frac{3}{2}}}$

$\frac{\pi}{4} < \frac{tan^{-1}\left(\sqrt{\frac{t_0^2}{t(t-2t_0)}}\right)}{<} \frac{\pi}{2}$
and
$tan^{-1}\left(\frac{t_0(t-t_0-t_1)}{tt_1}\right) \approx tan^{-1}\left(\sqrt{\frac{t_0}{t_1}}\right) \approx \frac{\pi}{2}$

APPROXIMATION: we assume this region to be equal to $\frac{tan^{-1}\left(\sqrt{\frac{t_0^2}{t(t-2t_0)}}\right)}{t^{\frac{3}{2}}} -$
$\frac{tan^{-1}\left(\frac{t_0(t-t_0-t_1)}{tt_1}\right)}{t^{\frac{3}{2}}} \approx -\frac{\pi}{4t^{\frac{3}{2}}}$
and in total it will be:

$$\frac{1}{t\sqrt{t_0}}\sqrt{\frac{t-2t_0}{t_0}} - \frac{\pi}{4t^{\frac{3}{2}}} \text{ with } t > 2t_0 + t_1 \tag{2.72}$$

putting all the constants
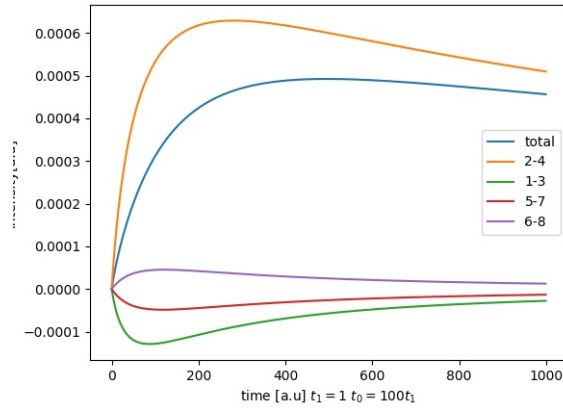
Figure 2.4: Comparing the transmittance with all terms with the various terms, the number is in the order of appearance and assuming $t_0 = 100t_1$
assuming $z_e = D = 0.1cm$ and $s = 1cm$
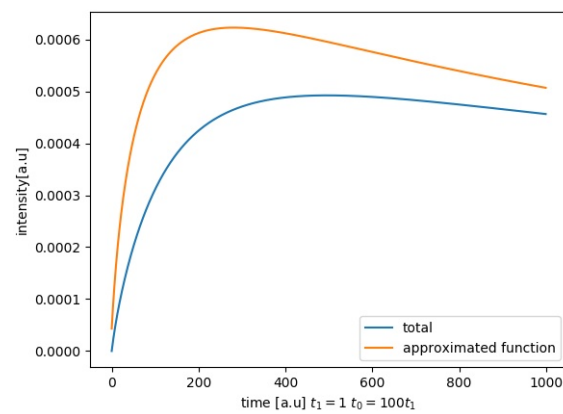
Figure 2.5: Comparing the total transmittance with the approximation

$$T(\rho, t) =$$

$$\frac{s^2 \mu_R z_e \upsilon}{8(4\pi)^{\frac{7}{2}}(D\upsilon)^{\frac{5}{2}}}(\frac{1}{t^2\sqrt{t_0}}\sqrt{\frac{t - 2t_0}{t_0}} - \frac{\pi}{4t^{\frac{5}{2}}}) \tag{2.73}$$

$$exp(-\mu_a \upsilon t)exp(-\frac{\rho^2}{4D\upsilon t})H(t - 2\frac{s^s + z_e^2}{4D\upsilon})$$

At infinity, it behaves as in the reflectance case (but due to absorption, we will not reach this region)

The rising edge is slower than Raman in reflectance, and we see that there is a delay of $\frac{s^s + z_e^2}{2D\upsilon}$ from the arrival of the probing pulse to on the top layer to the emission of the Raman signal of the bottom layer from the top layer and a time $t*$ from the start of the emission to the maximum position ot the curve.

Using this equation, it will be possible to estimate the time curve of the Raman signal from a material covered by a diffusive layer. Using the time profile, it will be possible to estimate the origin depth of a Raman signal.

In particular two methods are possible to estimate the time-delay.

- using a reference Raman signal, and the time delay would be estimated using $\Delta t = t_{max,Bi} - t_{max,Raman,Ref}$, where t_{max} is the peak position.

- measure a reference elastic scattered pulse $\Delta t = t_{max,Bi} - t_{max,El,Ref}$.

2.6.1 Estimating the photons collected by a fiber

APPROXIMATION We will use the same method and approximation as the one presented in 2.5

- $exp(-\mu_a \upsilon t) \approx exp(-\mu_a \upsilon t_I) \approx exp(-2\mu_a \upsilon t_0) = exp(-\mu_a \frac{s^2}{2D})$

$$N(t) = \int T * q(t)\rho d\rho = \int (1 - exp(-\frac{d^2}{4D\upsilon\tau}))\frac{4D\upsilon\tau z_e^2 \mu_R}{\upsilon(4\pi D)^{\frac{3}{2}}}$$

$$(\frac{1}{\tau^2\sqrt{t_0}}\sqrt{\frac{\tau - 2t_0}{t_0}} - \frac{\pi}{4\tau^{\frac{5}{2}}})H(\tau - 2\frac{s^s + z_e^2 + sz_e}{4D\upsilon}) * q(t - \tau) \tag{2.74}$$

$$\int \frac{\sqrt{t - 2t_0}}{tt_0} - \frac{\pi}{4t^{\frac{3}{2}}}dt =$$

$$\frac{2\sqrt{t - 2t_0}}{t_0} - \frac{2\sqrt{2t_0}}{t_0}tan^{-1}(\sqrt{\frac{t - 2t_0}{2t_0}}) + \frac{\pi}{2\sqrt{t}} \tag{2.75}$$

now the domain of integration will at the t_{max} will be $[t_i, \frac{d^2}{4D\upsilon} + t_i]$ with $t_i = 2\frac{s^s + z_e^2 + sz_e}{4D\upsilon} = 2t_0 + 2t_1 + 2\sqrt{t_1 t_0} = 2t_0 + 2t_\varepsilon$

$$N_{max} = \frac{2}{t_0}(\sqrt{\frac{d^2}{4D\upsilon} + t_\varepsilon} - \sqrt{t_\varepsilon}) - \frac{2\sqrt{2}}{\sqrt{t_0}}(tan^{-1}(\sqrt{\frac{\frac{d^2}{4D\upsilon} + t_\varepsilon}{2t_0}}) -$$

$$- tan^{-1}(\sqrt{\frac{t_\varepsilon}{2t_0}})) - \frac{\pi}{2}(\frac{1}{\sqrt{t_i}} - \frac{1}{\sqrt{t_i + \frac{d^2}{4D\upsilon}}}) \tag{2.76}$$

and by assuming $\frac{d^2}{4Dv} >> t_\varepsilon$

$$N_{max} = \frac{A_0}{f_w}\frac{s^2\mu_R z_e v}{8(4\pi)^{\frac{7}{2}}(Dv)^{\frac{5}{2}}}\left(\frac{d}{t_0\sqrt{Dv}} - \frac{\sqrt{2\pi}}{\sqrt{t_0}2} - \frac{\pi}{2}\frac{1}{\sqrt{t_i}}\right)exp\left(-\mu_a\frac{s^2}{2D}\right) \qquad (2.77)$$

2.7 Conclusion

We firstly calculated using a different method than the one presented in [26] the Raman light Green function. We found that the two methods find the same result.

We then tried to estimate the fluency given an illumination area and estimated the photon collected by a fiber. We found that the Raman is distributed on a larger area than the elastic scattered light.

We finally tried to estimate the Green function for a Raman signal coming from a material covered by a diffusive layer.

Chapter 3

Wavelength Through Time Spectrometer

The first part of the thesis had been dedicated to the development of a Raman Spectrometer that takes advantage of the different speeds of propagation inside a fiber for different wavelengths. This spectrometer makes use of temporal separation instead of spatial separation.

A pulsed laser is sent into the sample. The reflected light is collected by a probe and sent via a long fiber to a single-pixel detector. Inside the fiber, the Raman wavelength will travel at a different speed than the probing wavelength separating the two. We will record the difference in arrival time of the photons thus, reconstructing the spectrum [12].

The thesis will present the proof of concept of this method but has four possible applications if further developed:

- Raman spectrometer for probing a small region of space.

- Raman spectrometer comparable with a CCD spectrometer with much lower complexity.

- a cheap and lightweight Raman spectrometer with low energy consumption[32]

- Raman camera [12]

In this chapter we will present this new type of spectrometer for Raman.

- Physical basis on the operation of the spectrometer

- present and characterize the illumination source (the laser and injection path)

- probing optical system

- the spectrometer setup

- characterization of the spectrometer

- Measurements taken with this new instrument

The setup used is schematically shown in figure 3.1.
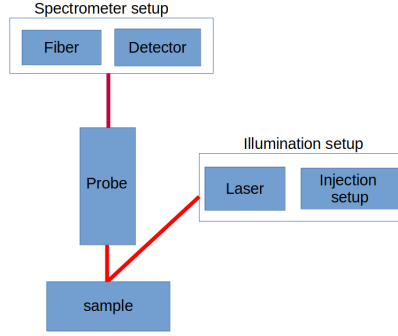
Figure 3.1: General scheme of the setup.

3.1 Physics

Light is an electromagnetic radiation that interacts with matter. After it interacts a new electric field will be produced. The sum of the original electric field and the new perturbation field will generate a final field with a lower speed of propagation than light. The reduction of speed in the material is given by n, the refractive index. The new speed of light will depend on the wavelength of the photons, causing a dispersion effect. The wavelength dispersion coefficient (D) will express the delay per wavelength per unit of space. Therefore, if two pulses with different wavelengths start simultaneously, they will arrive at different times [12]. The difference in the time of arrival will be Δt:

$$\Delta t = \int_{\lambda_0}^{\lambda_1} LD(\lambda)d\lambda \qquad (3.1)$$

Where L is the length of the fiber and λ_0, λ_1 are the two wavelengths that we are separating.

If we know:

- the dispersion coefficient $D(\lambda)$, and $D(\lambda)$ is monotone

- the length of the material

- a reference wavelength arrival time

We can reconstruct the wavelength of a pulse by looking at the time position of a photon, making use of temporal separation instead of spatial separation as in a CCD spectrometer. Therefore this phenomenon can be used as a spectrometer for pulsed light. Moreover we can use a single- pixel detector instead of a camera to measure the spectra using this phenomenon.

In our case, we will have a pulsed laser light interacting with a material, and we will observe two main types of scattering:

- elastic scattering, where the wavelength remains unchanged

- Raman scattering where there is a change in the wavelength
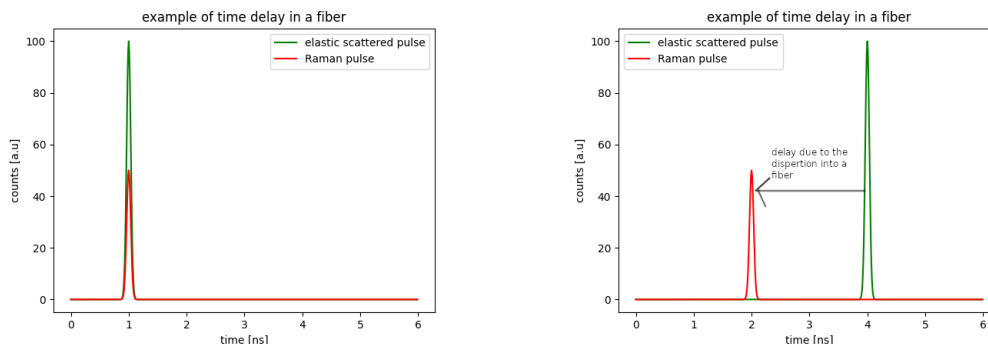
Figure 3.2: Example of temporal Delay

Both types of scattering are instantaneous and will retain a pulse shape, as seen in chapter 2. The sample will reflect the two scattered pulses at the same time. However, they will have different wavelengths, as we explained above and shown in fig 3.2 we will observe a separation of the wavelength that we will be able to study with the spectrometer we built.

The spectrometer

Two, or more pulses, will enter the fiber, be separated and then recorded by the detector. The resolution of the spectrometer is given by the temporal resolution of the system. The quantities that will affect the temporal resolution are

- bandwidth of the laser

- FWHM of the pulse

- collection illumination distance. Therefore the FWHM of the Green function.

- Modes of the fiber

- length of the fiber

- number of channels of the TCSPC board

3.2   The Illumination setup

The illumination setup is represented in fig. 3.3. To probe into the sample for Raman spectroscopy, three characteristics for the light are needed:

- High Power. The Raman scattering is a very low-efficiency process and therefore, we need a very high number of scattering events to occur. Therefore, increasing the number of photons interacting with the material will increase Raman photons linearly.

- Good spectral resolution is required to achieve Raman to distinguish two peaks. It is achieved by having a laser with a very small bandwidth. The
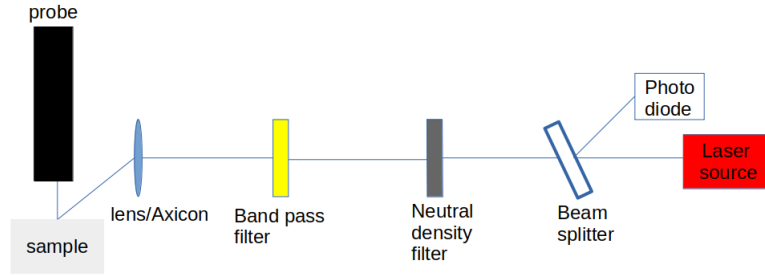
Figure 3.3: Scheme of the illumination setup

bandwidth is linked with the resolution because the Raman will shift all the photons by a constant amount. The spectral bandwidth of the laser is the minimum resolution achievable by the spectrometer.

- Good temporal resolution, full width at half maximum (FWHM), such that the Raman peak will be well resolved in time.

For those reasons, the laser chosen in this work is a Titanium-Sapphire laser in active mode-locking.

As we will later show, this laser has all those characteristics with the addition of the tunability of the wavelength that will let us explore Raman with different probing wavelengths. The following injection setup will be used to clean the laser light of eventual unwanted wavelengths, direct the light on the sample with the desired shape.

3.2.1   Titanium Sapphire Laser

The laser is a solid-state laser with optical pumping. The active material is a Titanium Sapphire crystal, made of TiO_2, and was built in-house.

As the optical pump, we use a Nd:Yg at 532 nm in continuous wave, Millenia V from Spectra-physics, with a minimum output power of 0.2W and a maximum of 5W. This laser uses a second harmonic generation to obtain the 532 nm wavelength and will require a chiller to cool the second harmonic crystal.

The pump laser will enter a cavity where it will interact with the crystal and obtain the laser action via the stimulated emission process. The light is confined in a cavity by mirrors with high reflectivity in the desired wavelength range. The wavelength of operation is selected by a Lyot filter that is placed inside the cavity. The filter blocks the laser action, other than the selected wavelength of operation where the losses can be lower than the threshold power of the laser, thus allowing the laser action.

The laser can work in both continuous-wave regime and pulsed regime.

The pulse regime is achieved with active mode-locking using acoustic optical modulation. Inside the cavity, we have a crystal with high-frequency acoustic modulation. An acoustic wave that travels through a material changes the pressure and the density at each point of the material. The change in density causes a change in the refractive index of the material. The crystal will act as a grating dispersing the photons in space and therefore adding losses.

At one small instant in time, the modulator allows the light without any loss, therefore, allowing the laser action.

characterization of the laser

Before using the laser, we need to understand its properties and any problem of the laser should be considered during the measurement phase

Basic quantities

The characterization of the laser measurement was taken in Impulse Response Function mode (IRF), where the light from the laser was connected directly to the detector before encountering any samples.

- The barycenter gives the position of the pulse. It is defined as

$$b = \frac{\int c(t)t dt}{\int c(t) dt} \tag{3.2}$$

  where c is the counts per unit of time.

- The full width at half maximum that will be referred to as FWHM is a quantity that express the time duration of the pulse. It is defined as the distance in time of the two points where the distribution has the value of half of the maximum of the function.

- The total photon counts is the sum of all the photons recorded on the curve.

- The background is the photon counts before the arrival of the pulse, where the number of photons is not influenced by the pulse

.

Spectral Band

A highly significant characteristic of a laser for Raman is its spectral bandwidth because it will give the minimum possible resolution of the pulse. We have not directly measured the spectral band of the laser pulse of the Titanium Sapphire laser but a measurement was taken previously the beginning of this thesis measured the bandwidth of the laser at 764 nm at 0.09 nm as seen from fig. 3.4

Stability

A stable laser is important because the variation in the total count, FWHM or barycenter will be an additional source of noise if a long measurement is performed and during the data analysis, the instability will be needed to be taken into account.
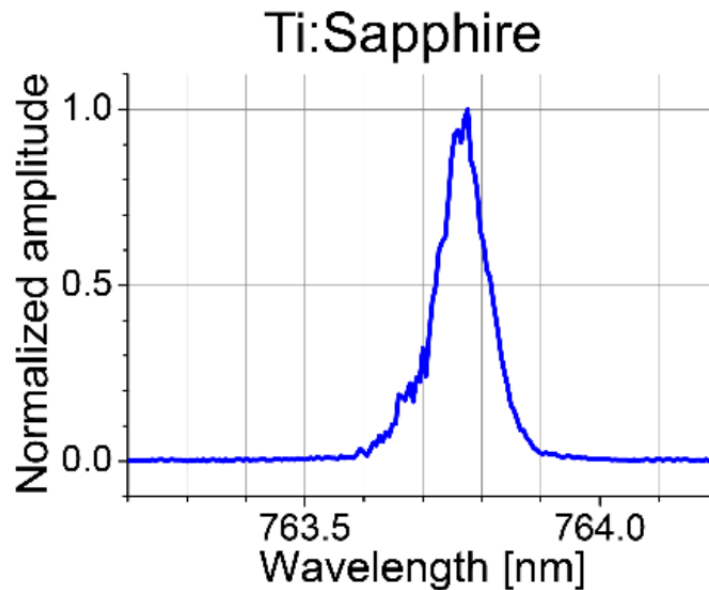
Figure 3.4: Laser spectra

For one hour, a measurement has been taken. The measurement has been taken in IRF, impulse response function. This mode consists in connecting the laser output directly to the detector. The IRF has been taken with a 1 Hz frequency. This has been done to measure the stability of the laser.

From fig. 3.5 we have the stability measurements. Especially the FWHM and the total photon counts are important as a shift during measurement and if a long measurement is performed, it has to be averaged out to avoid artifacts.

Spectral power

The Titanium-Sapphire laser is a tunable laser where we can change the output laser wavelength. We have changed the position of the Lyot filter, thus changing the wavelength, we have measured the power. The power is not constant due to the varying efficiency of the optical components at each wavelength. The measures in fig. 3.6 were taken with a set of mirrors optimized in the region 700-860 nm.

Criticalities of the Titanium Sapphire laser

One main limitation of the laser is its low stability., The laser, during its operation disalign and the output power and FWHM of the laser changes in time. This issue could be critical and has to be considered during the measurements and data analysis.

A second limitation was the pump laser. To increase the output power and optimize the FWHM of the Ti-Sa laser, we would need to increase the power of the optical pump. The critical component during the thesis was the Millenia pump laser, which presented significant problems due to its long operational life. By the end of the thesis, the laser was not able to function at more than 3W and frequently shut off.

(a) Background stability.

(b) Barycenter stability

(c) FWHM stability

(d) Stability of the total photon counts
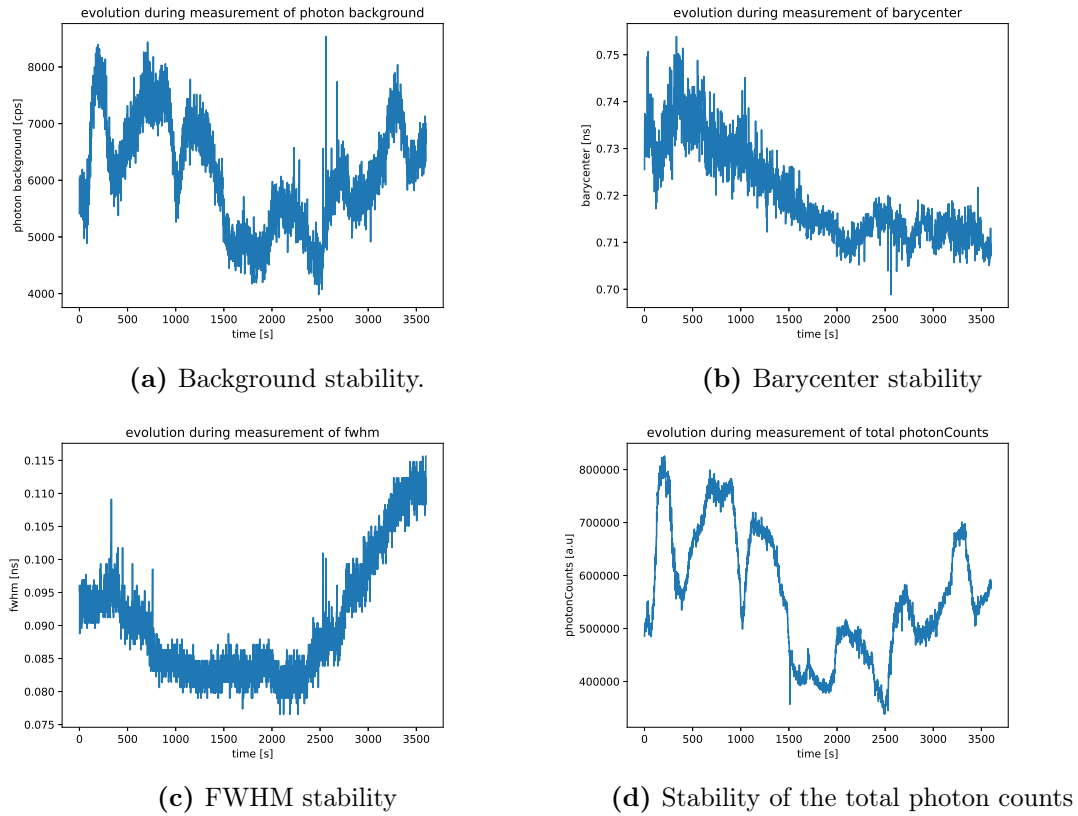
Figure 3.5: Measurements on the stability of the laser
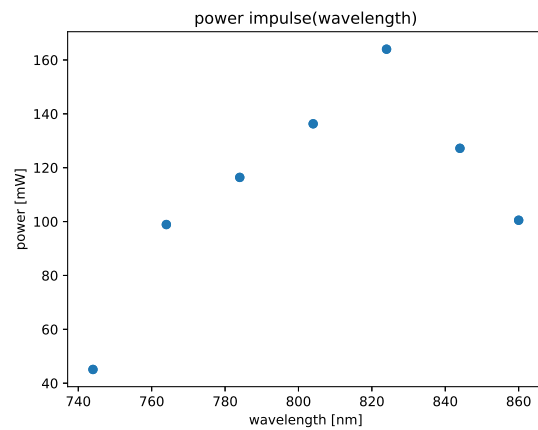
Figure 3.6: Power in pulsed regime as a function of wavelength

Other lasers

Two other lasers have been used during this thesis:

- Supercontinuum laser from NKT photonics. It produces white light and we use a motorized grating to separate the various wavelength components and couple the selected wavelength into a fiber for the measurements. Due to the ease of changing the wavelength, it has been used during the calibration processes.

- Pulse Diode Laser(PDL) is a low-power laser at 670 nm or 820 nm depending on the diode used. The operational power of the laser is 1mW and visible. The laser has been used during the alignment phases.

Both lasers will not be used during the Raman measurement, but they have been used during the alignment procedure or calibration. They are all pulsed lasers, but they had a large spectral band close to 10 nm and very low power of around or less than 1 mW

3.2.2   The injection

The injection system is the path the light takes after exiting the laser to reach the sample. In this path, we will optimize the laser source to have the output laser required on the sample.

After the light exits the cavity of the Ti-Sa laser, it encounters a beamsplitter that is needed to direct a small fraction of light on a detector (A photodiode or a SIPM) that will record the arrival of the pulse into an electronic signal. The TCSPC board will use this electronic signal as a sync signal that will be taken as a reference to produce the photon arrival time distribution.

Then a neutral density filter will be used to reduce the power of the light. If we have a high number of photons, it is needed as they would saturate the detectors or the electronic board. The saturation of the detectors can happen due to the dead time of the active area. The saturation of the electronic board can happen if two or more photons arrive during a single repetition, making it impossible for the TCSPC board to reconstruct the pulse shape. Using a neutral density filter, we can reduce the power as much as needed. It is mainly needed during the alignment process. The attenuator will be completely open when the Raman measurement runs because there is no risk of saturation with the Raman signal.

Then we reach a laser cleaning filter that removes any unwanted spectral components. The filter is mounted at an angle to the optical path to reflect away the removed component from the measurement location into a beam dump.

Then a lens can be present that will focus, de-focus, or make a ring illumination.

Finally, we have a mirror that will be used to direct the light on the sample. The light travels on a plane parallel to the optical table. To reach the sample, we need to add an angle to the beam. Such mirror will be used to make coarse and fine adjustments on the positioning of the laser spot on the sample.

(a) Focused light on the collection point

(b) Collimated or unfocused light

(c) Ring illumination around the collection point
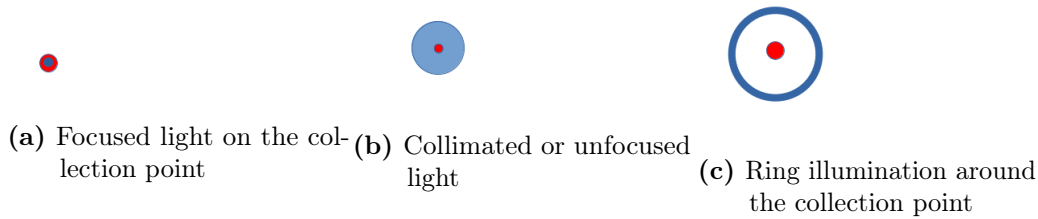
Figure 3.7: Different types of illumination on a sample

Laser cleaning filters

A laser cleaning filter is needed to remove any unwanted photons that the Ti-Sa laser produced. The reason for the unwanted photons are the fluorescence of the crystal and the light coming from the pump laser.

Such photons will be in a sufficiently high number to bury the Raman photons generated by the probing wavelength. They will act as a noise background, as they will not have a pulsed shape, but they are a continuous wave background.

Image on the sample

There are three main options for illumination on a sample that change the source detection (SD) distance here we will also refer to it as ρ.

- focused in fig. 3.7a

- collimated in fig. 3.7b

- ring illumination in fig. 3.7c

We have to choose the proper illumination considering two points: the presence of fluorescence and the distance of source collection. The optimal illumination for the light collection is at $\rho = 0$, and the collection spot coincides with the illumination spot. However, the fluorescence is strongest at $\rho = 0$. If we aim to minimize it, we should use a ring illumination to increase the SD separation, but we will lose some Raman photons due to the added travel path of the photons. When collecting at a distance from the illumination source, we need to consider also the broader FWHM of the pulse.

To obtain a ring illumination, we have to use an axicon. The diameter of the ring depends on the distance from the axicon to the image plane.

For the positioning of the illumination, mirrors will be used. It will not be at the optimal position but as a starting position for optimizing the signal.

To correctly position the light at the center of the lens or axicon, we need an x y stage. The x-direction will be needed to position the light at the center of the optical element. A y-axis will be used to position the illumination at the focus for the lens or adjust the ring diameter for the axicon on the sample.

3.3 The probe

The main limitation of both systems is how much light can be collected by the fibers as it is impossible to overcome the limit given by the theorem of conservation of radiance. The probe's aims to maximize the light collected by the fiber in reflectance given the constraints of the fibers and the detector.

The optical system of the probe is mounted on an XYZ stage that will be used to optimize the signal. The x and y-axis will be used to position the collection spot at the correct position. The z-axis will be used to adjust the focus.

Two optical systems are available that have different magnification and distances from the focus point to the lenses. The distance from the system's focus to the lens influences the numerical aperture of the overall layout, but it should also be considered for the operational use. A short lens-focus distance risks blocking the light from the injection system and making it difficult to position it on the sample.

The probes will require that the light arriving on the fiber coupler (formed by a 36 mm focal length lens) and on the filter is collimated.

Before the fiber coupler we have placed a slider where we will insert the band-reject filters.

Two-lens system

The two-lens system is formed by a 50 mm (L2) lens and the 36 mm (L1) coupling lens.

The probe's focus is at 50 mm from the lens with a magnification factor of 1.39. The light after L2, if at focus, will be collimated as required by the fiber coupler. Being collimated, the distance between L1 and L2 is not an essential parameter. The short distance of 50 mm from L2 to the sample could block the injection light and complicate the positioning of the mirrors. In fig. 3.8a we can see its optical scheme. This probe has a magnification factor of 1.4.

Three-lens system

The three-lens system is a probe optimized for the monomode fiber collection. As a first lens L1 is placed the fiber coupler with $f_1 = 36$ mm at $d_1 = 36$ mm, $f_2 = 100$ mm with any distance possible being collimated, $f_3 = -50$ mm at $d_3 = 64$ mm finally the distance form the sample should be 130 mm. This distance allows us to work at a comfortable distance to avoid interfering with the injection beam

In fig. 3.8b we can see its optical scheme. The Magnification factor is 10. That means the area collected by the fiber is 10 times than the core of the fiber.

Differences and optimal choice

The Choice of probe should be determined by two factors:

- the ease of operation

- the amount of light collected. We need to recall that the conservation of radiance imposes $MM_\alpha = 1$, where M is the image magnification and M_α is

(a) Two lens probe

(b) Three lens probe
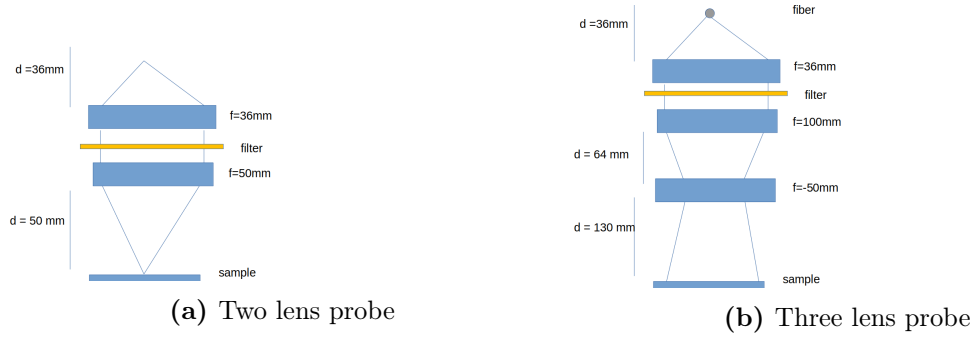
Figure 3.8: Probes optical scheme

the angular magnification. If we have a high magnification factor, we will have a low numerical aperture of the system. That means that the probes are limited by the numerical aperture and dimension of the fiber being used.

We found that we should use a far-away probe from the sample, such as the three-lens system, for ease of operation. If the probe is too close, it risks blocking the input light and the placement of the last mirror.

We have observed that the three lens probe collects more light in the seven core-bundle fiber (BFL200HS02 from Thorlabs) and about the same in the monomode fiber (780 hp monomode fiber from Thorlabs with a core size of $4.4\mu m$)

3.3.1 Band-reject filters

After the light interacts with the sample, the vast majority of photons are elastic, or Tyndall photons, scattered photons with a tiny minority of Raman scattered photons.

The elastic photons will need to be removed for three reasons:

- if a high-intensity light travels through a fiber it generates fluorescence that will act as noise, they will have the same wavelength as Raman.

- the elastic photons will saturate the detector because they can be more than $10^{10}cps$

- The cross-talk between wavelength can happen on the detector and the position of the Raman wavelength can be present the elastic Photons

Therefore we need filters to remove the probing wavelength. Four types can be used:

- Notch filter. It cuts only a very narrow region of wavelength.

- Longpass. Only higher wavelengths are allowed, and they can be used for Stokes photons. It will block anti-stokes photons

- ShortPass. Only lower wavelengths are allowed. It can be used for anti-stokes photons, will block stokes photons. (it will not be used in this thesis)

- BandPass. Only a small band is allowed. It can be used to verify that a photon has a specific wavelength

We need to note that the filter will significantly reduce the photon count for the elastic photons, but it will not reduce them to zero because a typical filter has at most an OD of 7.

It is possible to place two filters in series, but we have to be careful in removing the reflected components of both filters.

Choice of filter pair

At least two filters should be present in the setup. A laser cleaning filter seen in section 3.2.2 and a bandpass filter seen in section 3.3.1. The filters are present for two reasons:

- reduce the power of the elastically scattered light

- remove any florescent component coming from the laser

The first task is performed by the band-reject filter and the second by the Bandpass filter. To have a good performance of our spectrometer, we must ensure there is no overlap of the two allowed regions of wavelength. If there is an overlap, we could have not removed the elastic scattered light, if the probing wavelength is inside the allowed band of the band-reject filter, or not have a clean probing light.

When using the titanium laser as a source beam, we will have two other lights other than the laser. Light from the pump laser and fluorescence of the crystal.

3.4   The Spectrometer setup

An advantage of this system compared to a CCD spectrometer and the Diffuse Raman Spectrometer that we will present is its simplicity.

No additional optical elements are required for the spectrometer as the separation of the wavelength already happens in the fiber.
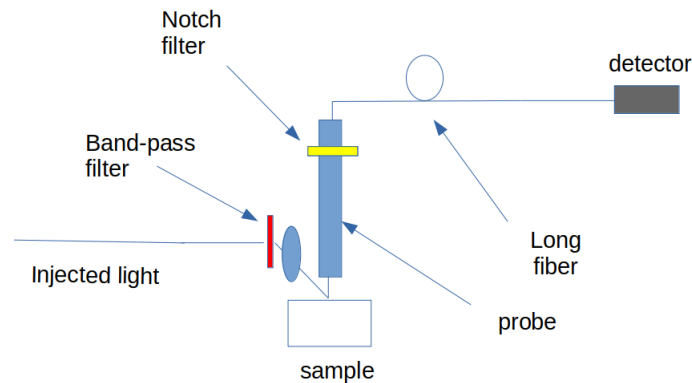
Figure 3.9: Scheme of the WTT spectrometer

As shown in the scheme in fig. 3.9 only two elements are present in this setup after the probe:

- a fiber

- a detector

With this type of spectrometer, the choice of the type of illumination is critical because it will affect the collection efficiency and the resolution of the spectrometer.

The illumination on the sample

The illumination on the material should be aligned with the collection point. As shown previously in the theoretical chapter, the further we move from the illumination source, the larger is the temporal FWHM of the green Function and therefore, the FWHM of the output pulse.

$$FWHM_{tot}^2 \approx FWHM_{Laser,IRF}^2 + FWHM_{greenfunction}^2 \tag{3.3}$$

Aiming to maximize the spectrometer's resolution, we need to reduce the FWHM of the system and so we have to collect at 0 source collection distance.

We cannot increase the source-detection (SD) distance to remove fluorescence. The increase in the SD would reduce the light collected and the Raman collected. We would have proportionally more Raman photons to the elastically scattered photons but we would have proportionally the same number of fluorescence photons. Finally we cannot use high SD separation for two reasons. The FWHM of the Green function would be large and secondly, we can collect very few photons with the monomode fiber.

3.4.1   The fibers

To obtain a good spectrometer, we need to maximize the light collected and the separation of the wavelength, therefore:

- Large core

- high numerical aperture

- high dispersion of the various wavelength

- Only material dispersion should be present. Modal and waveguide dispersion should be minimized.

A constraint on the choice of the fiber also comes from the detector. Considering the conservation of radiance, the fiber does not have to have a larger area and numerical aperture than the detector as the active area will not collect those additional photons. We have considered using two types of fiber: monomode fiber and graded-index fiber.

monomode fiber

This type of fiber is a monomode fiber optimized in the range 780-970 nm [46]. The fiber's attenuation is $3.5dB/Km$ at 850 nm, for the 300 m fiber is, therefore, $1dB$, giving an efficiency of 0.8.

This fiber has a numerical aperture of 0.13 and a core diameter of 4.4 μm. The amount of light that it can collect is very low. On the other hand, this fiber being monomode has no intra-mode dispersion and negligible waveguide dispersion, not inducing any dispersion other than the ones due to the wavelengths.

Two fibers of this type were used, one 300 m and the other 100 m long. In the experiments we used the 300 m fiber as it had three times the resolution of the 100 m one.

Graded index fiber

We have been using a GIF 50c fiber from Thorlabs [47]. This is a graded-index, multimode fiber with a core diameter of $50\mu m$ and numerical aperture of 0.2. The efficiency of the fiber at 850 nm for 25 m is 0.95.

Five 25m fibers were available.

comparing the two fibers

The monomode fiber should be preferred to the Graded Index fiber as a spectrometer due to the lack of intermodal dispersion. Moreover, on the detector side, we have a monomode fiber. Therefore, the collected light will already be limited by this fiber.

In the WTT spectrometer, the temporal FWHM of the curve is closely related to the spectrometer's resolution.

A longer fiber improves the resolution of the spectrometer because the photons will be more separated. In a multimode fiber, this is not true because modal dispersion is present.

A significant limitation of monomode fibers is the low photon collection compared to fibers with a larger core diameter.

3.4.2   Superconductive Nanowire Detector

The detector used in this part of the work is a Superconductive Nanowire Detector (SCND) from Single Quantum.

Principles of operation of the detector

The SCND detector uses a superconducting nanowire single-photon detector [11].

A nanowire is cooled using liquid helium down to 3 K in a vacuum, reaching a superconducting state, where the electric resistance is null and a small bias current of a few μA passes. When a photon arrives, it interacts with the nanowire, being absorbed. As a result, the photon will heat the nanowire, causing a breaking in the superconductivity state.

A change in the voltage will be recorded, thus signaling the arrival of a photon. after a short time, the nanowire is cooled down again to a superconductivity state, returning to the detection state.

To achieve optimal efficiency, we have to set the bias current. If the current is too low, we will be losing some efficiency from the detector because it will not lose the superconductivity state once it interacts with a photon thus, not recording the event. Instead, if we put a too large bias, reaching a critical current, the current itself will make the nanowire lose the superconductivity state.

The optimal choice is a few μA below the critical current.

Characterisation of SCND

The background counts coming from the thermal noise of the detector are close to zero if the bias current is set correctly. When the detector is covered, we cannot record any dark photons over 1 minute time.

Inside the single quantum detector, a monomode fiber optical cable with a low numerical aperture and low area is present. This fiber will send the light from the fiber presented in 3.4.1 to the active area of the nanowire detector. Due to the conservation of radiance, the area of acceptance is low. Using a larger fiber than the monomode present in the detector means wasting photons at the junction of the two fibers.

The data reported on the spec sheet [39] at 800 nm:

- System detection efficiency of more than 0.9

- Dark count rate of less than 10Hz

- Dead time, the minimum time separation for two photons, of less than 10 ns

- Maximum count rate of more than 80MHz

3.4.3   Alignment procedure

As previously explained, the spectrometer requires little alignment, except on the side of the probe. The complication of that side arises because we are using a monomode fiber with a very small core and we need to center it with the illumination.

To perform this optimization, we need first to position the illumination and the collection area close.

We used a light source from a fiber placed on the probe's output to know where the collection area is. Due to the reversibility principle, placing the system at focus, the area illuminated will be the collection area. After the two spots overlap, we need to fine-tune the collection, and for that, we have to look and maximize the elastically scattered light.

Connecting the monomode fiber to the detector when we have no filter, we need to attenuate the source light to not saturate the detector. Then we have to move the XY stage and maximize the counts seen on the TCSPC board.

Before a measurement we need to reinsert the band-reject filter and open the attenuator completely.

3.5   Post processing

The measurement is collected using a TCSPC board that returns the histogram of the photon count with the time of arrival of the photons. From this data we want to reconstruct the spectra of a sample. Firstly we need to find the calibration of the spectrometer and then secondly using the calibrated function we need to analyze the data.

3.5.1   Calibration of the system

After collecting a measurement using a TCSPC board, the data will be presented with two axes, a y-axis showing the photon counts per time gate and an x-axis showing the photon arrival time. We have stated that different arrival times correspond to different wavelengths and from the arrival time, we need to convert into the corresponding wavelength. We need to perform a calibration of the fiber to find this relation.

The calibration of the fiber has been performed using the supercontinuum laser. An IRF measurement is performed to find the time position of each wavelength. Then we connect the long fiber to the detector and different wavelengths are sent into the fiber and are collected by the detector. The source has been connected directly to the long fiber and sent into the detector without interaction with any samples.

For each wavelength, the histogram is recorded and we take the time gate with the maximum count as the reference point for the arrival of the curve.

Using a nth-order system, we have fitted a calibration curve on the arrival time curve of the wavelength. Using the Occam razor principle, we will choose n as low as possible that does not compromise on the regression coefficient R^2. We have chosen a polynomial of the II order. In figure 3.10 we can see the plot of the fitted curve on the different arrival times of different wavelengths.

3.5.2   Data analysis process

After a measurement, we need to analyze the data to retrieve the spectra of the sample. A reference measurement is required to find the relative position of the other wavelengths. The calibration is not absolute but depends on the relative arrival time to a known wavelength. The arrival time can change, even if the fiber optic cable remains the same, by increasing or decreasing the length of the detector or sync cables to the TCSPC board.

To reconstruct the spectra, we have developed a Python class called *wavelengthTroughTime*. To the class we need to pass the measured data, the reference wavelength (λ_0), and the reference measurement to the object.

Reconstruction

Being a monotone function we can compute using the inverse formula $\lambda_0 = f^{-1}(t_{0,e})$. To compute the inverse function we use from the library scipy the function fsolve. We will need to measure the arrival reference time at λ_0 that we will call
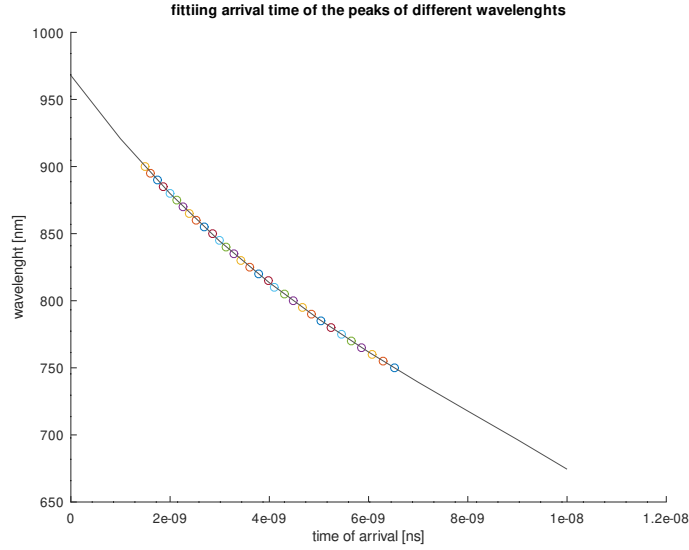
Figure 3.10: Fitted curve on the arrival time that will be used to calibrate the spectrometer, $R^2 = 0.99997$

$t_{0,m}$ and it will be taken as reference. The difference between $t_{0,m}$ and $t_{0,e}$ will give the offset needed to compute the wavelength using the calibrated function plotted in fig. 3.10.

Any possible λ_0 in the calibrated range can be chosen, but it is best to use the probing wavelength for simplicity.

We are using the calibration function from fig. 3.10 with the reference time for the probing wavelength we can convert the arrival time (ns) into the wavelength (nm) and the wavenumber.

If the elastic light is present in the sample measurement, the reference measurement can be the measurement itself. Therefore, the elastic light can be recognized as the strongest peak of the measurement.

3.6   Characterization of the system

We need to understand the main properties of this spectrometer. To have a complete characterisation we need to estimate:

- spectral range

- spectral resolution

- time integration

- spatial resolution

The characterization has been performed using the 300 m monomode fiber

Spectral Range

Two elements determine the spectral range of the spectrometer: the time window and the length of the fiber.

The time window of the photon distribution is given by the period of repetition of the laser. This is due to the working principle of the TCSPC board that measures the arrival time of a detected photon compared to the sync pulse.

The length of the fiber determines the calibration curve. This is because the delay of two photons at different wavelengths is proportional to their length. Therefore the longer the fiber, the lower the spectral range.

Our system uses a 300 m monomode fiber, with a repetition rate of 100 MHz, the time window is 10 ns, giving a spectral range of 400 nm or 4500 cm^{-1}. This is only an ideal range. Due to the time delay, some photons of the trailing edge of the elastic scattered light appear on the opposite side of the histogram giving the measured arrival time on the opposite side of the spectra. We will need to remove therefore the last few nanoseconds of the recorded pulse, giving a total spectral range of around 4000 cm^{-1}.

Detection efficiency

The element that mainly influences the detection efficiency is the fiber. The detector has an efficiency of approximately 0.9 for wavelength from 200 nm to 2000 nm[39]. The fiber instead has been optimized for the range 780 nm to 970 nm. Outside this range, the efficiency of transmission will be much lower.

We have estimated the detection efficiency using the supercontinuum laser. We firstly took an IRF measurement, connecting a short fiber to the SCND detector, and scanned through the wavelength range 750 to 1300. We then added 300 m fiber to the short fiber and scanned in the same wavelength range.

An attenuator was present to obtain the optimal light intensity for the detection. We recorded its position in both runs for all wavelengths. From the position we were able to convert into the transmission efficiency.

The efficiency has been calculated with:

$$\eta_{spectrometer} = \frac{T_{300m}C_{300}}{T_{IRF}C_{IRF}}\eta_{SQ} \tag{3.4}$$

where C are the total counts for each wavelengths and η_{SQ} is the detector efficiency of 90% From fig. 3.11 we can observe that the practical detection wavelength range goes from 750 nm up to 1150 nm. Any Raman wavelength higher than 1200 nm cannot be detected.

In the range 780 nm to 950 nm we have an efficinecy of 80%

Spectral resolution

The resolution is the most important specification of a spectrometer. For a WTT spectrometer, the spectral resolution is directly linked to the temporal resolution and is related to the ability to differentiate two separate peaks. The elements affecting the spectral resolution are :
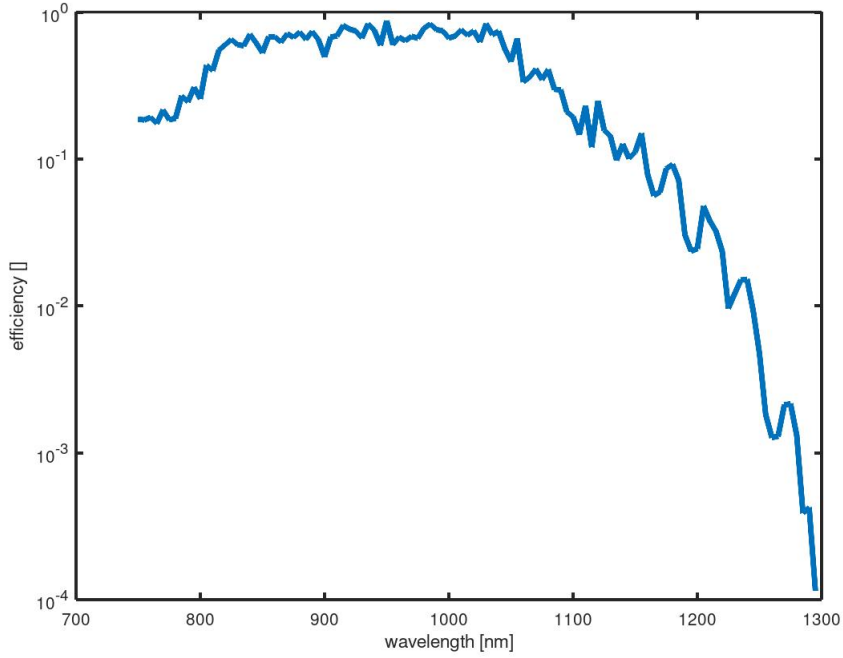
Figure 3.11: Efficiency of the fiber spectrometer per wavelength

| (a) Time axis | (b) Wavelength axis | (c) Wavenumber axis |
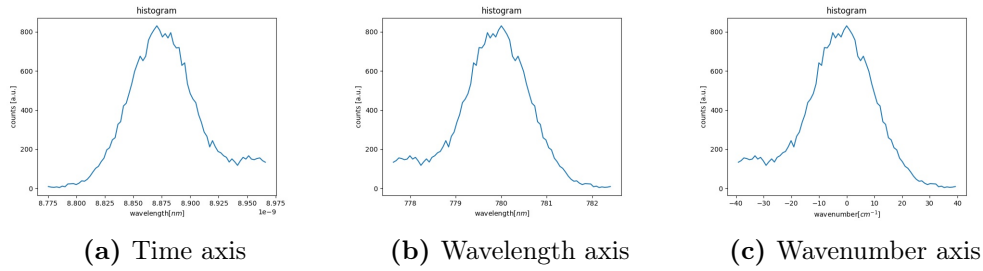
Figure 3.12: Estimating the resolution of a measurement

- temporal FWHM of the probing pulse

- position of collection, D, μ_a, μ_s, due to the propagation inside the material and can be estimated using the Green function of the sample

- spectral band of the injected pulse.

- length of the fiber

- number of channels of the TCSPC board

- intramodal dispersion

To estimate the maximum resolution, we have to look at the temporal FWHM of the elastically scattered light measured after the 300 m fiber.

Starting from the FWHM of the elastic light, unfiltered and by looking at the FWHM of the pulse after traveling through the sample and the long fiber. As seen

from fig 3.12 the FWHM in fig 3.12a is 80ps, converted into wavelength is 2 nm from fig 3.12b and in wavenumber is 20 cm^{-1} when probing at 785 nm.

The major contribution to the FWHM in the arrival time is the FWHM of the initial pulse. The laser has a bandwidth of around 0.1 nm and a fundamental limit exists between spectral and time resolution, the Fourier limit However, it places the minimum possible pulse at 10 ps.

As seen in chapter 2, if collected at null source distance, the propagation inside the material is 2 ps, negligible compared to the other the temporal broadening of the injection pulse.

Ideally, using a Fourier Limited laser at 785 nm, with 0.1 nm of bandwidth and 10 ps of temporal FWHM, we would reach a resolution with the spectrometer of 0.3 nm.

The resolution can be improved by increasing the length of the monomode fiber at the cost of the detection efficiency. The pulse will remain mostly unchanged, except for a small broadening due to the spectral bandwidth of the laser. The resolution will improve thanks to the better separation due to the added travel time. To have a higher spectral resolution and the same spectral range, it would be needed to reduce the repetition rate of the laser.

The minimum pulse dimension we recorded on a measurement was 60 ps at 780 nm that converted into nm corresponds to 1.5 nm of resolution or 20 cm^{-1} in wavenumber. This means that the maximum resolution of the system is 1.5 nm.

We need to note that in the wavelengths lower than 750 nm the fiber is no longer monomode and we will lose in the resolution if we operate in this spectral region.

Time integration

The main factors determining the temporal integration required are the Raman efficiency of a material, the power of the injected laser and the collection efficiency.

We have qualitatively observed that the minimum integration time for strong Raman emitters, such as marble, is 10 s with a laser power of 100 mW.

Spatial resolution

the spatial resolution is given by the area of collection. The area of collection is given by the probe magnification factor and the core dimension of the fiber.

We will use a monomode fiber of $5\mu m$ and a probe with the magnification of 1 or 10. giving a resolution of $50\mu m$ with almost no probing depth capabilities

3.6.1 Noise

The noise is caused by the fluorescence of the laser crystal, the pump laser, fluorescence of the sample and light from the room.

Those noise terms are, compared to the ps scale, a constant background. When using a CCD spectrometer, the background noise comes from the broadband of the fluorescence. When using this method, the noise arises from the broad temporal distribution.

Another possible source of noise is the reflection happening inside the probe or in the 300 m fibers caused by defects of the fiber or some stresses applied.

3.6.2 Comparison to a CCD spectrometer

Comparing this spectrometer to a normal CCD camera spectrometer shows a clear disadvantage of this system, with the only advantage being the simplicity of the setup. The main limitation is the area of collection limited by the dimension and numerical aperture of the monomode fibers due to the conservation of radiance. A spectrometer that uses a CCD camera divides the light in the wavelength component with a grating, and the fiber that can be used is much larger. Depending on the spectrometer, it is possible to use a linear to circular fiber bundles with a core diameter of the order of mm of diameter. The light collected will be $(\frac{1mm}{4.4\mu m})^{\approx}5\ 10^4$ more than our system.

If we compare the two systems using the same type of fiber, our system has some advantages. The detection efficiency in a CCD is comparable with the Single Quantum detector only in a small wavelength region. The Single quantum has a near-flat efficiency of more than 0.8 in the wavelength region from 200 nm to $2\mu m$ where the CCD cameras only in a few hundreds of nanometers have this high efficiency. The limitation in our system is the efficiency and dispersion of the wavelengths in the fiber. It also has the advantage of lower dark counts. We will take as a reference a CCD from Hamamatsu [17] that has 6 dark counts per second. In the single quantum, we measured to be around 0.1 cps. The limitation of the current system appears when we consider the resolution term-limited by the FWHM of the time pulse. The theoretical limit of the resolution can be placed around 0.2 nm at 785 nm with a Fourier limited pulse and a 300m fiber, by increasing the fiber length, the resolution can be improved using a laser with a smaller band.

The future application of this technique could be promising if a bundle of monomode fibers is used.

- a Raman camera can be made using N fibers that parallelly measures on the sample and are recorded by N detectors

- By using a bundle of fibers on a larger detection area, we can collect significantly more light and we could match the efficiency of a CCD Spectrometer

3.7 Raman Spectra

In the previous sections, we explained how we developed the fiber Raman spectrometer and explained its characteristics. In this section, we will prove that our setup can perform Raman spectroscopy and then present some of our results.

3.7.1 Powder samples

Calcium Carbonate $Ca(CO)_3$

As a first step, we measured some Calcium Carbonate $Ca(CO)_3$ powders fig. 3.13. This material has been chosen because it is a strong Raman emitter, it is well
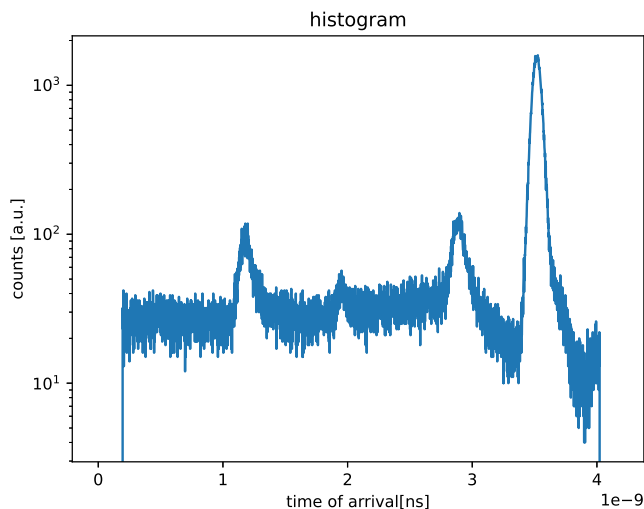
Figure 3.13: $Ca(CO)_3$ powder, raw measurement. The x axis shows the arrival time. The measurement performed with 785 nm probing wavelength and with 100s integration time. Power of 100mW

known in literature and highly scattering, making it ideal for this experiment.

We first notice the presence of four peaks. The right one is the elastically scattered light at 785 nm because it arrives simultaneously as the unfiltered light and has the highest photon counts as seen in fig. 3.14. Raman scattering possibly causes all the other peaks scattered photons, but we need to prove it, at least for the first measurement. The main characteristic of Raman peaks is that they have different wavelengths. Firstly we need to convert the time axis into wavelength and wavenumber in fig. 3.15, to more clearly recognize the Raman shift, we need to remove the elastic light and we can convert into the wavenumbers.

To understand if the result is correct we need to overlap the spectra we obtained and the one given from literature. From fig. 3.16 the two results seems to agree except for the 1086 cm^{-1} and the 700 cm^{-1} peak that have a small shift. This is likely caused by incorrect calibration of the spectrometer used to calibrate the fiber or by the uncertainty on the wavelength of the probing laser. The calibration process is critical in most Raman processes, it is common to encounter this problem. It is possible to calibrate using some known Raman spectral band. To prove beyond doubt that the wavelength is a Raman wavelength, we have to use a different filter that selects the Raman wavelength and removes any other wavelength. We have took as an example the $1086cm^{-1}$ shift that with a probing wavelength of 780 nm will correspond to a Raman emission at 852 nm and it will be possible to use an 850 10 nm bandpass filter selecting only this peak. From fig. 3.17 we can see that all other peaks are not present and the sole remaining peak is the one at $1086cm^{-1}$ in the same position.

Characteristic

The spectral range of this measurement has been limited by setting the gain
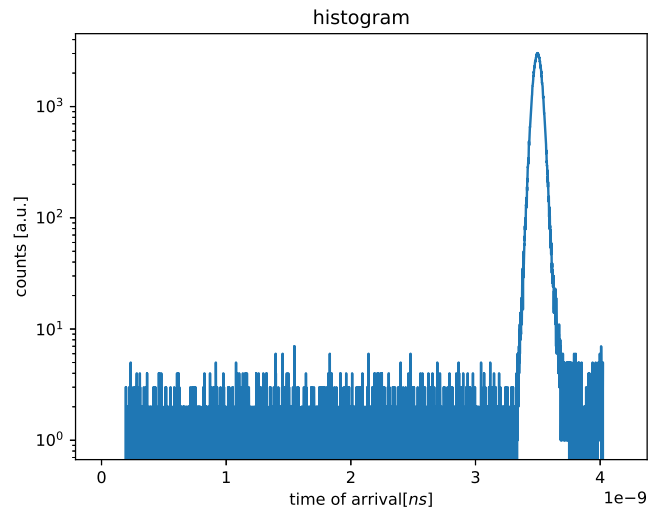
Figure 3.14: Unfiltered light
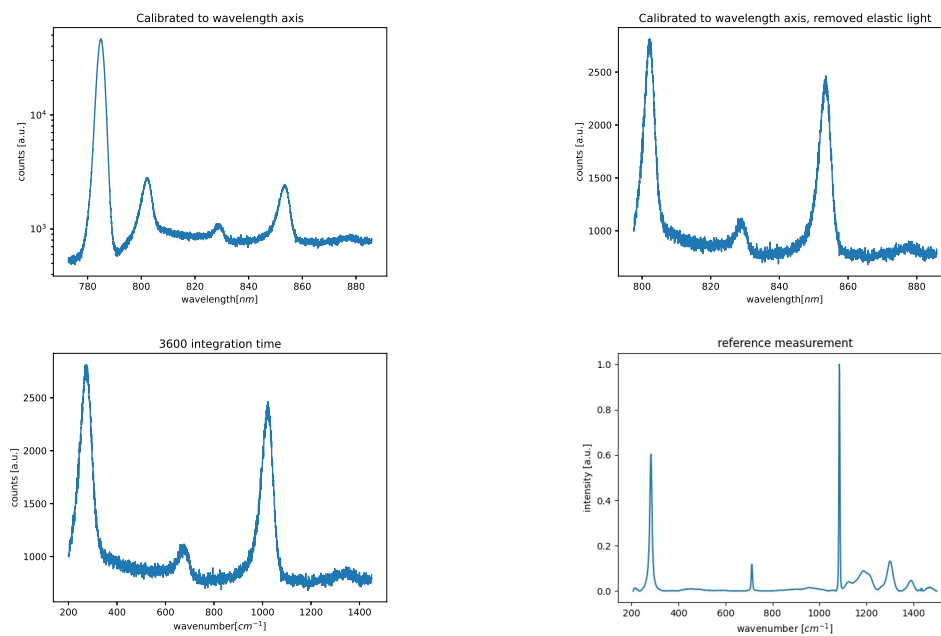
Figure 3.15: $Ca(CO)_3$ powder. power of 100mW, 3600s integration time. 785 nm wavelength probing light. The reference wavenumber data is taken from https://rruff.info/Calcite/X050035
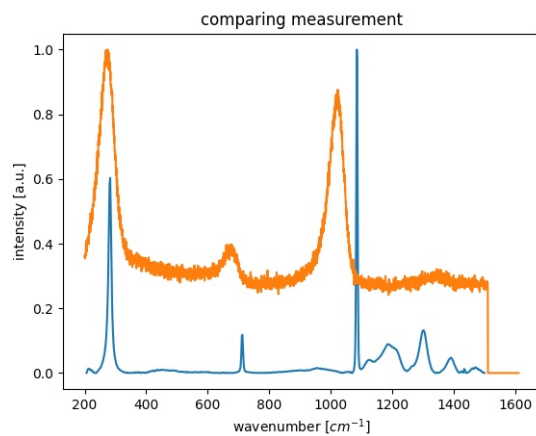
Figure 3.16: Comparison of our result and a reference measurement
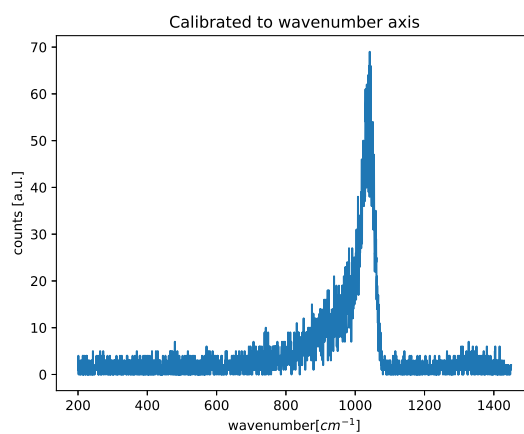
Figure 3.17: $Ca(CO)_3$ powder. Used a 850 10 filter and laser power of 100mW, 100s integration time.
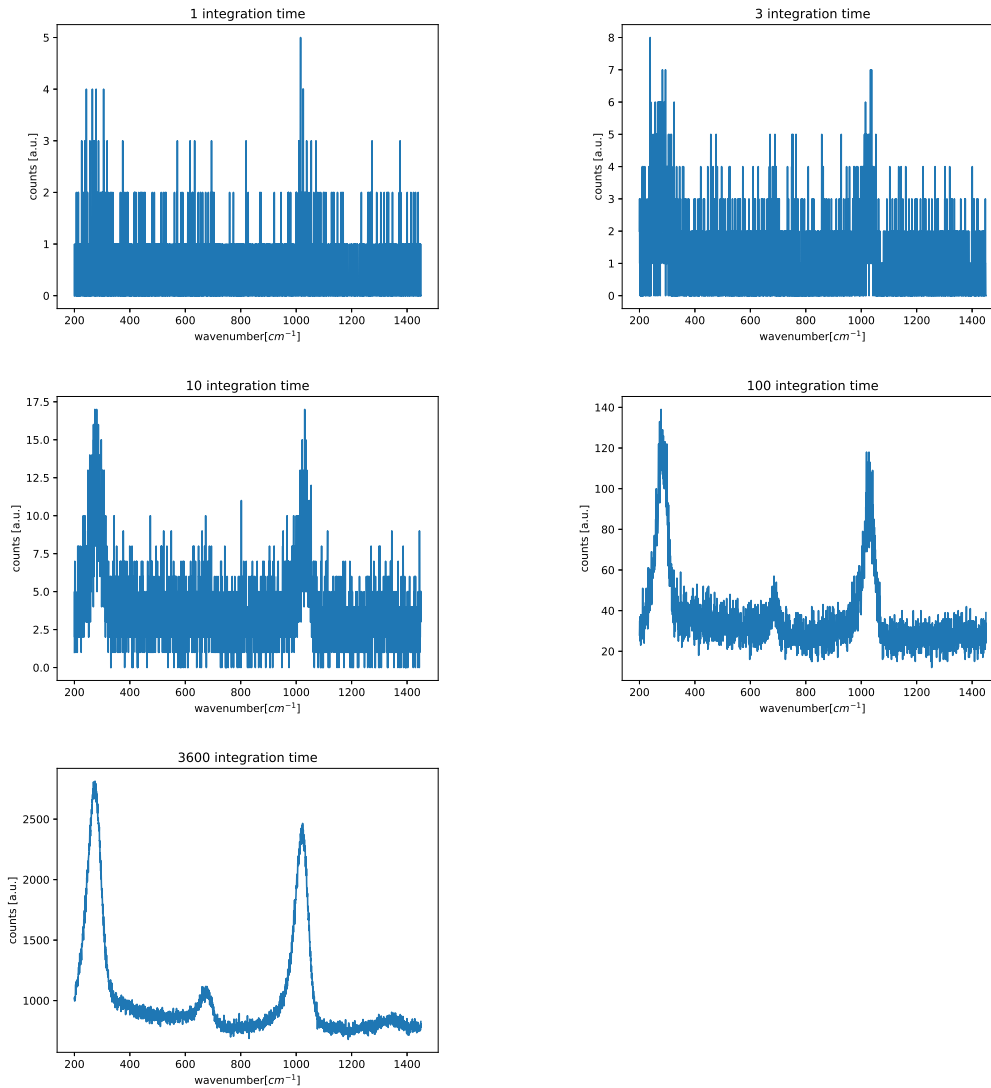
Figure 3.18: $Ca(CO)_3$ powder, power of 100mW. 785 nm probing wavelength

of the TCSPC board at 12. Having a higher gain does not give a higher resolution, but we have done it to focus our attention on this wavelength range that was the one of interest for the shift according to the known spectra.

The measurement has a FWHM of 200 ps, converted is 5 nm and in wavenumber, it corresponds to 90 cm^{-1}.

Time integration

A higher time integration will correspond to a higher signal-to-noise ratio. The main element of noise with low integration time is the Poisson noise cause by the quantized nature of photons. We can see from fig. 3.18 the different integration time and we can qualitatively see that the signal-to-noise ratio improves.

Qualitatively the minimum integration time for distinguishing the peaks is 10 s when the laser has a power of 100 mW
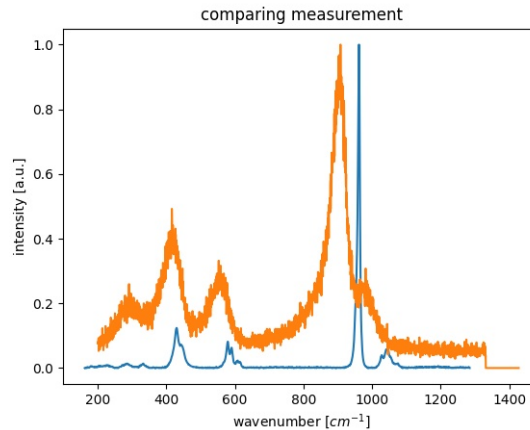
Figure 3.19: Comparison of our result with a reference measurement taken from rruff.info

Hydroxy Apatite

Hydroxyapatite, $Ca_5(PO_4)_3(OH)$ is a mineral and it is a common mark of malign calcification formation in breast cancer.

Comparing our results with the literature, we can confirm again that we are actually measuring the Raman signal.

From fig. 3.19 we can see that again there is a small shift of a few cm^{-1} with respect to the known spectra.

3.7.2 Spectroscopy on diffusive materials

When measuring on a diffusive sample, we have the additional complication of the added travel time inside the material that increases the FWHM of the measurement and decreases the photon collection. The materials we will present are no longer pure and composed of a single molecule but can be composed of multiple molecules.

Marble
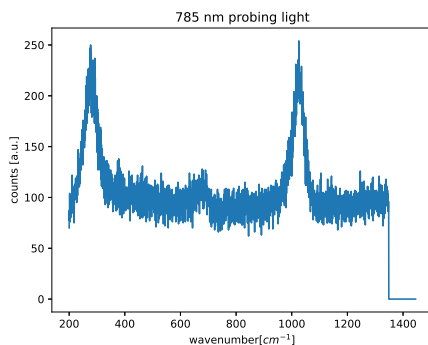
(a) Using 785 nm probing light
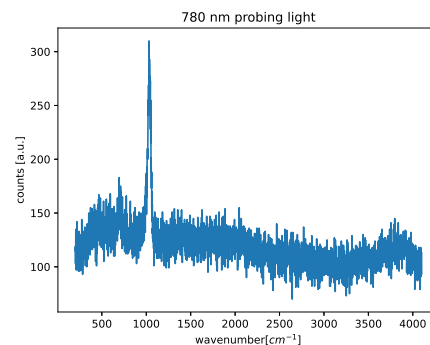
(b) Using 780 nm probing light

Figure 3.20: Marble block.
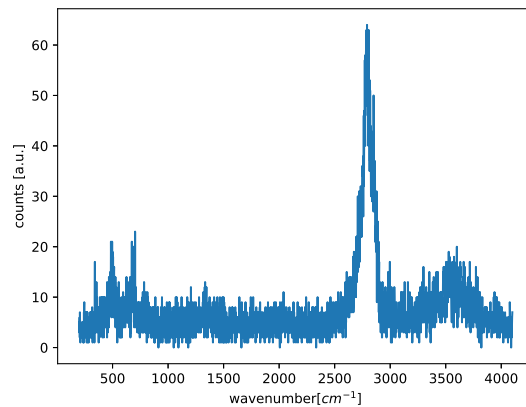
Figure 3.21: Silicone, 20 mW of power, 100s integration time. 780 nm probing light
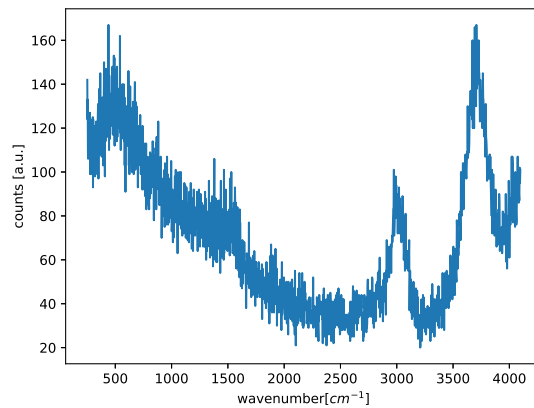
Figure 3.22: Lard, 20mW of power, 100s integration time. 780 nm probing light

In fig $3.20a$ we can see the 200 cm^{-1} peak that is not visible on fig. $3.20b$, this was caused by a different notch filter used to block the elastic light and a slightly different wavelength used. The two have a different range because we have used different gain on the TCSPC board. The marble spectra are very similar to Calcium Carbonate because it is composed of the same molecular structure. This result confirms the possibility of using this technique on diffusive samples.

Silicone

From fig. 3.21 we can see that the Silicone has a 3000 cm^{-1} Raman shift. This peak is similar to the lipid peak and therefore, silicone can be used as a phantom to simulate the presence of fatty tissue.

Lard

From fig. 3.22 we can observe a curve with a very large FWHM and two sharp peaks. The sample's fluorescence causes the curve with a broad temporal profile, and it is of no interest for us, and it will be a noise term in our measurements. In

the case of Lard, we can see the presence of fluorescence in the sample in the early wavenumber and two possible Raman peaks at higher wavenumber . One at 2900 cm^{-1} is caused by the lipid presence and the second one at 4000 cm^{-1} could be caused by the presence of water.

Plastics

Measuring the Raman from plastic could help differentiate the different types of plastic for improving its recycling. In fig. 3.23 we have a different measurement of different kinds of plastics. From this measurement, we could only detect for some a peak at 2900 cm^{-1} and no Raman. This Raman shift is present in most Plastics, but it has not a high amplitude in polystyrene see ref. [37]. Plastic should be recognized by looking at the spectral region lower than 1500 cm^{-1} and most work in the literature focus on this region, but we are not able to recognize any feature. The fact that we could not record any of this shift could be caused by poor alignment, low integration time, low power of the laser, the presence of flourescence dye or the lack of the precise composition of the material.

3.7.3   In-Vivo

We took the measurements on the arm of a subject at different locations. In all the measurements, we could observe high fluoresce and in most samples, we could recognize two sharp peaks that could be Raman. From fig. 3.24 we see that 3.24b, 3.24d, 3.24e could have a Raman emission at 2700 cm^{-1} and at 3300 cm^{-1}. Looking at the Lard measurement in fig. 3.22 we see that it has the emission close to 3000 cm^{-1}. The 3000 cm^{-1} region is a very common Raman shift position for biological molecules. We can notice that these regions can be high in the concentration of fat. According to ref. [19] 3000 cm^{-1} shift comes from the proteins and lipids. And in fig. 3.24e according to [13] the 3000 cm^{-1} shift it is caused by the keratine of the fingernails.

The high background is caused by the fluorescence of the skin and by the biological tissue. ref. [13] and [19] report of multiple shifts present in the region lower than 2500 cm^{-1} that we were not able to measure given the high background.

(a) Bottle cap plastic (PP)

(b) Lens container (PET)

(c) Polystirine packaging (PS)

(d) Plastic bag PE

(e) Plastic Bubble wrap LDPE

(f) PVC film
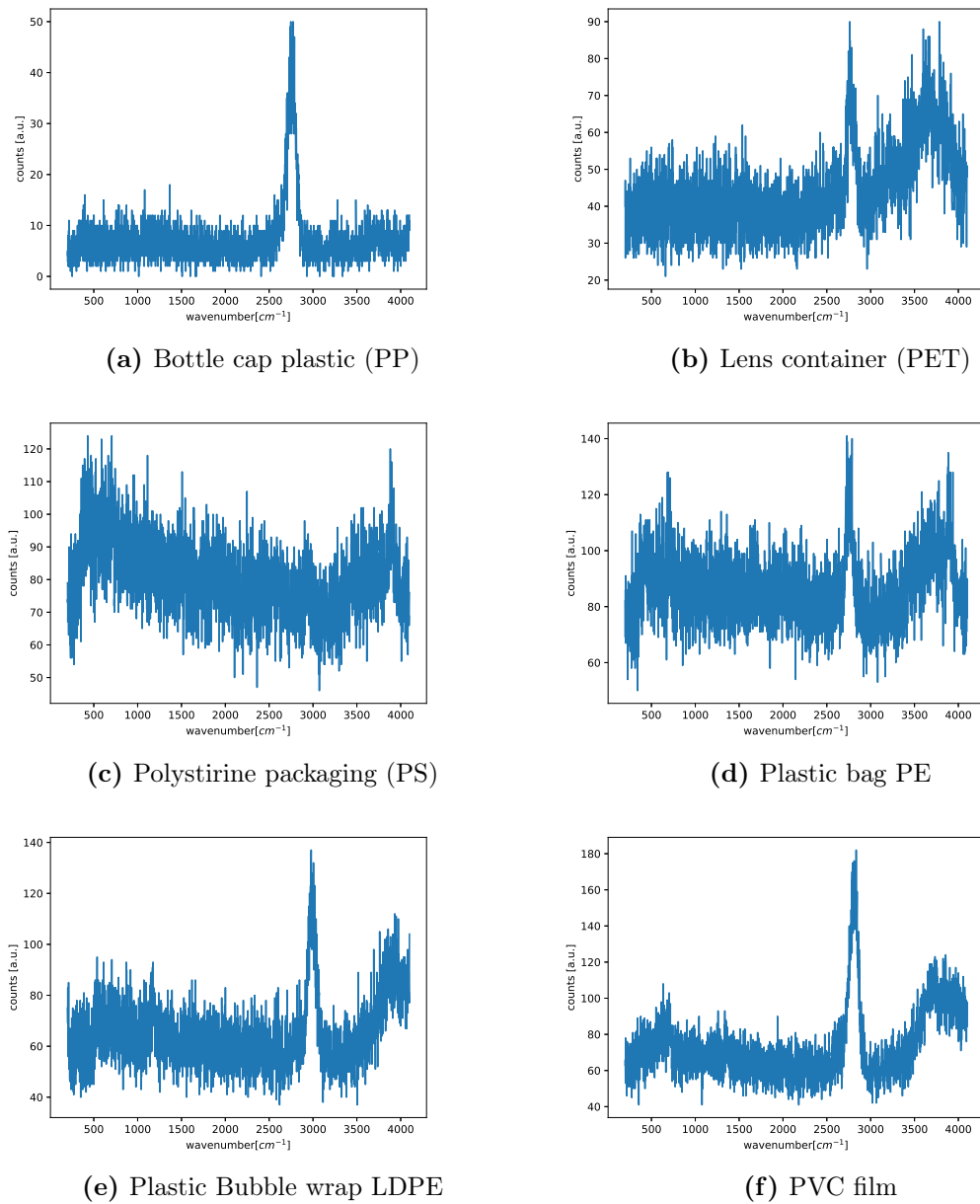
Figure 3.23: Different types of plastics. Power of 20mW using 780 nm probing light with 1000s integration time

(a) Back of hand

(b) Hand palm

(c) Wrist near bone

(d) Forearm near elbow, fat region

(e) Finger nail

(f) Thumb knuckle

(g) Forearm internal side
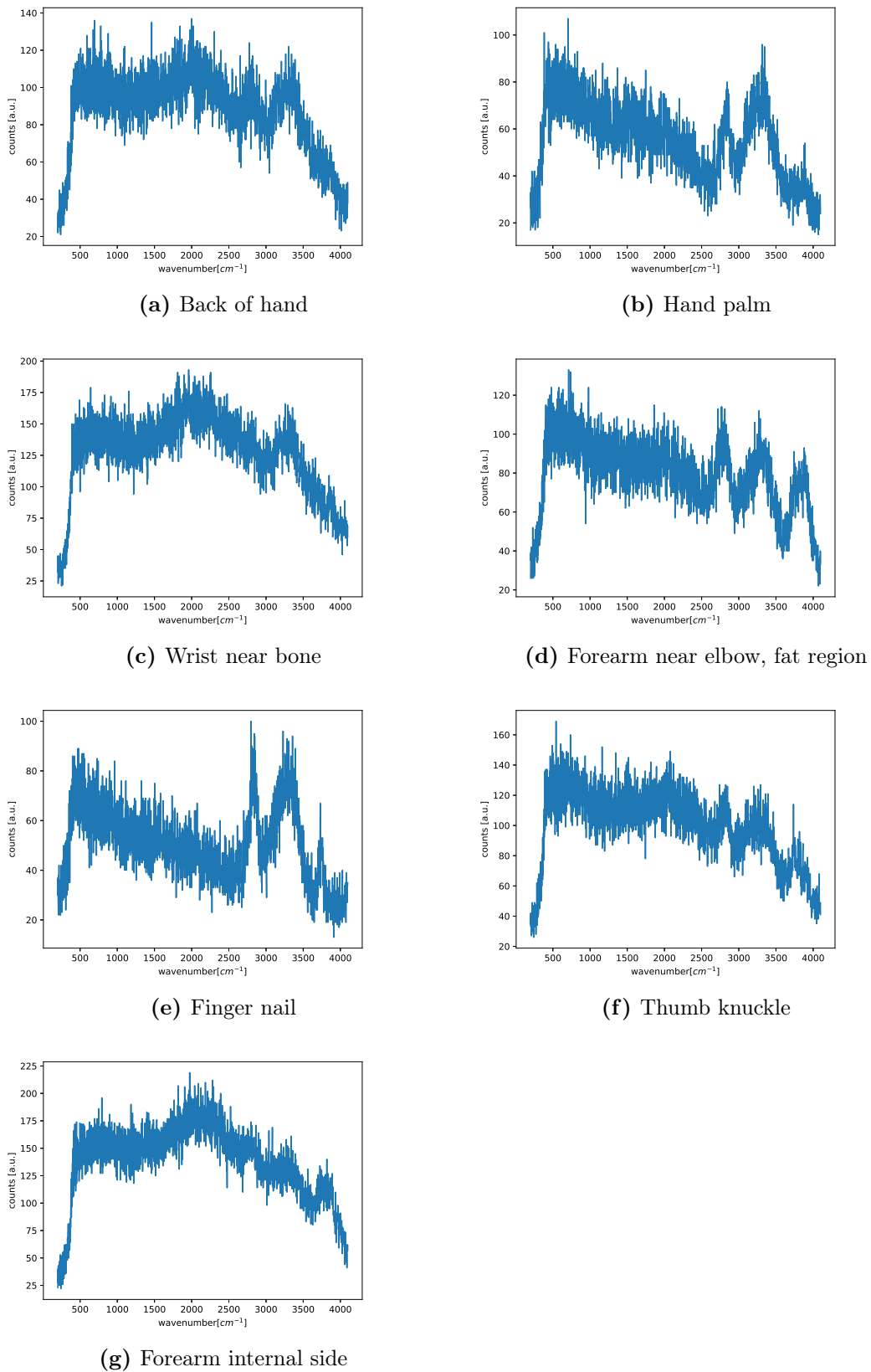
Figure 3.24: In-Vivo. Power of 20mW. 780 nm probing light with 300s integration time

3.8   Conclusion

We have developed a new type of spectrometer for Raman scattering. The spectrometer with our laser source can resolve 1.5 nm but can be improved if a laser source with smaller temporal FWHM is used. The main advantages of the spectrometer are its simple setup that requires aligning only the laser source on the collection point and its high spectral range.

With this spectrometer, we measured several spectra to verify its capabilities for Raman spectroscopy. In particular, we tested this approach on diffusive samples and on an in-vivo subject where we could retrieve some Raman shift.

Chapter 4

Compress Sensing Time-Domain Spectrometer

A diffuse Raman spectrometer was constructed in previous works and during this thesis, we finalized the spectrometer for an in-vivo measurement. The design of the spectrometer follows what has been proposed by Berto et al. [6] and his novel use of a single-pixel camera and a Digital Micromirror Device (DMD) making use of compressive sensing techniques. The diffuse Raman spectrometer exploits the temporal profile of the Raman signal to reconstruct the depth from the detection position. The same setup can also be utilized for time-gated Raman to reject the fluorescence of a sample better. This spectrometer makes use of the same illumination and probing setup as the one discussed in chapter 3.

We finalized the existing system in several key aspects, such as improving the detection efficiency by optimizing the collection source and significantly reducing the spectrometer's noise by building a PVC case to the setup, covering the detector and DMD to remove all unwanted illumination. Our main contribution was improving the control of a Digital Micromirror Device, developing a controlling program and synchronizing the device with the TCSPC board to allow faster measurement times. Having developed this program, the spectrometer can be aligned more quickly and it allows for faster and more precise measurements than previously possible. The compressive sensing approach had already been implemented, but we improved the results with the synchronization of the DMD to the TCSPC board and different reconstructions algorithms. We finally performed some in-vivo measurements and improved the measurements from bi-layer (Silicone and Marble) phantoms.

4.1 Principle of operation of the spectrometer

This detector aims to measure both the spectra and the pulse shape of each wavelength using a single-pixel detector. From the spectra, we can understand the Raman shift and, therefore, the molecular composition of a material and from the temporal profile, we can understand the origin depth of the Raman signal. Thus, we need an element to separate the light in its wavelength components and a detector to measure each wavelength's arrival time. We made use of compressive sensing techniques to improve the speed of collection by measuring parallelly multiple
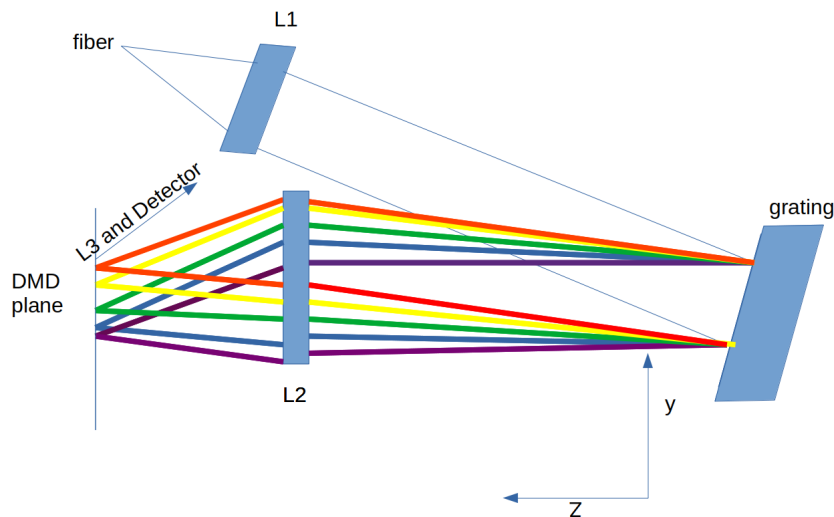
(a) Optical scheme from the fiber to the DIgital Micromirror Device (DMD)
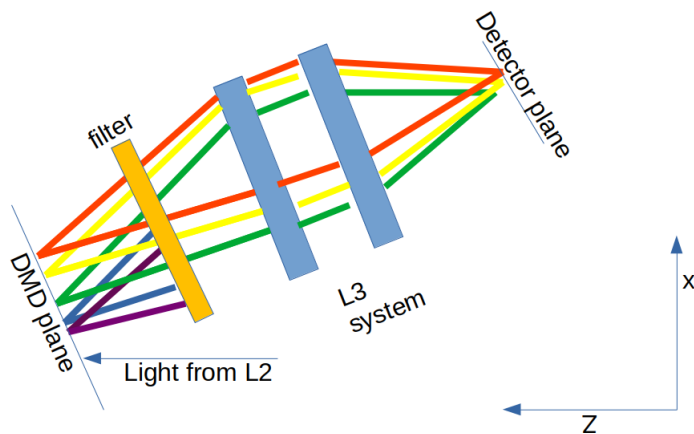
(b) Optical scheme from the the DMD to the Detector

Figure 4.1: The optical scheme of the Time domain Raman spectrometer

wavelengths.

We will now present the detector and Digital Micromirror Device and explain the ideas of compressive sensing. Then explain the function of each optical component and the properties of light. In figure 4.1 we present the general scheme for the spectrometer.

The detector

We have been using a hybrid detector (HPM 100-50 [4] [5] from Becker-Hickl) that uses components from Hamamatsu. It is called hybrid because it combines the technology of amplifications typical to PMT and as an active area a semiconductor such as in avalanche photodiodes. The detector has an active area of 6 x 6 mm^2, with a square shape positioned at a 45° angle with respect to the Detector casing. The detector has high efficiency of 10 % up to 850 nm. From 850 nm it starts rapidly to decrease and at 900 nm it has an efficiency of 1 % as seen from fig 4.2. Since Raman has a very low efficiency, any Raman wavelength higher than 900 nm
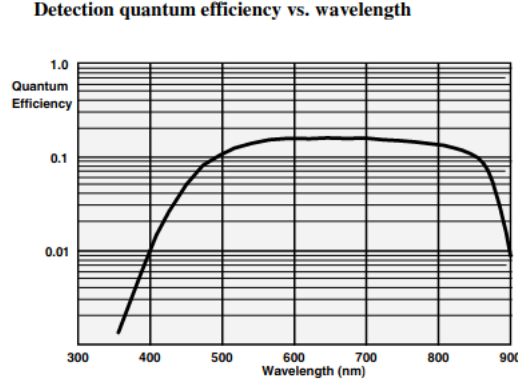
Figure 4.2: HPM 100-50 Detector efficiency plot. Taken from [4]

will not be detected.

Digital Micromirror Device

A *Digital Micromirror Device* (DMD) will be used to select the wavelength to be recorded by the detector. The DMD permits to show a pattern by rotating individual pixels of a matrix of micromirrors. We can control the pattern shown using a program written by us and the DMD will show a pattern desired by the user. The DMD is the only element in the setup that we will control during a measurement. We have been using the model DLP6500 evm [20] from Texas Instrument with the reflective area of 16mm x 5 mm and 1920px x 1080px pixel. The pixel of the DMD activated will rotate by +12° and send the light to the detector and the detector will be able to record it. The remaining light will be sent in the detector's opposite (-12°) direction, removing the photons.

4.1.1 Compressive Sensing in the Single Pixel Time-Domain Spectrometer

The use of Compressive Sensing significantly reduces the acquisition time of the system by changing the basis of measurement on the DMD as in ref. [6].

A measurement on the DMD can be expressed as

$$\mathbf{S}_m = \mathbf{M}\mathbf{S}_\nu \tag{4.1}$$

Where $\mathbf{S}_m$ is the measured number of photons on the measurement matrix, $\mathbf{S}_\nu$ is the spectral distribution of photons on the DMD plane and $\mathbf{M}$ is the measurement matrix.

We want to reconstruct $\mathbf{S}_\nu$, the spectral intensity and we can only change the basis of measurement $\mathbf{M}$.

Three possible measurement bases can be used:

- Monochromator mode or line scan that will be referred to as raster scan

- Full Hadamard basis

- Hadamard Basis and Compressed sensing

Monocromator mode

The monochromator mode uses a trivial set of bases that correspond to the identity matrix. This is the most trivial method.

In this modality, *a line is illuminated for* $\frac{1}{n_{basis}}$ *of the time* and if we want to increase the resolution of the system, by increasing n_{basis}, we do it at the cost of fewer photons per second per line. If we have a sparse signal, by choosing a priori the lines to be illuminated it could be useful but a priori we need to know what lines have the Raman photons

Hadamard mode

the Hadamard matrix is defined as

$$\mathbf{H}_n \begin{pmatrix} 1 & 1 \\ 1 & -\mathbf{H}_{n-1} \end{pmatrix} \tag{4.2}$$

where $\mathbf{H}_1 = [1]$

The matrix form a complete set and the basis of the system are the lines of the Hadamard matrix. The set of basis is complete and therefore it is possible to represent any measurement on it. We will be using a modification of this matrix that is $\mathbf{H}^* = \frac{\mathbf{H}+1}{2}$ that is still complete.

Using this method, *every line will be open 50% of the time.* A single line will be acquired significantly more time, increasing the photon collected and not compromising the spectral resolution. It is advantageous if the signal has a very low photon count, such as a Raman signal coming from depth.

Such a set of bases, using some particular ordering, are capable of sub-Nyquist measuring. However, in this project, it will be used as a method to improve the acquisition time. We will not use sub-Nyquist techniques because we are interested in the long integration time of the Raman spectra. An ordering method called cake cutting from ref. [48] has been implemented, but it has not been used during the thesis for Raman measurements. We will be using the full Hadamard matrix in our measurements.

4.1.2   Optical system layout

The fiber

A circular to linear fiber bundle with seven cores (BFL200LS02 model from Thorlabs). The fiber is used to transfer the light from the probe to the spectrometer. Each core has a diameter of $200\mu m$ with numerical aperture of 0.2. We have used a circular to linear fiber instead of a circular to circular because it reduces the image on the DMD, thus improving the resolution. The fiber will be needed to be positioned carefully to minimize the image in the y-direction on the DMD. The advantage of using a single fiber with a large core would have been its high numerical aperture but would be limited by the low aperture of the lenses, therefore not improving the light collected. The other end of the fiber is circular, with a diameter of $640\mu m$, as it is the optimal shape for collection. The limiting factor for the spectrometer resolution is the dimension of the single fiber of $200\mu m$. Each

pixel of the DMD has a dimension of $7\mu m$. The fiber has a metallic coating and to avoid any accidental contact with the electronics of the DMD, it has been wrapped in a plastic film.

Fiber to L1

When the light from the fiber becomes a free beam, it is diverging. L1 is placed to collimate the light. To obtain this condition, we need to use a lens with focal length f_1 equal to the distance fiber lens d_1. If the distance is different from the focal length, the magnification factor on the DMD plane will be modified as we will discuss in 4.1.2

To reduce the dimension of the image of the fiber is possible to use an aperture slit of size smaller than the fiber. It will reduce the spot size on the DMD plane, but we would have worse collection efficiency.

L1 to Grating to L2

The beam after L1 is collimated. It will encounter a grating that will separate the wavelength components in multiple modes of dispersion. Each wavelength will have a different angle compared to the incoming beam. We will be selecting the mode with the highest intensity. The other modes will have to be considered as losses of the spectrometer.

The angle of the light with respect to the optical table can be changed by changing the grating's angle. We want the central wavelength selected to be parallel to the optical table. L2 can be placed in any position we want in the y-direction because the beam is collimated and will make no difference in the image it produces. The positioning on x, z and the angle of the lens to the beam is critical for aberration.

L2 to DMD

The image of the beam after L2 will be positioned on the DMD plane. Its dimension in the z-direction will determine the resolution of the system. This is because the grating disperses the wavelengths in the z-direction and we consider each line a different wavelength on the DMD, as shown in fig. 4.3.

The magnification factor of the image of the fiber on the DMD plane is equal to:

$$M = \frac{f_2}{f_1} \tag{4.3}$$

L2 has a $f_2 = 100$ mm and $d_2 = 100$ mm the image on the DMD will be a 1 to 1 representation of the fiber. This is the reason for using a linear fiber for injecting light into the spectrometer. The area of collection is maximized on the probe side where a circular shape is an ideal collection, and on the DMD plane the y-direction is minimized

Using a lens with a shorter focal length would the spectral resolution of the system, but we need to consider the small angle of reflection from the DMD of 12.5°. If a lens with a too short focal length is used, the DMD will have to be placed closer to the lens, considering the small reflection angle will not allow the light to
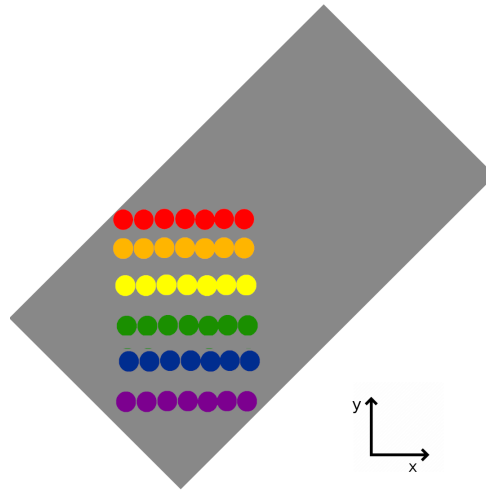
Figure 4.3: Example of images on DMD from multiple wavelengths
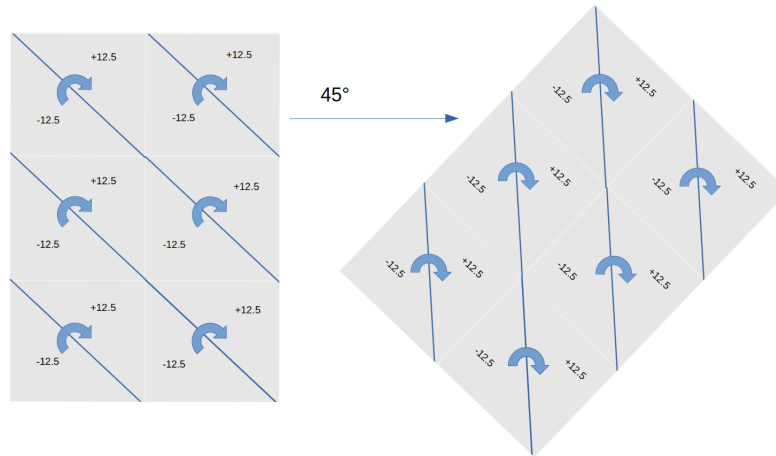
Figure 4.4: The axis of the single mirrors is at 45° compared to the sides of the DMD

reach the third lens. With this configuration, we need to place the DMD at a small tilt with respect to the incoming beam to reach L3.

To quickly place the DMD on the focal plane of the L2 lens, we place the DMD on a mount designed by us. The DMD will need to be placed at a 45° angle because, as seen in fig. 4.4 the individual pixel can move on a 45° angle compared to the vertical axis.

DMD to L3 to the detector

The light after the DMD is diverging and is collected by L3. Before L3, a filter can be placed to remove any unwanted wavelengths, such as any remaining elastic light or light from the room, as seen in fig. L3 comprises two lenses, one with a focal length of 100 mm and the other with a focal length of 50 mm. The first needs to be facing the DMD and the second the detector.

This optical system has a magnification factor of 0.5 using eq. 4.3.

We will have an image of the DMD plane on the detector plane with a magnification factor of 0.5. On the y axis, we will have the various wavelengths as shown
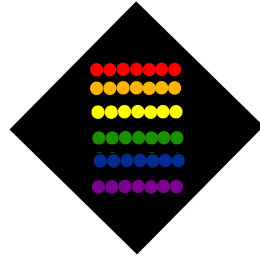
Figure 4.5: Example of wavelength position on the detector

in fig 4.5. The image on the detector of the fiber will have a size of approximately of 100 μm x 700 μm. The detection system will be covered by a cloth and have the only point of access for the light through the filter.

Fine tuning of the system

It is possible to place L1 with a distance different than the focal length of the lens. If $d_1 < f_1$ The beam after the lens will be diverging and on the DMD plain, we will have a magnification factor smaller than 1. Two problems appear:

- increasing the aberration on the image on the DMD plane due to the aberrations caused by L2

- losing photons due to the low numerical aperture

The aberration problem can be solved by inserting an iris before L2 to block the photons that reach the edges of the lens, but this will further decrease the system's numerical aperture. If $d_1 > f_1$ the beam will be converging after L1, we will not have fewer aberration problems because it is easier to center the beam on L1, but we will have a magnification factor greater than 1 on the DMD plane, thus reducing the resolution. In fig 4.6 we have the magnification factor on the DMD plane as a function on the position of d_1.
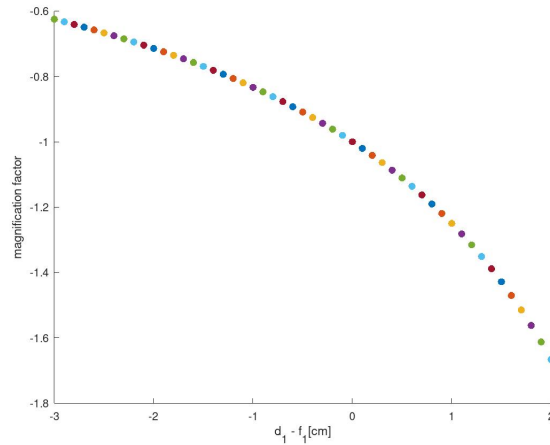
Figure 4.6: Magnification on of the image of the fiber on the DMD plane. d_1 is the fiber lens distance and f_1 is the focal length of L1. The magnification is negative because the image has a π rotation.

4.2 The DMD

The DMD is the optical element used to select the wavelength that will reach the detector. The Digital Micromirror Device (DMD) is formed by a matrix of mirrors that can be turned electronically.

We will explain the implementation of a custom program to control the DMD and synchronization to the TCSPC board to improve the measurements' speed and precision. We will finally explain a new DMD mount that we built for improved precision in the alignment.

4.2.1 The DMD control program

During the thesis work, a good portion was dedicated to developing a C code that could communicate with the device.

The code is a translation into C of two python codes:

- PyCraft6500 [36]

- DMD ScopeFoundry [33]

C has been chosen because the code will be integrated into a custom software called TRS that has been written in C.

An advantage of our program compared to the ones written in python is that the speed at execution time will be reduced thanks to the fact that C is a compiled language and python is an execute language.

When then sent a trigger signal generated by the DMD to the TCSPC board to synchronize the measurement. This, compared to the previous setup, greatly improved its speed and reliability for the reconstruction.

We will give a general overview of the code available on Github, https://github.com/alebossi96/dmd in table 4.1 we will present the most important functions.

function name	scope
getBasis	the entire set of images is generated given the required information on the type of basis, Hadamard or raster, the dimension of the basis, the number of measurements to be performed, the angle of the image, either 0° or 45°. The entire set is composed of 1-bit images. The on-state directs the light to the detector and is represented by a 1. The off-state sends the light away from the detector and is represented by a 0.
defineSequence	Receives input the patterns and parameters such as time, repetition, a trigger and here we divide the set into various batches of 24 images. The 24 images are saved into a 3 bytes char array for each pixel, 3 bytes corresponds to 24 bit and the communication data is prepared by calling the other functions.
new_encode	The batch is compressed using a method called enhanced run-length-encoding [15], which reduces the size of the data to be sent. Two versions of the encoding function are present. One from DMDScopefoundary and the second from PyCraft6500. The version from PyCraft6500 is the one that will be used.
definePattern	The pattern is then prepared, giving the information on duration, trigger and dead time between each pattern.
configureLUT	set the repetition mode
checkForErrors	performs the error correction on the DMD
startSequence	start a sequence
stopSequence	stops a sequence repetition

Table 4.1: Notable functions of the program

Name	Scope	Use
Raster Scan	perform a line scan	during the alignment and measurements
Hadamard scan	scan using the Hadamard basis	during measurement. The data collected requires to be further analyzed
all open	All the mirrors of the DMD are open	during the alignment phases
mirrors closed	no light should be hit the detector	used to check the background noise coming from the outside of the spectrometer
Bandpass filter	A line chosen by the user is opened at a chosen position	
notch filter	line is closed at a desired position	

Table 4.2: Different types of pattern implemented in the function getBasis.

All the data is processed and the communication data is stored in several arrays in the computer RAM. The choice has been made to store it in the computer temporarily instead of sending it directly to the DMD because the elaboration of the data can require up to 30s per set, which could add an extra dead time if operated one batch at a time instead of continuous repetition. The problem with this method is the high RAM usage that should be optimized in a future version of the program.

The 1-bit pattern is compressed into a string of hexadecimal values [15] in a format readable by the DMD and sends them to the DMD using a library called Hidapi to handle the USB communication.

A set of patterns can be shown for a predefined number of times or in repetition mode. In repetition mode, the set is shown in a loop until a stop pattern signal is sent. Otherwise, it can be possible to show one batch of images at a time if it is too large for the memory of the DMD, the batch size for the communication can be chosen but the ideal dimension is 24 or an integer multiple due to the limit imposed by the storage of the Images presented 4.2.1.

After programming this function, a command-line setup is implemented in the function *main* to set the parameters before a measurement run rapidly.

Operation Mode of the Developed DMD Controller

The code written by us generates a series of 1-bit images, as required by the user. The type of images are selected by the user that can choose from are presented in table 4.2.

The user can choose some other important characteristics of the pattern that will be shown, such as:

- duration of exposure, How much time should an individual image be shown on the DMD. It must be less than 8s and greater than $100\mu s$.

- dark time between patterns

- the batch size of the communication

- if the pattern has to be repeated

- if the pattern should be reduced to the minimum image.

- if the images should be shown with a 45° inclination or a 90° inclination.

4.2.2 Synchronization with TCSPC board

A significant improvement from the previous system has been the synchronization between the DMD and the TCSPC board. This communication allows us to have a quick image exposure on the DMD, a rapid sequence of measurements, and a precise time interval for exposition.

The DMD was designed in order to have as output or as input a trigger signal. The board allows a trigger input to start recording a measurement. The trigger is an electrical signal to inform of the change in the pattern.

To achieve the synchronization, we have first made a cable that could connect the DMD to the board's serial port and then select the output voltage of the trigger via a jumper.

The trigger has as output a high voltage when there is a change in the pattern.

To have a very high measurement frequency, we need to operate in Continuous flow mode on the TCSPC board.[5] We are using a SPC -130 from the Becker-Hickl board that has two memories. In this modality, after completing a set of 32 measurements, the board quickly swaps the memory and the board, in a few tens of microseconds, is able again to store the new data.

4.2.3 Characteristic

The DMD operates in a pre-stored mode for precision of presentation of the images, high time reliability in the frequency change of pattern and speed of operation. The Images in this mode will have to be uploaded on the DMD before the start of measurement. Another possible mode of operation is video mode, where the pattern are uploaded on the fly. However, this mode is much less precise in the image shown and time exposition.

The dimension for the data sent to the DMD depends on the images to show. A factor that greatly influences the compression in the inclination of the image. If the image has a 0° angle or 90° angle, the dimension of the data per batch is around 7000 bytes if the same image has an angle of 45° the dimension of the data is approximately 40000 bytes, the enhanced run-length-encoding algorithm causes this difference [15] that it is used to compress the patterns. In table 4.3 we have highlighted the characteristics.

The maximum time allowed for a single element in pre-stored mode is 8 seconds. To reconstruct the Raman spectra from depth will require a very long time

parameter	value	notes
highest repetition per pattern	9523 Hz	
maximum time allowed for an image	8 s	
maximum number of patterns stored	256 pattern	
maximum pattern generatable by a PC	256 pattern	with a 8GB RAM
maximum pattern generatable by a PC	100 pattern	with a 4GB RAM
upload time to the DMD	5 s to 100 s	depends on th size of the pattern
Time to generate communication data on the computer	1s	

Table 4.3: Table of characteristics for the DMD.

integration for every base. We overcome this problem by looping on every base the number of times required. The looping through the basis also has the advantage of compensating the instability of the laser.

4.2.4 Design of the DMD mount

We designed a new mount for the DMD. There are 4 degrees of freedom (DoF). The high number of DoF has been chosen to have the system flexible for future upgrades.

The most critical parameter to be selected is the position in the z-direction. In this direction, we have the focus of the image of the fiber from L2, A precision of few tens of micrometer is required.

The second axis for importance to be set is the y axis. It is required to center the DMD on the central wavelength. It will become critical during the alignment process. a precision of the order of millimeters is required.

The third axis is the x-axis. The illumination has to be centered at the center of the DMD to maximize the spectral range. A precision of a few millimeters is required.

A final degree of freedom is the rotational axis of the DMD mirrors. It has been set to 45° because we want to keep the beam parallel to the optical table. The disadvantage of this choice is the limited spectral range and the increased computational time for compressing the basis.

A possible upgrade could be turning the DMD to 90° and have the optics (L3) and the detector at an angle. The optical system will become more complicated, but we will improve the spectral range and speed.
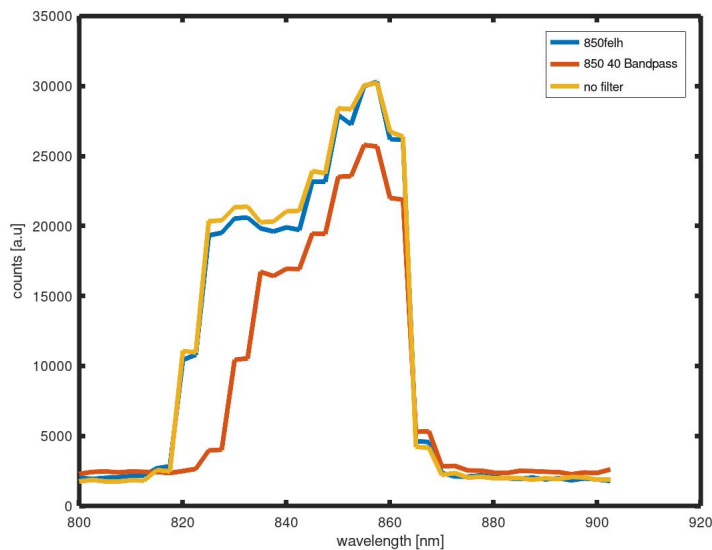
Figure 4.7: Counts of the spectrometer per wavelengths when centered at 850 nm. The variation of the counts are caused by the different intensity of the Supercontinoum laser at different wavelength.

4.3 System Characterisation

4.3.1 Spectral Range

Increasing the number of lines of the Grating will improve the resolution but will decrease the spectral range of the spectrometer. The spectral range will have to be chosen considering the Raman shift of the expected molecules to be searched and the system's absolute efficiency. If we want to probe higher wavenumbers, we will need to consider the low efficiency of the detector at 900+ nm.

During the alignment phase, we select the wavelength range of operation by selecting the grating angle. The spectral range is given by the illumination of the DMD, the alignment of the detector and the presence of a filter before L3. Using the calibration presented above, we find that the ideal spectral range on the DMD is 90 nm.

Not all the DMD areas can be illuminated because the light is being dispersed with an angle with respect to the DMD. If the DMD is too shifted on the x-axis, we are reducing the spectral range. Using the supercontinuum laser, it has been possible to vary the wavelength to verify the alignment of the system and measure the range using various filtering options inside the spectrometer where the filter was placed before L3 as explained in sec 4.1.2.

We the spectral range from fig. 4.7 is around 45 nm, meaning we are close to the ideal position of the DMD and detector with the minimum measurable wavelength to be around 820 nm and the maximum wavelength 865 nm. In particular, we notice that the efficiency and the range with the 800 felh filter are close to the one with no filter.

paramtere	measurement	source
h_{image}	294 μm	fig. 4.8
R	45 nm	4.3.1
h_{DMD}	7.1 mm	[20]

Table 4.4: Parameters to estimate the resolution of the spectrometer

4.3.2 Spectral Resolution

The spectral resolution is given by

- the number of lines on the Grating

- the number of bases to be used on the DMD

- the dimension of the input fiber

- the magnification factor of the optical system up to the DMD

- The resolution could be worsened by aberrations in the optical system

During the alignment process, it will be possible to measure the number of lines of the DMD illuminated and then convert them to the wavelength and find the spectral resolution. The lower the number of lines illuminated, the smaller is the resolution.

We can estimate the resolution of the system by using:

$$FWHM = \frac{h_{image}R}{h_{DMD}} \tag{4.4}$$

Where h_{image} is the image of the fiber dimension on the DMD plane, R is the spectral range of the spectrometer and h_{DMD} is the diagonal size of the DMD.

The measurement of the illuminated lines will happen during the alignment phase. The best estimate of the image dimension will happen when we reach the smallest possible sacnning line as done in fig. 4.8. Using eq. 4.4 and the parameters from table 4.4 we estimate the resolution of the system to be 1.9 nm.

To estimate the ideal number of basis to be used we need to find the number of lines illuminated.

$$lines_{image,fiber} = \frac{h_{image}}{h_{px}} = 41 \tag{4.5}$$

Therefore to achieve the optimal resolution we need to use:

$$n_{basis} = \frac{lines_{DMD}}{lines_{image,fiber}} = \frac{3000}{41} = 73 \tag{4.6}$$

The maximum resolution will be reached using a Hadamard set of 128 bases.

The resolution is limited by the dimension of the image of the fiber on the DMD plane. At the cost of the photon collection, we could use a smaller fiber. The fundamental limit of the spectrometer is the bandwidth of the Titanium Sapphire laser of 0.1 nm. Using eq. 4.4 we can estimate to reach this limit we would need to have a $h_{image} = 15\mu m$
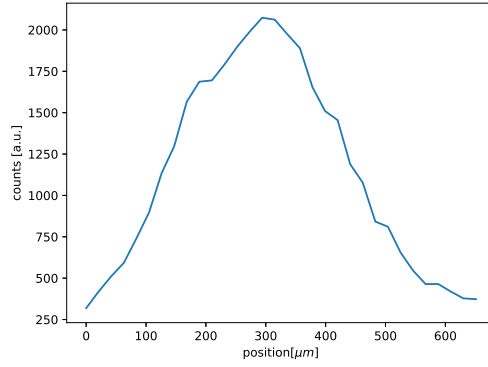
Figure 4.8: Illumination spot measured on the DMD with a raster scan of 3px line.

4.3.3 System Efficiency

The calculation of the absolute efficiency directly is complicated due to the saturability of the hybrid detector. We have tried to estimate the efficiency using a power meter

Absolute efficiency

Measurements taken at 670 nm, only focused light can be measured by the powermeter.

optical element	input power $[\mu W]$	output power $[\mu W]$
L1 + L2 + Aperture Slit	243	97
L1 + L2 + Aperture Slit +grating	97	56
complete setup	56	32

when no aperture slit is used

optical element	input power $[\mu W]$	output power $[\mu W]$
L1 + L2	265	190
L1 + L2 +grating	190	115
complete setup	115	65

the estimated efficiency of each component at 670 nm is

optical element	efficiency $[\%]$
L1 + L2	72
Aperture Slit	56
grating	58
complete setup with Aperture	13
complete setup with no Aperture	24

at 820 nm, we have measured:

optical element	input power [μW]	output power [μW]
L1 + L2	600	230
L1 + L2 +grating	605	120
complete setup	120	53

optical element	efficiency [%]
L1 + L2	38
grating	52
complete setup with no Aperture	8

We have a higher loss on the lenses with the same alignment of the 670 nm. The system has lower efficiency than in the 670 nm case due to the high losses of the lenses. Finally, we should consider that the efficiency of the detector is at 20% below 850 nm. The absolute efficiency will be around 2% in the region below 850 nm.

4.3.4   Best choice of probing wavelength

As we previously discussed, it is possible to choose the laser's operational wavelength and, therefore, the wavelength with optimal characteristics.
when choosing the working wavelength we need to take into account:

1. the efficiency of the spectrometer, in particular the efficiency of the hybrid detector.

2. the availability of filters

3. power of the laser

4. Raman efficiency $\propto \frac{1}{\lambda^4}$. but it is nearly constant for all wavelengths in fact considering the boundaries of our operational wavelength $(\frac{1000nm}{700nm})^4 \approx 4$

5. Fluorescence of the sample that decreases with the wavelength

For this work, the 780 - 785 nm wavelength was used as it was in a position of high power and stability for the laser, being very common as a Raman probing wavelength several filters were available such as the 785-33 nm notch filter (2) and, the fluorescence of the sample was relatively low (5).

A problem for this probing wavelength was the spectral range as we wanted to probe the region of 2500 cm^{-1} typical of lipids. It corresponds to 980 nm where our detector has an efficiency of 10^{-4} in comparison before 850 nm, the hybrid detector has an efficiency of 10^{-1}

A different choice that had not been used due to problems with the laser is the 720 nm where the 2500 cm^{-1} region would fall in 880 nm where the efficiency is 10^{-2}.

4.3.5 Temporal Resolution

The temporal resolution will give information on the delay of the arrival of a pulse and it FWHM. Those characteristics in turn, will give the information on the distance from the collection to the element being identified.

We can measure the IRF by connecting the laser source directly to the spectrometer and we measured $FWHM_{IRF}$ to be 200 ps.

The hybrid detector has a slow response of more than 100 ps. This means that we will not be able to measure IRF with smaller FWHM because:

$$FWHM_{spect}^2 = IRF_{det}^2 + FWHM_{pulse}^2 \tag{4.7}$$

4.4 The alignment

Aligning the optical element is a difficult process that must be done carefully to minimize the aberration and obtain the best possible resolution and photon collection. We will first present the spectrometer alignment process and its characterization using a beam profiler. We will compare the performance to the spectrometer presented in chapter 3 that during the alignment will be taken as reference. We will finally explain the noise term of the spectrometer and our solution for the minimization.

4.4.1 The alignment process

It is a process that has to be done by steps with the help of a beam profiler and has to be fine-tuned before any measurement.

For these three initial steps, any laser can be used, and therefore the best results will be obtained with a visible safe laser.

- The beam exiting the fiber will be diverging and on the grating, we need to have a collimated source for optimal efficiency. We could decide following what has been stated in section 4.6 that we want to be slightly out of focus. This condition will be difficult to set precisely.

- We need to center the grating on the beam and have the light reflected from the grating be parallel to the optical table by changing the inclination of the grating. There are multiple modes of dispersion, we will need to select the strongest.

- We need to place L2 with the curved side facing the incoming beam. This is the most critical component to place as it is the element that will cause most of the aberrations.

As a first step, we need to minimize the aberrations at the alignment wavelength. After optimizing using the visible wavelength, we will need to change the wavelength and align using the expected wavelength for the Raman shift. We will need a light source with very short spectral band and therefore, we will use the Titanium Saphire

laser tuning it at the Raman wavelength. The operational wavelength is not the probing wavelength but the wavelength where we expect the Raman signal.

A beam profiler is then needed because it has much higher precision and will detect all the aberrations. The Beam profiler is formed by a CCD camera used to represent the pulse spatial shape.

- By changing the grating angle we need to center the new wavelength on L2

- By looking at the image, we need to minimize the aberrations. Small adjustments will have to be made by moving a few millimeters L2 or adjusting the angle with two angle stages.

- After removing every aberration, we can place the DMD and center it on the mirror area. Using the x,z-axis stage, we can place the DMD at the correct position.

- We turn all the DMD mirrors to the detector.

- we place L3 and it will have to be centered on the lens. It is not possible to move L3 closer due to the presence of L2. We will have to place the DMD at a slight angle, because the reflecting angle of 12.5° is too small to reach L3. If the centering condition is not met firstly, we will lose in efficiency due to aberration because not all photons will be able to reach the active area of the DMD and more importantly, the photon that reaches the active area depends on the number of lines activated on the DMD, even if not illuminated. This is probably caused by some small change in the reflection angle on mirrors of the DMD.

- We can verify the alignment on the detector plane using the beam profiler. Here we can have some aberrations, but most have to be removed for the issues listed above.

- Finally, we can place the detector and it will have to be placed perpendicularly to the beam. The active area diagonal will have to be perpendicular to the optical table.

After this operation, the lenses are aligned and only the DMD and detector are to be aligned. This small realignment process has to be done before any series of measurements to avoid loss of efficiency

alignment of DMD, Detector and fiber

We have now to proceed with the fine-tuning using the TCSPC board. This procedure has to be also performed before measurements. Firstly we need to align the DMD on the z-axis to focus L2 on the DMD plane. By using the Ti-Sa laser in pulse mode, we use the raster scan and by moving on the z-axis, minimize the number of lines that are illuminated

- We will need to select raster scan firstly with large lines

- minimizes the lines illuminated by moving the z-axis

- minimize the spot by rotating the linear input fiber

- reduce the dimension of the line and repeat until the dimension of the spatial FWHM is of the order of 200 μm

To estimate the spatial FWHM that I define as d_f we take

$$d_f = n_{lines}d_{px} \tag{4.8}$$

where $d_{px} = 7$ μm is the dimension of a single pixel.

Then we will have to optimize the positioning of the hybrid detector using the XYZ stage. This will be achieved by maximizing the photon count. Due to the large area of the detector, we will reach a plateau in the counts we will need to position the detector at the center of this plateau. The DMD will have to be placed carefully in the x-direction as not to cut any wavelength. The detector will have to be placed such that that the image of the DMD falls entirely on the Active area.

After having aligned the setup it is needed to calibrate the spectrometer.

Calibration process

We will be measuring the light arriving from a determined line on the DMD and on the z-axis the grating will disperse the wavelength. That means that each line will have a corresponding wavelength.

We need to find a function $\lambda(line)$.

We will use the supercontinuum laser and change the wavelength and measure the spectrograph. The supercontinuum laser has been chosen due to the simplicity of changing the wavelength compared to the Titanium sapphire laser.

We will do linear regression and find the relative wavelength line by measuring the highest peak position for each wavelength.

Once we obtain the relation for each wavelength, we can convert to wavenumber by knowing the probing wavelength.

4.4.2 Characterization of the image on the DMD and detector

The critical element of the resolution is the image on the DMD. A larger image will correspond to a worse resolution of the setup. Using a beam profiler, we can understand the change when the DMD is placed at an angle by looking at the spot size.

We see in fig. 4.9 as we start moving from the aligned wavelength, the aberration increases, worsening the resolution. From fig. 4.9a taken using a beam-profiler positioned on the DMD plane, the image of the fiber has a width dimension of 2.2 mm and height of 0.28 mm. This image is larger than the dimension of the fiber. It is caused by the not collimation of the L1 lens as seen in 4.1.2. Once we move out of the wavelength Region of alignment and exit the beam profiler, we see that there are significant aberrations like in 4.9d. It is the main reason for the use of a secondary filter in front of the L3 lenses.

(a) 850 nm, calibration wavelength

(b) 830 nm

(c) 810 nm

(d) 780 nm. Higher power of injection
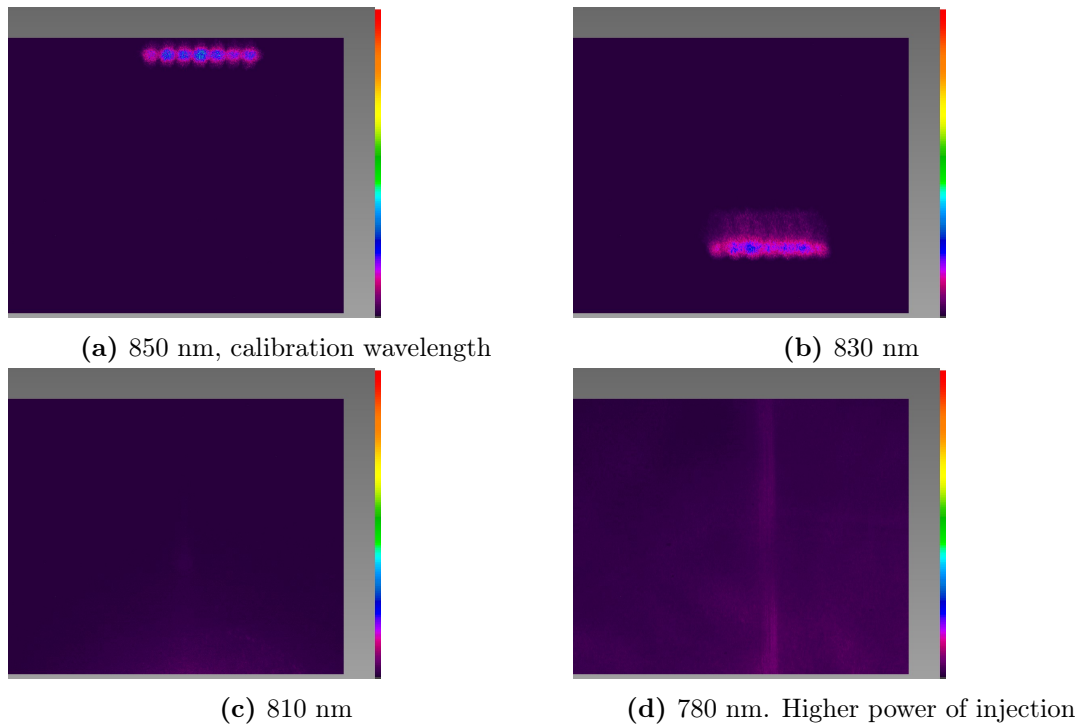
Figure 4.9: Beam-profiler measurements of different wavelengths

Figure 4.10: Beam image on the detector side.

The image on the detector's side seen in fig. 4.10 is not critical that the image be entirely out of aberrations, but they cannot be too strong to avoid any loss of photons. Its dimensions are in width 0.98 mm and in height 0.16 mm and are half of the dimension on the DMD because of the Magnification factor of L3 of 0.5.

4.4.3   Comparison between TDDRS and WTTS

The Wavelength through time spectrometer and the time domain Raman spectrometer separates the wavelengths in two different methods, but we can use it to verify the correct alignment and the presence of the Raman signal, as a standard spectrometer

As we showed, the efficiency of the time domain diffuse Raman spectrometer is 2 %. instead, the efficiency of the wavelength through time spectrometer is 80%.

The fiber used has a major importance, for the wavelength through time we use

a monomode fiber with 4 μm of diameter and for the TDDRS a 7×200 μm fibers.

We need to take the ratio to compare the photon collection efficiency of the two methods.

$$\frac{\eta_{TDDRS}}{\eta_{wtt}} = \frac{\eta_{spectrometer,TDDRS}}{\eta_{spectrometer,wtt}} \frac{A_{fiber,TDDRS}}{A_{fiber,wtt}} = \frac{0.02}{0.8}7(\frac{200}{4})^2 = 400 \qquad (4.9)$$

In TDDRS, we are approximately collecting 400 times the photons than in the WTT.

This estimation can be used to determine the correct alignment of the setup by looking at the integral of the photon counts.

4.4.4   App

An Android application called "Raman Shift calculator" was developed to help the user understand the Raman shift in wavelength given the pump laser and the shift in wavenumber. The application is available on the Google Play store. This shift is not immediate to calculate by a person and therefore, a simple program can speed the conversion. It can be helpful during the alignment process to understand the required wavelength for optimizing the spectrometer.

Three other modes are available. The first converts into wavenumber from a probing wavelength and a Raman wavelength. The second given the wavenumber and the Raman wavelength tells the required probing wavelength, it is useful for us because the laser is tunable. The third mode gives the relative efficiency from the initial wavelength to the final wavelength following $\eta = (\frac{\lambda_f}{\lambda_i})^4$

4.4.5   Noise

To reduce the noise around the detection probe, a covering box was built to avoid the stray light coming from monitors, mobile phones, laser reflections or any other source that would increase the noise of the measurements.

Secondly, the detector was covered to prevent this noise, not allowing any light other than the one coming from the desired optical path. On the optical path, a second filter can be added. It will remove all the elastic light leaking from the first band.

We are more resistant to noise coming from any sample fluorescence than a CCD camera or the WTT method because the fluorescence in the two cases is divided on the number of channels of the spectrometer (number of pixels on the CCD, number of time gates in WTT). In this case, it will be divided on both time gates of the WTT and pixels of the DMD. The fluorescence will be divided on the total number of elements, $tot_{el} = N_{basis}N_{timegates}$

A further noise term can be caused by the reflection of the elastically scattered light on the optical table from the removed modes of the gratings, lights from the DMD or any other external source.

Covering the spectrometer

The hybrid detector has few dark counts per second, on the order of 300, but if we do not adequately isolate it from the light present in the room caused by the
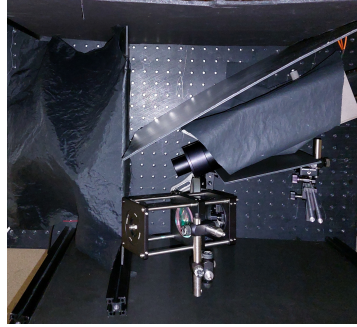
Figure 4.11: Picture of the inside of the spectrometer with the covering.

presence of computer monitors, laser or dim lights, it appears that the background counts are much higher, enough to saturate the detector. Moreover, inside the spectrometer, there are two additional noise sources. Firstly, on the electronic board of the DMD, some LED are present and secondly, the grating is dispersing the wavelengths on multiple modes that are not guided by the optical path. We needed, therefore to shield this detector from any lights. Placing some PVC board on the sides of the spectrometer, we provide some initial protection from the sides. We have placed a piece of PVC on the DMD side, leaving a rectangular cut inside it for the mirror area. The final setup is shown in fig. 4.11.

Inside the spectrometer we have the DMD with some LED lights on its board. The DMD mount partially blocks the light but if not properly covered they are a significant source of background. We used a piece of cloth to cover them. Cloth has been used instead of PVC or cardboard because it adapts easily to the surfaces and better blocks those light.

The detector itself has to be protected. The light source that we want to detect passes through the DMD. Any exposed side has to be covered as still some external light could be detected, but it should be mostly protected from any reflection inside the spectrometer. A possible source of noise is the elastic light collected by the fiber that is either reflected on the optical table or metallic stands of the optical components.

To be certain that no external light enters the detection system a Large Cloth covers the entire setup so that any left gap is closed. The entire spectrometer is enclosed by some PVC boars and another large cloth.
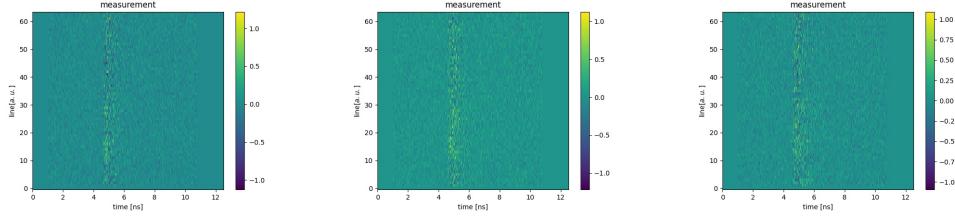
4.5   Data Analysis

The data measurement has to be analyzed to accumulate the various measurement loop or perform the inverse transformation from the Hadamard Basis to the wavelength base.

The equation that has to be minimized is:

$$L(\mathbf{S}_\nu) = ||\mathbf{S}_H - \mathbf{H}\mathbf{S}_\nu||_2 + L_{reg}(\mathbf{S}_\nu) \tag{4.10}$$

and the loss function has to be minimized. The basic method uses a least square minimization where $L_{reg}(\mathbf{S}_\nu) = 0$.

Figure 4.12: Three different acquisitions. Each one has a very low photon count of Silicone ($\mu_a = 0.05$, $\mu_s = 5$) thickness = 10 mm, $\rho = 0$ mm over marble

If instead we want to perform some regularization technique we can also use as an additional loss term

- Lasso regression where $L_{reg}(\mathbf{S}_\nu) = \lambda||\mathbf{S}_\nu||_1$ where the regularization forces the final vector to be sparse.

- Ridge regression $L_{reg}(\mathbf{S}_\nu) = \lambda||\mathbf{S}_\nu||_2$

For the regression function, we have used a python library called sklearn.
We then had to plot the data with the correct wavelength and wavenumber axis.

4.5.1 Chosing the regularization method

We present the results of the reconstruction with the various methods.

We can see in particular from table 4.5 that the Ridge regression does not perform well in the regularization task, being equal for the noise to the simple least-square optimization but losing the amplitude information. When choosing the correct α, the Lasso regularization technique reduced the noise and left unchanged the photon amplitude of the Raman signal. Lasso performs well in this case because it is a sparse signal. Some artifacts can be seen in the reconstruction of a measurement taken by looking at the amplitude color scale where we see negative counts. Those are unphysical and are caused by the Poisson noise of the signal to be reconstructed.

4.5.2 Notes on the reconstruction

When reconstructing a weak signal, we need to integrate for a long time interval. To perform a long measurement, we need to measure a repeated loop of the Hadamard basis and then either sum them together or solve an over-determined system during the reconstruction. In fig. 4.12 we see the reconstruction of a short acquisition time.

Then due to the short acquisition time, we will have a very high background counts comparable to the Raman signal.

Due to how the bases are constructed, the first line is always open. The reconstruction interprets this line as the source of most of the background noise, as seen in fig. 4.13. We will have to remove the first line. This first line has much more counts than the other lines and this has to be considered noise. Therefore we will remove this line

α	LSMR	LASSO	RIDGE
0			
0.1			
1			
10			
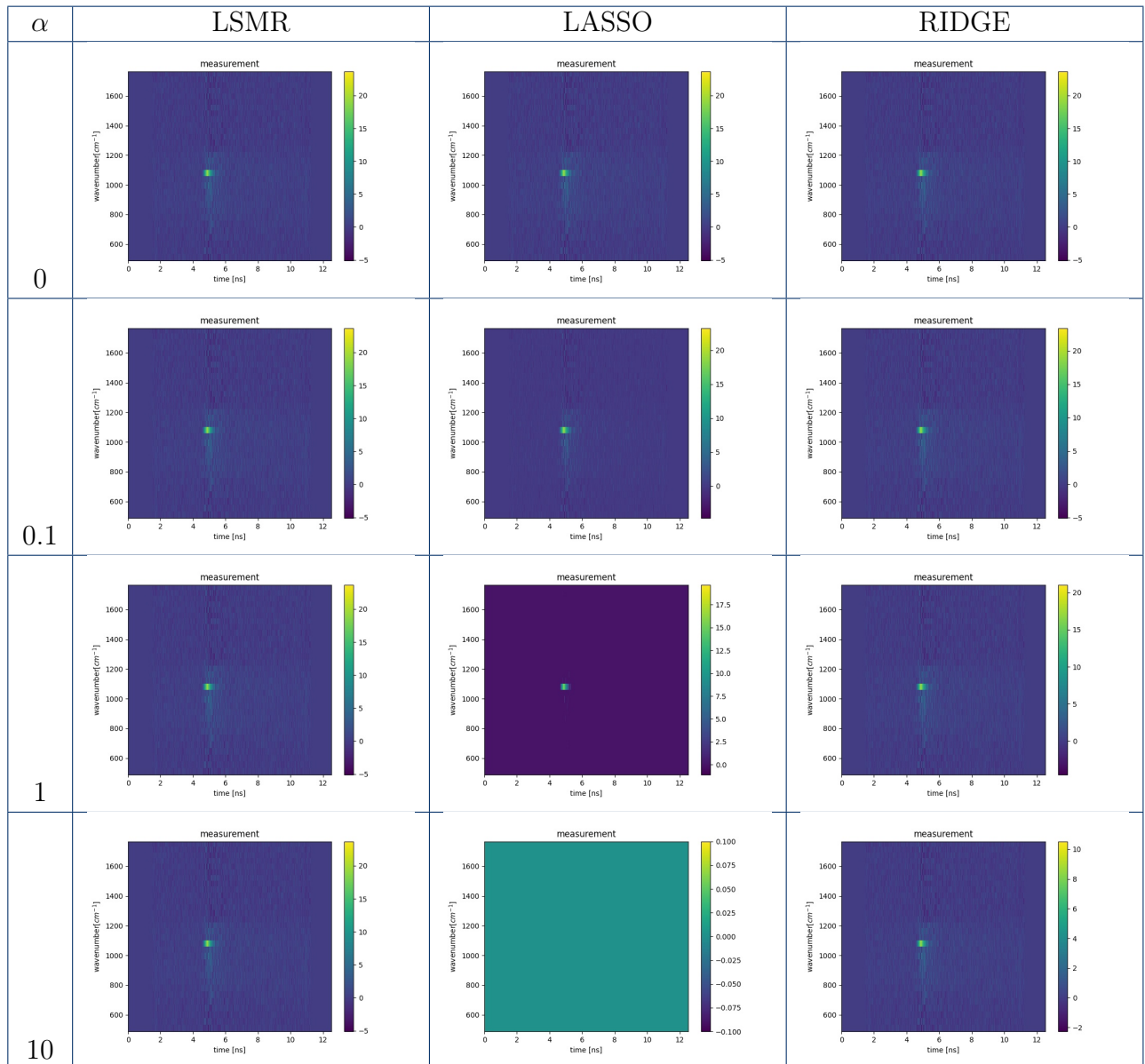
Table 4.5: Different regularization methods, Measurement performed on Marble Hadamard scan, 1s per base, 32 bases $\rho = 0$, Note that the LSMR method is independent to the α term chosen.
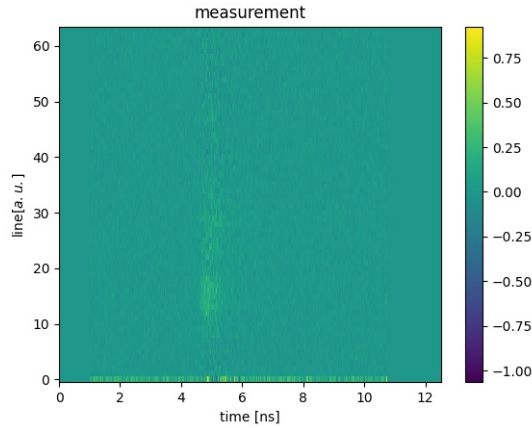
Figure 4.13: Reconstructed spectra with the first line

4.5.3 Choice of plot

Three types of plots can be used. We have three parameters that we need to present:

- the photon count

- the wavelength

- the time scale

We are limited in 2D to show the image and in fig. 4.11 we represented different types of plot.

The most complete plot is colormesh, where we have on one axis the wavelength and on a second the time axis and the photon counts are represented by the color intensity. This method's advantage is that it represents all three elements, but it does not offer an immediate way to read the wavelength, like in a typical spectrometer, and time axis, like in diffuse optics.

To have the perfect picture for all three elements, we have to use two other plots.

Plotting only some selected time gate, or the integral, will represent the data like a spectrometer but lose the temporal distribution. It can be useful to determine the Raman shift. Working with 4096 time-gates few can be shown at a time. We can plot some wavelengths with respect to time. It is the best way to read the time axis and have the information on the distance of the sample being analyzed. We will lose the remaining information on the wavelength.

(a) pmesh example

(b) Integration on all time gates

(c) Only selected time gates are presented

(d) Showing only selected wavenumber
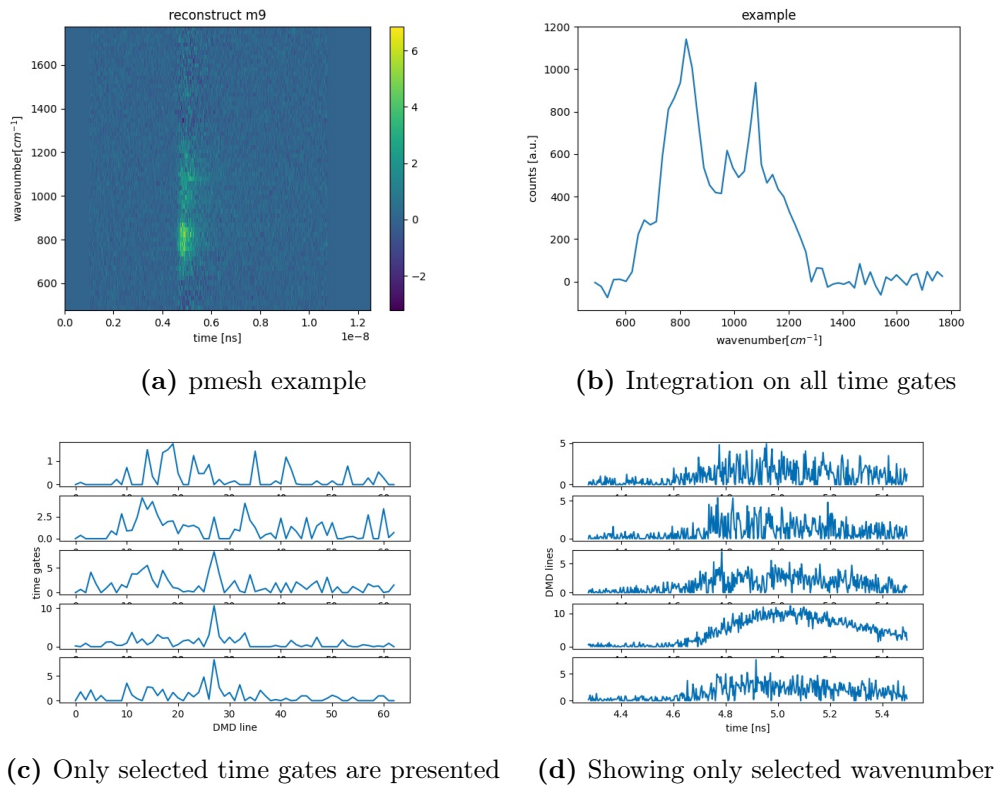
Figure 4.14: Different types of plot.

4.6   Time-Domain Diffuse Raman Measurements

Diffuse Raman spectroscopy aims to recognize a material at depth by looking at its Raman fingerprint. The last chapter discussed the design and working principle of such a spectrometer. Now we will present measurements of the Raman light. Here we present the measured Raman spectra on some diffusive samples. Marble and silicone-based samples are ideal for this as both of them are highly diffusive and strong Raman emitters. Moreover, both these materials have Raman fingerprints in regions similar to in-vivo tissue types (Bone and Lipids, respectively). Thus, these two sample types will be the primary focus of this chapter.

We will then present several measurements performed on bi-layer samples and present the diffuse Raman capabilities of this spectrometer. We will finally present some in-vivo measurements.

4.6.1   Raman measurements in reflectance of homogeneous samples

We firstly have to present the result for homogeneous samples. In the single-layer case in reflectance geometry, we are not limited by the photon count. The photon count is high because we are collecting at a small source collection distance.

(a) DMD line position **(b)** Convertion to wavelength **(c)** Convertion to wavenumber
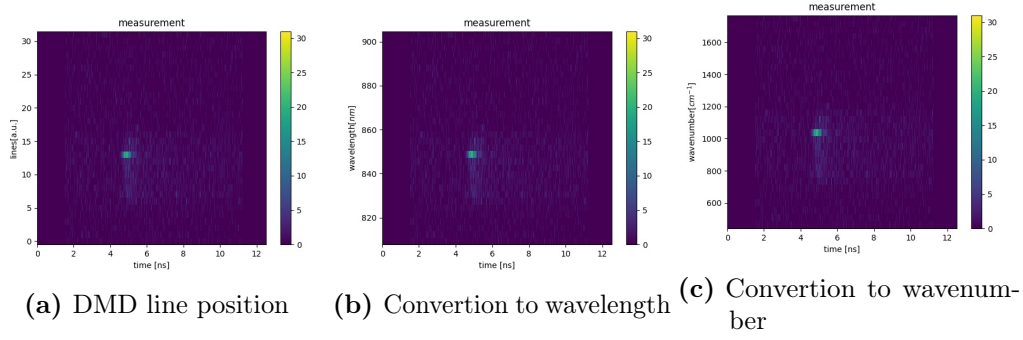
Figure 4.15: Marble, Raster scan, 1s per line, 32 lines. Laser power 40 mW, 780 nm wavelength

(a) Raw measurement **(b)** Line scan reconstruction
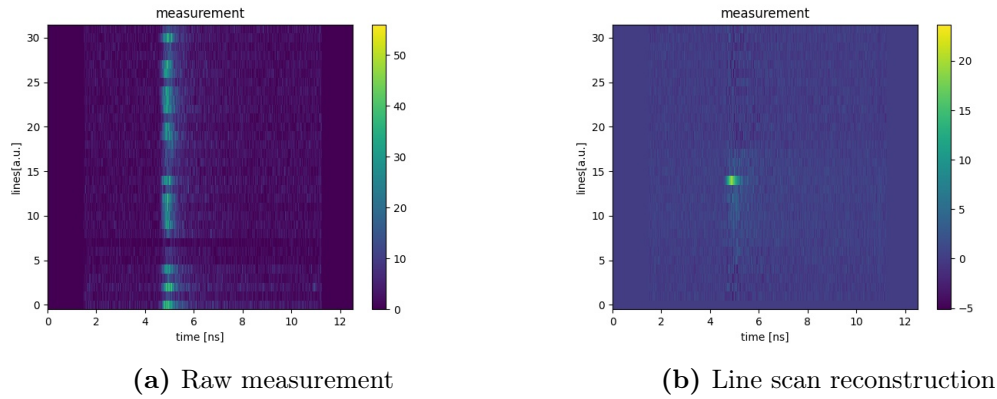
Figure 4.16: Marble, 1s per base, 32 bases $\rho = 0$

Marble

Marble is a very strong Raman emitter and here we present the measurements performed in a single layer material formed by marble block.

Raster Scan

Reconstructing the measurement with a raster scan is trivial as a single line corresponds to a single wavelength range. In fig. 4.15a we have the line position of the DMD, using the calibration we can convert into wavelength in fig. 4.15b and then into wavenumber in fig. 4.15c.

Hadamard Scan

Differently the reconstruction in a Hadamard scan is not trivial. From the raw measurement, we are not able to understand the spectral distribution. Using the methods presented in section 4.5 from the raw measurement presented in fig. 4.16a we can reconstruct the line scan 4.16b and similarly to what has been done to the raster case, we can convert the DMD lines to wavelengths and wavenumbers.

After presenting the data in a colormesh plot we can focus the spectrograph

(a) Spectra of Marble

(b) Plot of different DMD lines
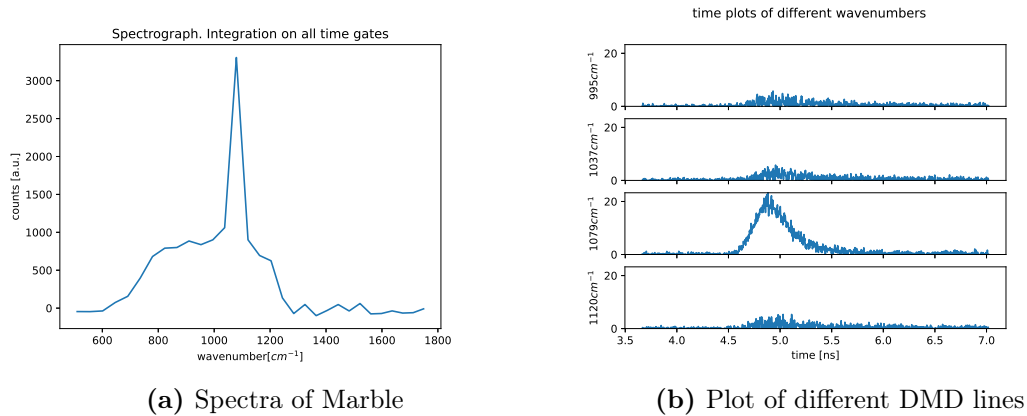
Figure 4.17: Marble, 1s per base, 32 bases $\rho = 0$
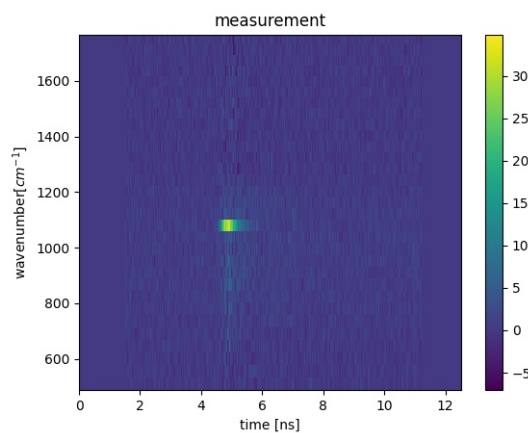
Figure 4.18: Marble. Hadamard scan, 1s per base, 32 bases lsmr, $\rho = 10$ mm

for marble presented in fig. 4.17a that shows the 1086 cm^{-1} peak. In fig. 4.17b we show the different time-domain plots for the different reconstructed DMD lines, and therefore for different wavenumbers.

Increasing the source detection distance

To increase the source detection distance (SD) we make use of ring illumination using an axicon. We will refer to the source detection distance as ρ. Increasing the source collection distance improves the signal-to-noise ratio of the photons coming from the depth. It comes at the cost of reduced photon counts and a broadening of the temporal FWHM. In fig. 4.18 we have the measurement with a 10 mm SD separation and comparing in fig. 4.19 the time distribution of a Raman signal to a measurement with $\rho = 0$ we can see that the it has a broader temporal distribution, this is cause by the added travel time inside the material as seen in chapter 2.

Silicone
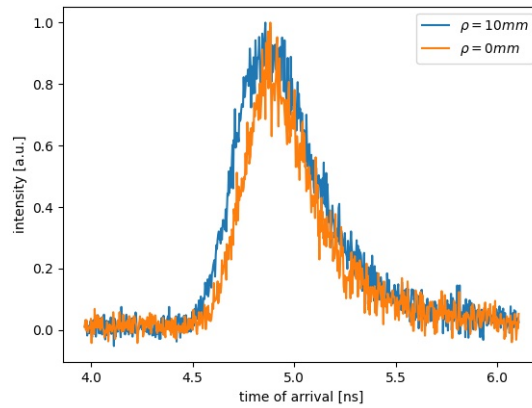
**Figure 4.19:** Comparison of different collection source distance normalized
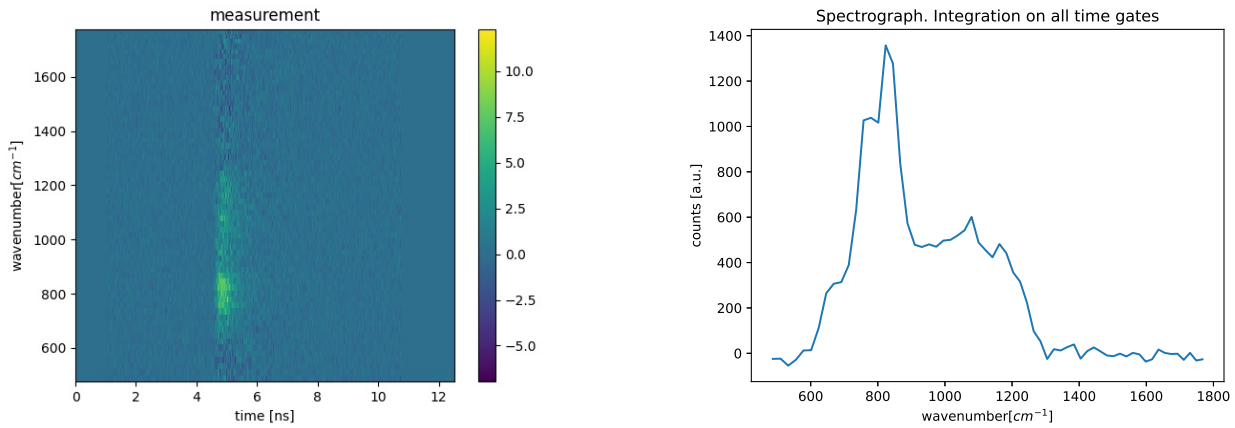
Figure 4.20: Silicone ($\mu_a = 0.05\ cm^{-1}$, $\mu_s = 15\ cm^{-1}$). thickness = 5 mm, $\rho = 20$ mm Hadamard scan, 64 basis, 1s per bases, repetition 20 times, total integration time 1280s, $\rho = 0$ mm

In fig. 4.20 we can see the spectrum we measured of a silicone phantom. In particular we noticed a peak at 800 cm^{-1}. Considering the long integration time of 1280 s we can conclude that this is a Raman shift with a low cross section. The main Raman shift for Silicone is at 2500 cm^{-1} and is out of the range for the spectrometer.

4.6.2   Bilayer

The bilayer measurements were performed using a Silicone phantom over a block of marble as seen in fig. 4.21. The Silicone phantom had a known coefficient of scattering and absorption and three possible thicknesses, 0.5 cm, 1 cm, 3 cm.
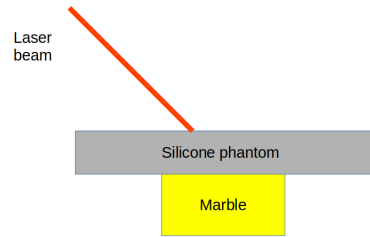
Figure 4.21: Example of Bilayer measurement
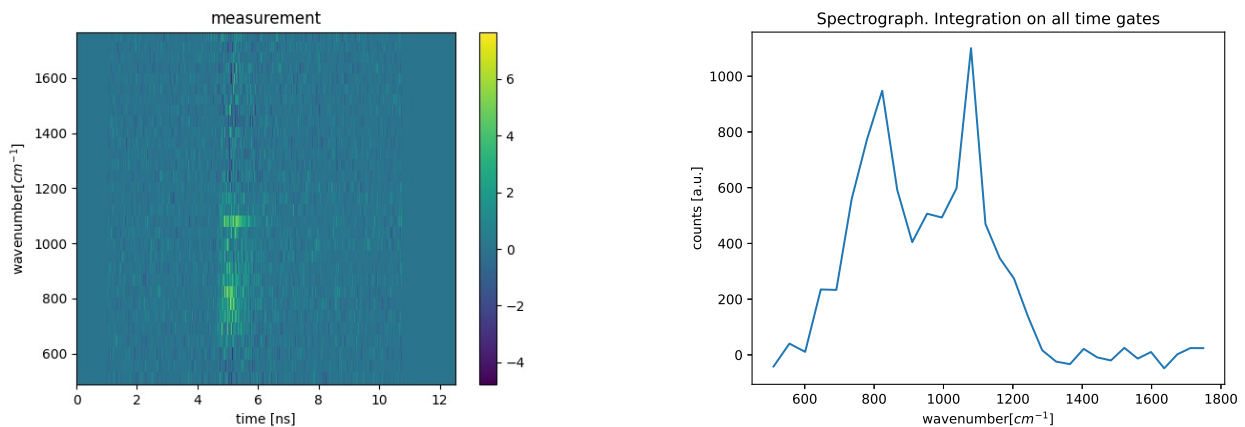
Figure 4.22: Silicone ($\mu_a = 0.05\ cm^{-1}$, $\mu_s = 15\ cm^{-1}$) thickness = 5 mm top layer, Marble bottom layer, $\rho = 20$ mm

Measurements

We want now to measure the spectra from bi-layer samples made of silicone on the top layer and marble on the bottom layer. Multiple silicone phantoms were available with different scattering and absorption coefficient.

Silicone ($\mu_a = 0.05\ cm^{-1}$, $\mu_s = 15\ cm^{-1}$) + Marble

From fig. 4.22 we can see that we can recognize the 1086 cm^{-1} shift from the marble with a SD distance of 20 mm and a thickness of 5 mm of the silicone and the 823 cm^{-1} from the silicone. in particular, focusing on two wavenumbers in fig. 4.23 we can recognize a tiny time shift between the two curves. In fig. 4.24 we increased the silicone's thickness to 10 mm and the Raman intensity was drastically reduced. By reducing the SD distance to be null, we observed an increase in the photon counts of the Raman signal from both the silicone and marble in fig. 4.26 where the silicone thickness was 5 mm but in fig. 4.24 with a silicone thickness of 10 mm we again are not able to measure the Raman from marble.
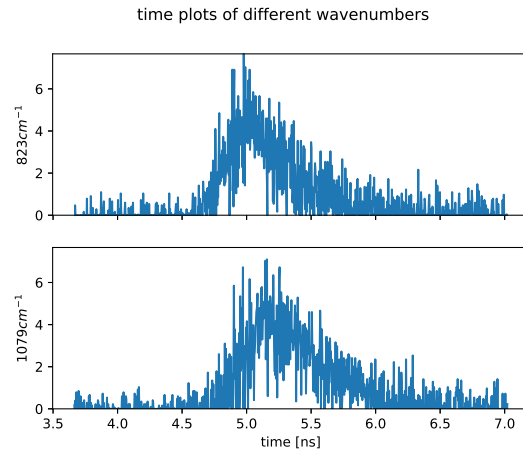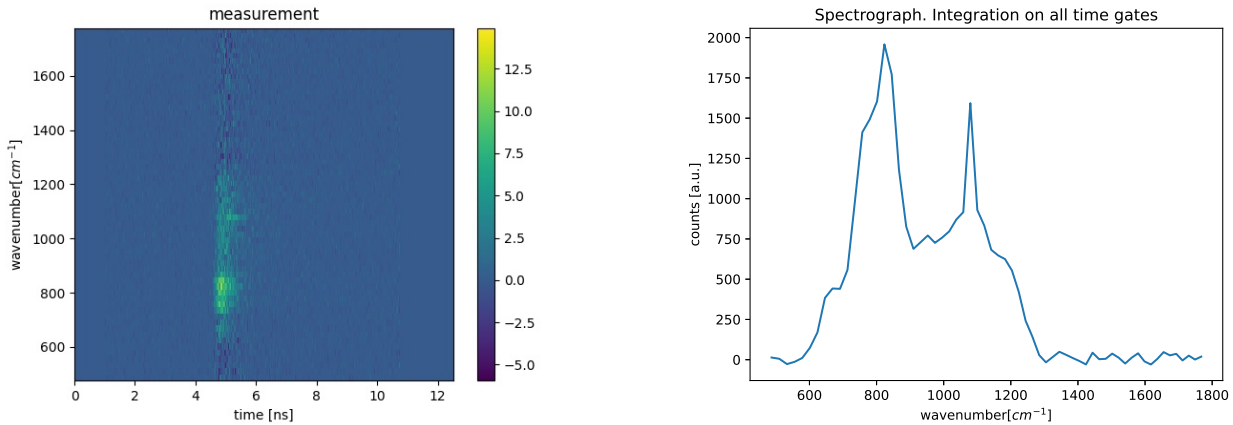
Figure 4.23: Silicone ($\mu_a = 0.05\ cm^{-1}$, $\mu_s = 15\ cm^{-1}$) thickness = 5 mm top layer, Marble bottom layer, $\rho = 20$ mm. Time of arrival for the wavelengths with a shift of 823 cm^{-1} and 1079 cm^{-1}.
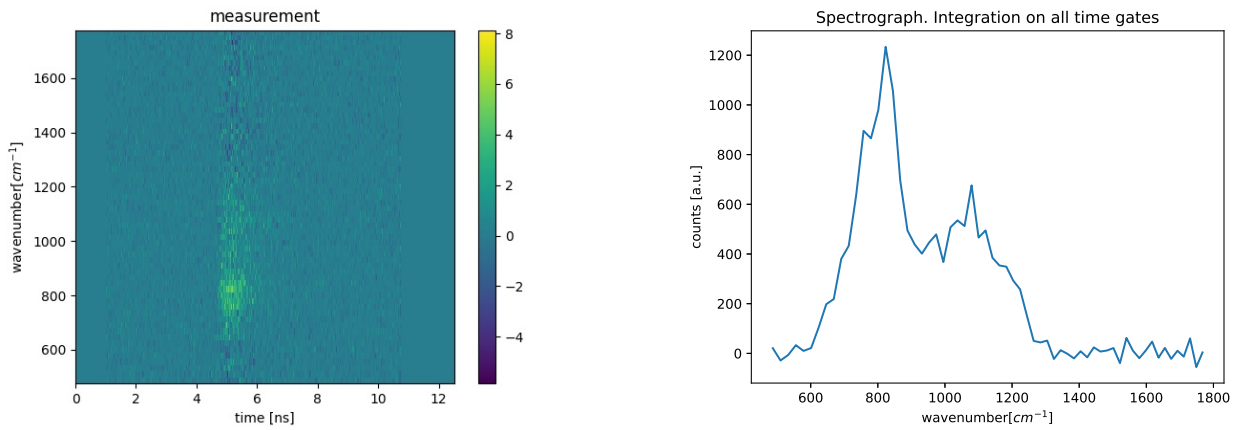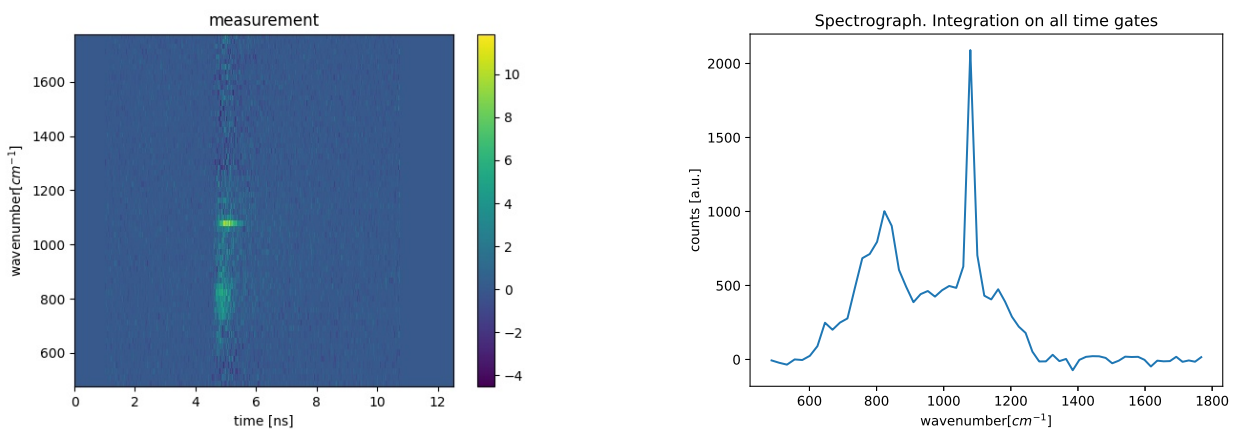

Figure 4.24: Silicone ($\mu_a = 0.05\ cm^{-1}$, $\mu_s = 15\ cm^{-1}$) thickness = 10 mm top layer, Marble bottom layer, $\rho = 20$ mm
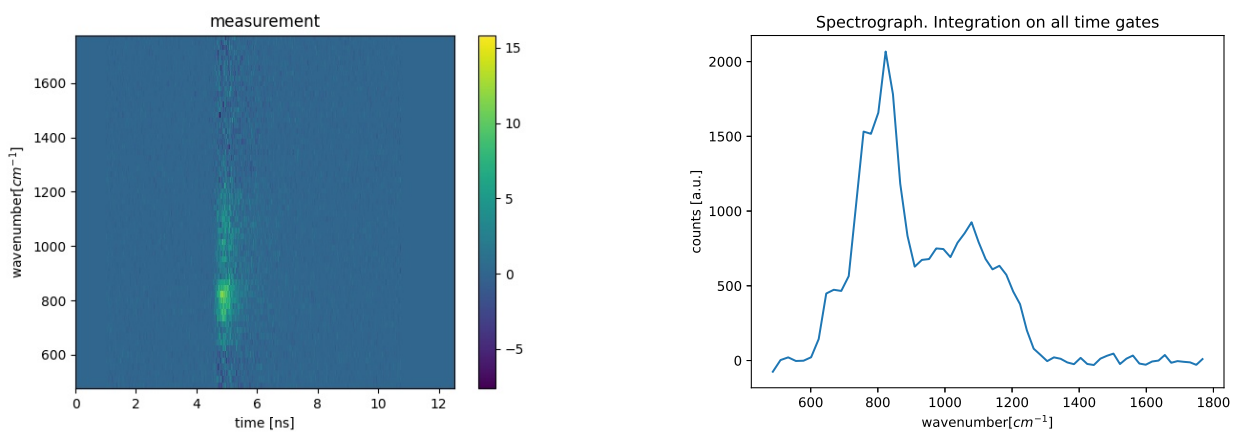
Figure 4.25: Silicone ($\mu_a = 0.05\ cm^{-1}$, $\mu_s = 15\ cm^{-1}$) thickness = 10 mm top layer, Marble bottom layer. $\rho = 0$ mm

Figure 4.26: Silicone ($\mu_a = 0.05\ cm^{-1}$, $\mu_s = 15\ cm^{-1}$) thickness = 5 mm top layer, Marble bottom layer. $\rho = 0$ mm

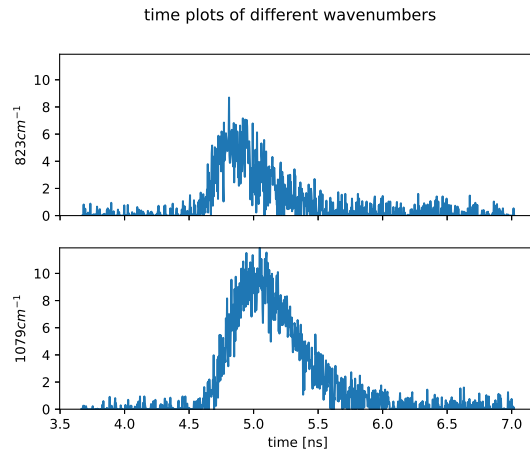**Figure 4.27:** Silicone ($\mu_a = 0.05\ cm^{-1}$, $\mu_s = 5\ cm^{-1}$) thickness = 5 mm top layer, Marble bottom layer, $\rho = 0$ mm

Silicone ($\mu_a = 0.05\ cm^{-1}$, $\mu_s = 5\ cm^{-1}$) + Marble

We changed the material of the silicone phantom to a less scattering one and we observed that from fig. 4.27 we can measure the Raman from marble after a 5 mm thickness and in fig. 4.29 after a thickness of 10 mm. We can see that the Silicone's Raman signal has a much lower intensity than the one from the previous phantom. This is because the light has a lower scattering coefficient the light there are fewer scattering events and less inelastic scattering.

Once we focus on the time domain and look at the 1089 cm^{-1} and 823 cm^{-1} shift, we see that from fig. 4.28 the there is a significant time separation of the two Raman peaks. In fig. 4.30 we can also measure a small curve for the 1079 cm^{-1} shift. In section 4.6.2 we will analyze the time separation of the Raman signals from marble and silicone from measures presented in fig. 4.27.
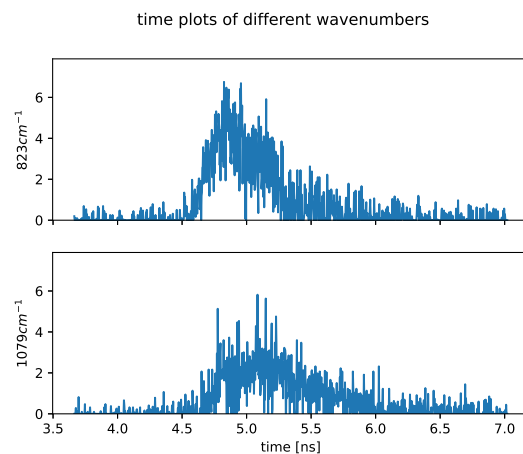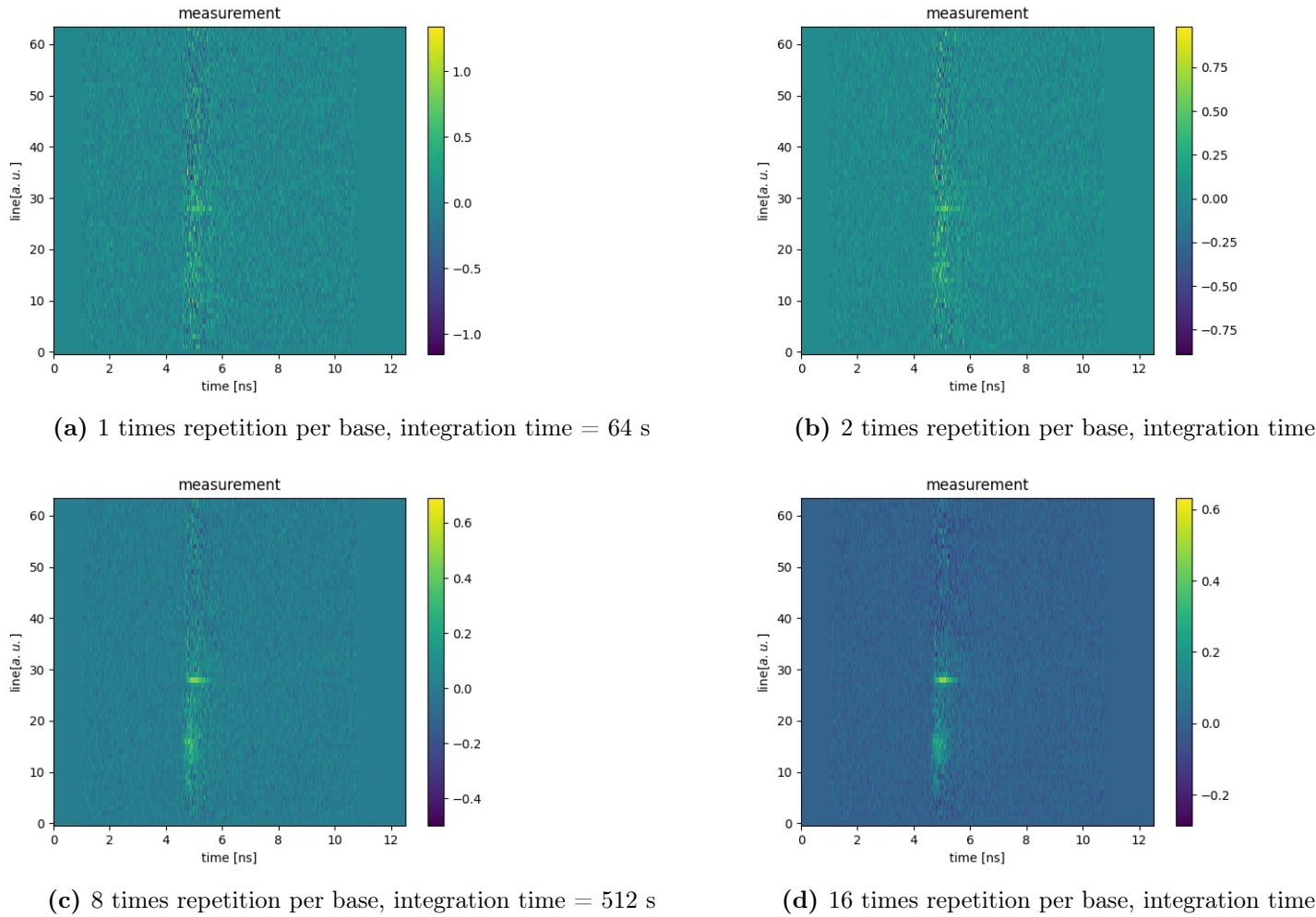
Integration time

Figure 4.28: Silicone ($\mu_a = 0.05\ cm^{-1}$, $\mu_s = 5\ cm^{-1}$) thickness $= 5$ mm top layer, Marble bottom layer, $\rho = 0$ mm. Time of arrival for the wavelengths with a shift of $823\ cm^{-1}$ and $1079\ cm^{-1}$.
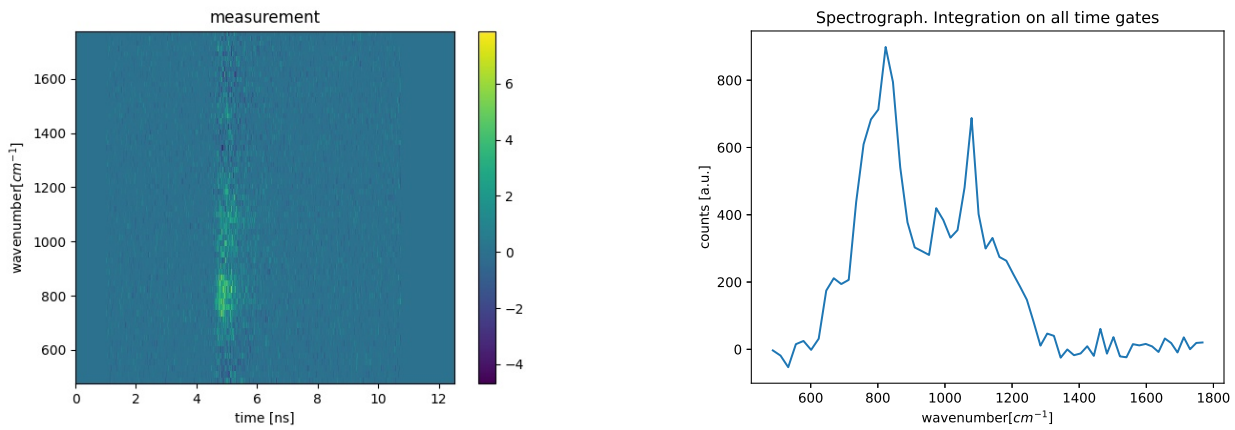
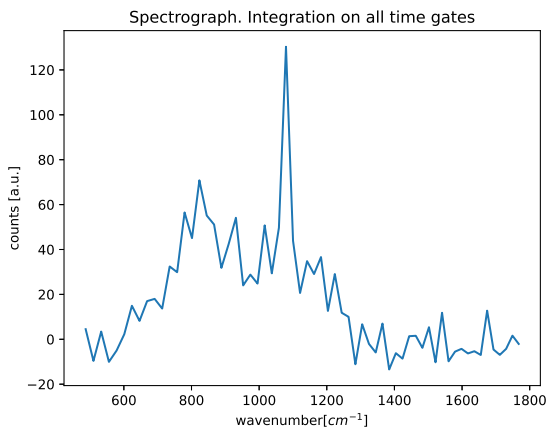**Figure 4.29:** Silicone ($\mu_a = 0.05\ cm^{-1}$, $\mu_s = 5\ cm^{-1}$) thickness $= 10$ mm top layer, Marble bottom layer, $\rho = 0$ mm

Figure 4.30: Silicone ($\mu_a = 0.05\ cm^{-1}$, $\mu_s = 5\ cm^{-1}$) thickness $= 10$ mm top layer, Marble bottom layer, $\rho = 0$ mm. Time of arrival for the wavelengths with a shift of $823\ cm^{-1}$ and $1079\ cm^{-1}$.

(a) 1 times repetition per base, integration time = 64 s

(b) 2 times repetition per base, integration time

(c) 8 times repetition per base, integration time = 512 s
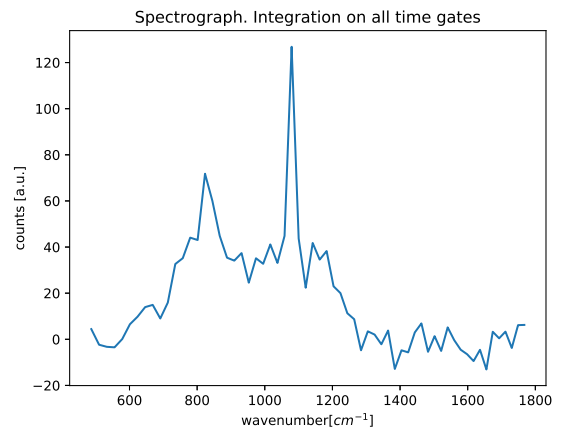

(d) 16 times repetition per base, integration time

Figure 4.31: Bilayer reconstruction of different integration time. Silicone ($\mu_a = 0.05$ cm^{-1}, $\mu_s = 5$ cm^{-1}) thickness = 5 mm top layer, Marble bottom layer, $\rho = 0$ mm.

The measurements on phantoms were performed over 10 minutes, but every second we acquired a new base and a set of 32 bases were stored to be later analyzed. We can therefore reconstruct how the resulting data improves with time considering the low counts per second.

From fig. 4.31 and fig. 4.32 we see how the signal improves with the integration time. We see that in the long integration time of the Raman signal of the marble is much more defined than the low integration one. The signal amplitude is expressed in cps and not in total counts. We can easily convert to total count by multiplying by the integration time. We can see that the reconstruction of the low repetition measurement has negative numbers. This is not physical and is caused by the Poisson noise on the different basis of the measurement.

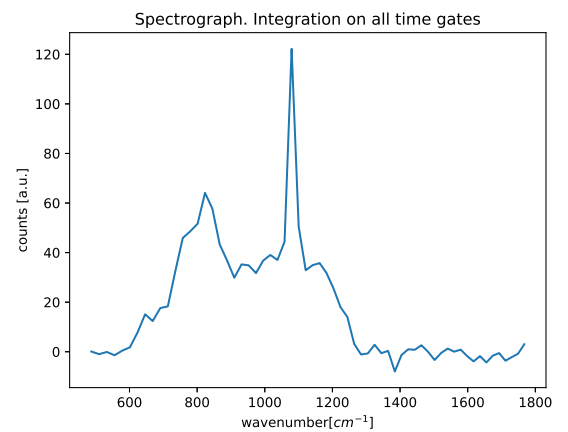**(a)** 1 times repetition per base, integration time = 64 s

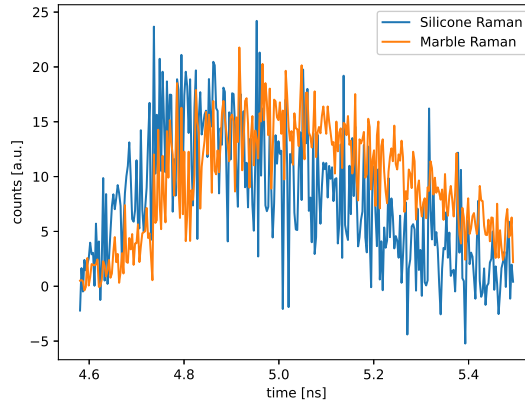**(b)** 2 times repetition per base, integration time =
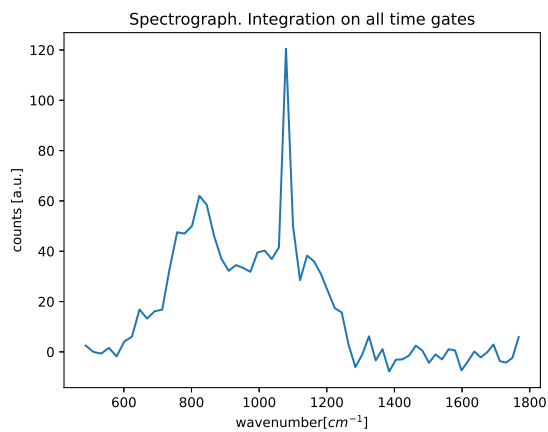
(c) 8 times repetition per base, integration time = 512 s

(d) 16 times repetition per base, integration time =

Figure 4.32: Spectrograph of Different integration time. Silicone ($\mu_a = 0.05\ cm^{-1}$, $\mu_s = 5\ cm^{-1}$) thickness = 5 mm top layer, Marble bottom layer, $\rho = 0$ mm.

Figure 4.33: Comparison of the time distribution of the Raman from Silicone ($\mu_a = 0.05$, $\mu_s = 5$, thickness 5 mm) and Marble

**Estimating the Time speration of the peaks from depth**

Comparing the time distribution of the Raman from the bottom layer to a reference time distribution gives the depth information of the Raman material. In fig. 4.33 we see the comparision of the Raman from the silicone and the Raman from the marble from the measurement presented in fig. 4.28. The peak position of the Raman from the top layer, the silicone, arrives approximately 170 ps earlier than the one from the marble. This is caused by the propagation time inside the material. In chapter 2, we estimated the bilayer green function and found a time delay from the arrival time of the pulse on the first layer of the material to the emission of the Raman signal of the bottom layer from the bilayer phantom. Using this function, we found the expected delay of arrival from the pulse arrival, using parameters for the top layer n = 1.5, $\mu_s = 5\ cm^{-1}$, $\mu_a = 0.05\ cm^{-1}$ and a thickness of 5 mm. The time delay estimated was $t_{max,Bottom} = 440$ ps.

It is possible to estimate the depth by measuring the time delay to a reference curve. The reference curve is from the Raman of the top layer. Using the same parameters, we estimate the position of maximum to be $t_{max,Top} = 110$ ps after the arrival of the pulse. We find the expected time difference of the maximum position for the top Layer marble to the one from the bottom layer to be $\Delta t = t_{max,Bottom} - t_{max,Top} = 330$ ps.

Comparing our estimation to the measured one, we find a difference of 160 ps. We believe this difference is caused by the several approximations that we needed to obtain an analytical solution to the bilayer problem. Another possibility is that some parameters of the silicone phantom (μ_a, μ_s, n) are not correct or the laser had a poor temporal resolution of more than 100 ps of FWHM, causing a poor measurement of the time delay.

4.6.3   In Vivo

A series of in vivo measurements has been performed. First, we performed the measurements on the forearm and hand of a subject to recognize a bone Raman
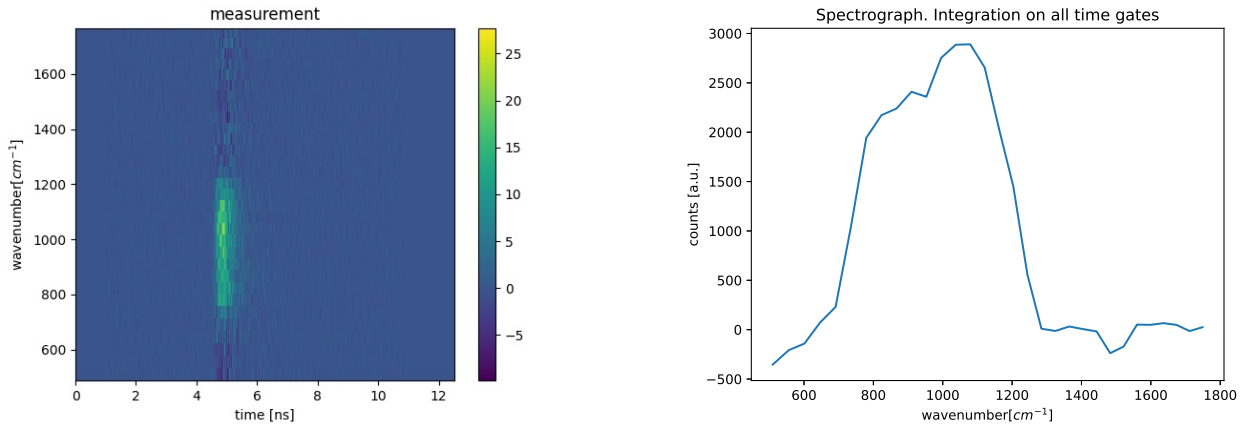
Figure 4.34: forearm, close to bone $\rho = 10$ mm, integration time $= 640$ s
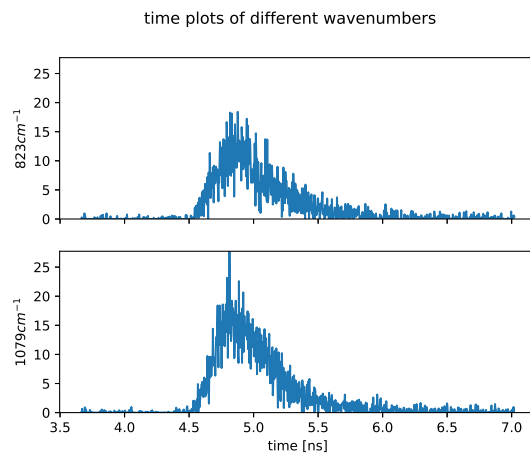
Figure 4.35: forearm, close to bone $\rho = 10$ mm, integration time $= 640$ s, Time scale

fingerprint. We aimed to find the 1086 cm^{-1} Raman shift of the $CaCO_3$ coming from the bone. The measurement are presented in figs. 4.34, 4.36, 4.37 and 4.38. No peak can be recognized in the in vivo case. By focusing on the time-domain in fig.4.35, we can see there is no time shift between the two curves typical of a Raman signal from depth. The in-vivo case is complicated to study. We believe we were not able to measure the 1086 cm^{-1} bone peak because:

- Presence of several Raman emitters on the skin that buried the Raman from the bone.

- Fluorescence of the biological tissue

4.6.4   Improving the system

Some elements should be improved in our system to obtain a higher signal-to-noise ratio.
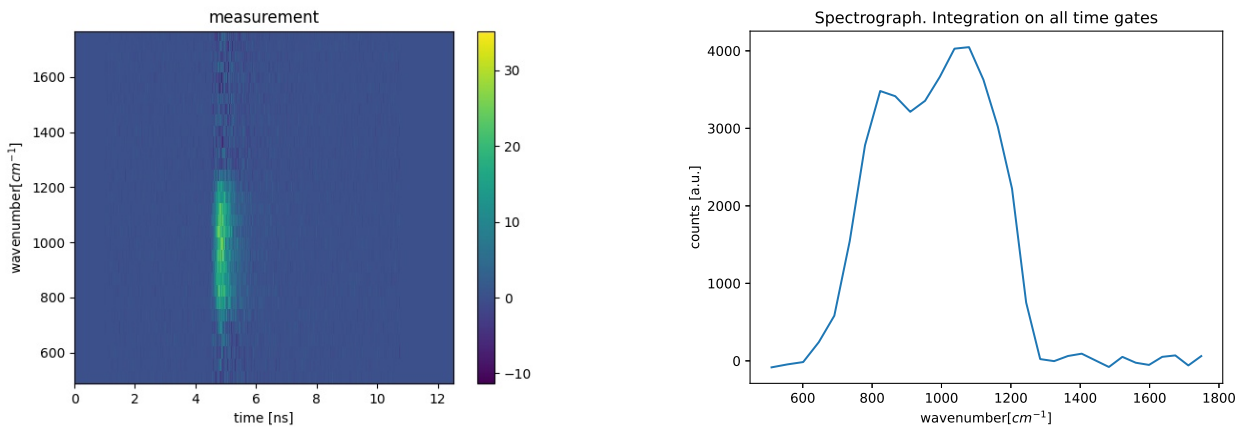
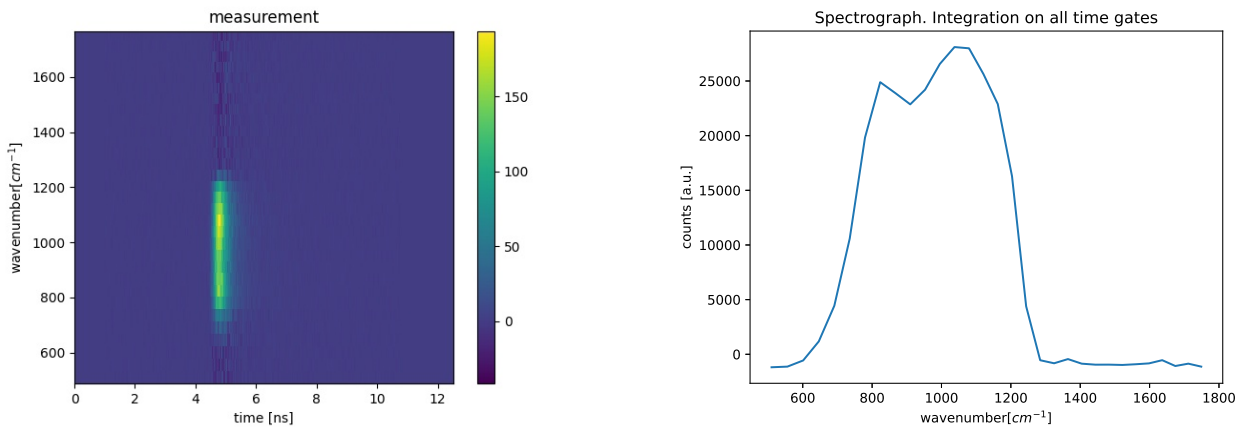**Figure 4.36:** Forearm fat region $\rho = 10$ mm, integration time $= 640$ s

Figure 4.37: Wrist close to bone $\rho = 0$ mm, integration time $= 640$ s
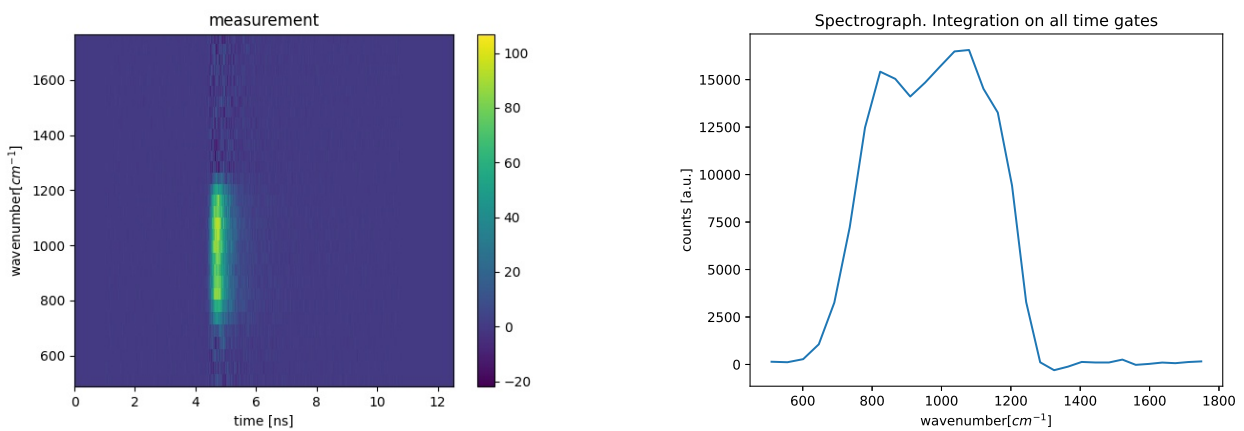

Figure 4.38: Palm hand $\rho = 0$ mm, integration time $= 640$ s

- The critical component was the laser that only functioned at low power for a limited amount of time. For this system, we need high stability, high power and must function for several hours without any problem. To solve this problem, we will have to change the pump laser of the Ti-Sa.

- We should consider using a detector with higher efficiency at higher wavelength and lower time jitter. The main difficulty will be finding a detector with a comparable dimension of the active area and comparable low dark counts.

- we should improve the range and resolution of the system. We could modify the optical system, use the entire area of the DMD, use a grating with a lower number of lines, and use a bundle of monomode fiber with a small core dimension, but this will greatly reduce the photon collection efficiency.

- Increase the numerosity of the basis. The dimension of the line on the DMD has a considerable effect on the resolution of the recovered signal therefore a higher number of bases 128, 256 could help in improving the resolution of the instrument without compromising on the detection efficiency and the integration time.

Finally, a rigorous validation of the two-layer system should be performed where a systematic study where the effect of the following parameters on the recovered Raman spectra:

- Silicone thickness

- Silicone optical properties (μ_a, μ_s)

- probing system, (two-lens system and three lens system)

- illumination shape

4.7   Conclusion

We have improved a Time-domain diffuse Raman spectrometer by finalizing the setup to decrease the noise by adding filters and improving the covering of the setup from unwanted lights, improving the efficiency by optimizing the collection of the fiber and the resolution by building a new DMD mount to place the DMD easily. We improved the usability of the system by developing a custom program to control the DMD.

We measured some bi-layer silicone marble phantoms and demonstrated the ability of the spectrometer to measure a Raman signal coming from 10 mm of silicone thickness. This work had as aim an in-vivo measurement that was performed, but we were not able to measure any Raman signal coming from depth.

We finally presented some possible improvements for the setup.

Chapter 5

Conclusion

The thesis consisted of a theoretical part and the development of two types of time-domain single-pixel Raman spectrometers.

The theoretical chapter aimed to explain how the Raman signal propagates inside a media, its temporal profile and its spatial distribution.

The first spectrometer for was reflectance Raman. It made use of a single-mode fiber to separate the wavelengths. The second was a diffuse Raman spectrometer for detecting a Raman signal coming from the depth of a sample and used compressive sensing techniques to improve collection speed.

Theory

In the theoretical chapter, we wanted to explain the propagation of a Raman signal inside a material. We found a parallel approach to find the Green function from the method presented by ref. [26] and by approximating the problem into a ring illumination, we estimated the fluency, finding that the source detection separation acts as a time-gate. We estimated the photons collected by a fiber and found that the Raman light has a larger spatial distribution than the elastic Light, proportionally to the signal intensity.

We finally tried to explain the Raman propagation from a bi-layer. The problem is complicated and required several approximations, but we found a possible Green function. In particular, we found and estimated a time delay from the pulse arrival on the first layer to the reflection of the Raman signal of the bottom layer.

WTT spectrometer

A new type of Raman spectrometer has been developed, using the wavelength dispersion in a fiber to separate two pulsed wavelengths and a single-pixel superconductive nano-wire detector.

The spectrometer has a low collection diameter of $40\mu m$ and numerical aperture of 0.1 but has a very high collection efficiency of 80% in the 780 to 950 nm region. The resolution measured on the system was 1.5 nm. A clear Raman spectra can be reconstructed with 20 mW of laser power and 100 s integration time on marble.

We have successfully measured several Raman spectra with this new approach and compared them to the previous method presented in ref. [22] we had several key improvements:

- higher efficiency of the spectrometer. In the operational range of 780 to 1100 nm we had around 80% of efficiency compared to the reported 1%

- higher spectral resolution of 1.5 nm compared to 3 nm reported and limited by the laser that was not Fourier limited.

- we performed a different method for calibrating the spectrometer independent of the sample measured.

- Several measurements have been performed on different types of plastics, lard, Marble, Silicone, calcium carbonate and hydroxyapatite

- Some in vivo measurement has been performed

The resolution of the setup can be significantly improved using a Fourier Limited laser with both high temporal and spectral resolution.

This method could be successfully used for a Raman camera if multiple detectors are used or as a Raman spectrometer if a large bundle of monomode fibers is used instead of a single monomode fiber on a larger detection area.

If a SPAD is used instead of a superconductive nano-wire detector, this type of spectrometer could be used in environments where space or weight are a constraint.

Time Domain Diffuse Raman spectrometer

The second setup is a time-domain diffuse-Raman spectrometer that makes use of time-domain techniques for depth probing. The spectrometer uses a single-pixel detector. It can parallelly record multiple wavelengths for an improved acquisition time via compressive sensing techniques.

We improved an existing time-domain diffuse Raman spectrometer by optimizing the optical setup, writing a new program to control the DMD, building a new setup for fine-tuning the DMD and adding the DMD - TCSPC board synchronization for fast measurement. Moreover, compressive sensing significantly improved the integration time while maintaining unchanged the resolution of the spectrometer.

The maximum resolution possible with the current setup is 1.9 nm. The spectral range of the system is 45 nm. Compared to the previous system, we have twice the detection efficiency. A new complete measurement can be acquired with a 1 Hz frequency.

The measurements had been performed on a Silicone marble bi-layer phantom. The silicone was placed on top of the marble and we tried to measure the Raman coming from the bottom layer, the marble. Some notable results are with thickness of 10 mm $\rho = 0$ mm Silicone ($\mu_a = 0.05cm^{-1}$, $\mu_s = 5cm^{-1}$) with a 600 s integration time it was possible to clearly recognize the Marble Raman signal.

Notably, in the data analysis, we were able to reconstruct a spectrum with the Silicone ($\mu_a = 0.05cm^{-1}$, $\mu_s = 5cm^{-1}$) of thickness = 5 mm, $\rho = 0$ mm after an integration of just 64 s we were able to recognize the Marble fingerprint.

From the bi-layer, we observed a time separation between the Raman peak from the silicone of the top layer and the Raman signal from the marble of the bottom layer. We validated the temporal separation that has been found in the theoretical

chapter. From this temporal separation, if a higher signal-to-noise ratio is available it will be possible to reconstruct the depth origin of the signal.

Some initial in-vivo measurements were performed, but we have not been able to reconstruct any Raman peak from the measurement due to the high presence of fluorescence.

The following steps in developing this spectrometer are a more rigorous validation on silicone phantom and proceeding then on meat phantoms with the final aim of measuring the bone signature from an in-vivo subject and with the final objective of using this type of spectrometer in clinics for disease monitoring and prevention.

Bibliography

[1] *ATKINS' PHYSICAL CHEMISTRY*. Tech. rep. (cit. on pp. 2, 4).

[2] Kalyan Ram Ayyalasomayajula and Phaneendra K. Yalavarthy. "Analytical solutions for diffuse fluorescence spectroscopy/imaging in biological tissues Part II: comparison and validation". In: *Journal of the Optical Society of America A* 30.3 (2013), p. 553. ISSN: 1084-7529. DOI: 10.1364/josaa.30.000553 (cit. on p. 15).

[3] R. Baker et al. "New relationships between breast microcalcifications and cancer". In: *British Journal of Cancer* 103.7 (2010), pp. 1034–1039. ISSN: 00070920. DOI: 10.1038/sj.bjc.6605873 (cit. on p. 13).

[4] Wolfgang Becker. "High Speed Hybrid Detector for TCSPC GaAsP cathode : HPM-100-50". In: March (2010) (cit. on pp. 66, 67).

[5] Wolfgang Becker. "The bh TCSPC Handbook-7th ed". In: *Scanning* 800 (2010), pp. 1–566. URL: http://www.becker-hickl.de/handbook.htm (cit. on pp. 8, 66, 75).

[6] Pascal Berto et al. "Programmable single-pixel-based broadband stimulated Raman scattering". In: *Optics Letters* 42.9 (2017), p. 1696. ISSN: 0146-9592. DOI: 10.1364/ol.42.001696 (cit. on pp. 65, 67).

[7] Matthew Bloomfield et al. "Non-invasive identification of incoming raw pharmaceutical materials using Spatially Offset Raman Spectroscopy". In: *Journal of Pharmaceutical and Biomedical Analysis* 76 (2013), pp. 65–69. ISSN: 07317085. DOI: 10.1016/j.jpba.2012.11.046 (cit. on p. 12).

[8] Alessandra Botteon et al. "Discovering Hidden Painted Images: Subsurface Imaging Using Microscale Spatially Offset Raman Spectroscopy". In: *Analytical Chemistry* 89.1 (2017), pp. 792–798. ISSN: 15206882. DOI: 10.1021/acs.analchem.6b03548 (cit. on p. 12).

[9] Kevin Buckley et al. "Raman spectroscopy reveals differences in collagen secondary structure which relate to the levels of mineralisation in bones that have evolved for different functions". In: *Journal of Raman Spectroscopy* 43.9 (2012), pp. 1237–1243. ISSN: 03770486. DOI: 10.1002/jrs.4038 (cit. on p. 13).

[10] G. Inzani C. Barri. "Appunti di Scienza e Tecnologia dei Materiali". In: *Course: Scienza e Tecnologia dei Materiali by Chiara Castiglioni*. 2016 (cit. on p. 2).

[11]   M Natarajan Chandra, G Tanner Michael, and H Hadfield Robert. "Super-
       conducting nanowire single-photon detectors: physics and applications". In:
       Superconductor Science and Technology 25.6 (2012), p. 63001. URL: http:
       //stacks.iop.org/0953-2048/25/i=6/a=063001 (cit. on p. 46).

[12]   Harikumar K. Chandrasekharan et al. "Multiplexed single-mode wavelength-
       to-time mapping of multimode light". In: *Nature Communications* 8 (2017),
       pp. 1–10. ISSN: 20411723. DOI: 10.1038/ncomms14080. arXiv: 1604.02495
       (cit. on pp. 33, 34).

[13]   Chunsik Choe et al. "Keratin-water-NMF interaction as a three layer model
       in the human stratum corneum using in vivo confocal Raman microscopy". In:
       Scientific Reports 7.1 (2017), pp. 1–14. ISSN: 20452322. DOI: 10.1038/s41598-
       017-16202-x (cit. on p. 60).

[14]   Jennifer-Lynn H Demers et al. *Raman spectroscopy*. Tech. rep. 3. 1992,
       pp. 2000–2004 (cit. on p. 13).

[15]   *DLPC900 Programmer's Guide Programmer's Guide*. Tech. rep. 2014. URL:
       www.ti.com (cit. on pp. 73–75).

[16]   C. Eliasson, N. A. Macleod, and P. Matousek. "Non-invasive detection of
       powders concealed within diffusely scattering plastic containers". In: *Vibra-
       tional Spectroscopy* 48.1 (2008), pp. 8–11. ISSN: 09242031. DOI: 10.1016/j.
       vibspec.2008.01.017 (cit. on p. 12).

[17]   Hamamatsu. *Hamamatsu S16010-1006 Datasheet*. URL: https://www.hamamatsu.
       com/resources/pdf/ssd/s16010_series_kmpd1126e.pdf (cit. on p. 53).

[18]   Michael D. Hargreaves et al. "Application of portable Raman spectroscopy
       and benchtop spatially offset Raman spectroscopy to interrogate concealed
       biomaterials". In: *Journal of Raman Spectroscopy* 40.12 (2009), pp. 1875–1880.
       ISSN: 03770486. DOI: 10.1002/jrs.2335 (cit. on p. 12).

[19]   Naiyan Huang et al. "Full range characterization of the Raman spectra of
       organs in a murine model". In: *Optics Express* 19.23 (2011), p. 22892. ISSN:
       1094-4087. DOI: 10.1364/oe.19.022892 (cit. on p. 60).

[20]   Texas Instruments. "DLP6500 0 . 65 1080p MVSP Type A DMD". In: (2016)
       (cit. on pp. 67, 78).

[21]   Michael Jermyn et al. "Highly accurate detection of cancer in situ with intra-
       operative, label-free, multimodal optical spectroscopy". In: *Cancer Research*
       77.14 (2017), pp. 3942–3950. ISSN: 15387445. DOI: 10.1158/0008-5472.CAN-
       17-0668 (cit. on p. 14).

[22]   Julia Toussaint, Sebastian Dochow, and Ines Latka. "Proof of concept of fiber
       dispersed Raman spectroscopy using superconducting nanowire single-photon
       detectors". In: *Microscopy Research and Technique* 63.1 (2004), pp. 58–66.
       ISSN: 1059910X. DOI: 10.1002/jemt.10421 (cit. on p. 105).

[23]   S. Konugolu Venkata Sekar et al. "Time domain diffuse Raman spectrometer
       based on a TCSPC camera for the depth analysis of diffusive media". In: *Optics
       Letters* 43.9 (2018), p. 2134. ISSN: 0146-9592. DOI: 10.1364/ol.43.002134
       (cit. on p. 11).

[24] María López-López and Carmen García-Ruiz. *Infrared and Raman spectroscopy techniques applied to identification of explosives*. 2014. DOI: `10.1016/j.trac.2013.10.011` (cit. on p. 12).

[25] Fabrizio Martelli et al. "Photon Migration Through Diffusive Media: Theory, Solutions, and Software". In: *Spie Book* (2010), p. 1365 (cit. on pp. 6, 7, 15, 24).

[26] Fabrizio Martelli et al. "Time-domain Raman analytical forward solvers". In: *Optics Express* 24.18 (2016), p. 20382. ISSN: 1094-4087. DOI: `10.1364/oe.24.020382` (cit. on pp. 15, 17, 32, 105).

[27] P Matousek et al. *Depth Profiling in Diffusely Scattering Media Using Raman Spectroscopy and Picosecond Kerr Gating*. Tech. rep. 2. 2005 (cit. on p. 11).

[28] P Matousek et al. *Subsurface Probing in Diffusely Scattering Media Using Spatially Offset Raman Spectroscopy*. Tech. rep. 4. 2005 (cit. on pp. 9, 10).

[29] Pavel Matousek. *Spatially offset Raman spectroscopy for non-invasive analysis of turbid samples*. 2018. DOI: `10.1016/j.trac.2018.04.002` (cit. on p. 10).

[30] Pavel Matousek and Nicholas Stone. *Development of deep subsurface Raman spectroscopy for medical diagnosis and disease monitoring*. 2016. DOI: `10.1039/c5cs00466g` (cit. on p. 10).

[31] Pavel Matousek and Nicholas Stone. *Recent advances in the development of Raman spectroscopy for deep non-invasive medical diagnosis*. 2013. DOI: `10.1002/jbio.201200141` (cit. on p. 10).

[32] Zhaokai Meng et al. "Lightweight Raman spectroscope using time-correlated photon-counting detection". In: *Proceedings of the National Academy of Sciences of the United States of America* 112.40 (2015), pp. 12315–12320. ISSN: 10916490. DOI: `10.1073/pnas.1516249112` (cit. on p. 33).

[33] Gianmaria Calisesi Michele Castriotta Andrea Bassi. *DMD ScopeFoundry*. URL: `https://github.com/micropolimi/DMDScopeFoundry` (cit. on p. 72).

[34] Sara Mosca et al. "Spatially offset Raman spectroscopy". In: *Nature Reviews Methods Primers* 1.1 (2021). ISSN: 2662-84492662-8449. DOI: `10.1038/s43586-021-00019-0`. URL: `http://dx.doi.org/10.1038/s43586-021-00019-0` (cit. on pp. 9, 10, 12).

[35] Antonio Pifferi et al. "New frontiers in time-domain diffuse optics, a review". In: *Journal of Biomedical Optics* 21.9 (2016), p. 091310. ISSN: 1083-3668. DOI: `10.1117/1.jbo.21.9.091310` (cit. on p. 8).

[36] Paolo Pozzi. *Pycrafter 6500*. URL: `https://github.com/csi-dcsc/Pycrafter6500` (cit. on p. 72).

[37] PublicSpectra. *Raman Spectrum of Polysterene*. URL: `https://publicspectra.com/Raman/Polystyrene` (cit. on p. 60).

[38] Jianwei Qin, Kuanglin Chao, and Moon S. Kim. "Investigation of Raman chemical imaging for detection of lycopene changes in tomatoes during postharvest ripening". In: *Journal of Food Engineering* 107.3-4 (2011), pp. 277–288. ISSN: 02608774. DOI: `10.1016/j.jfoodeng.2011.07.021` (cit. on p. 12).

[39] Single Quantum. *Single Quantum Iris-S19 Datasheet*. URL: https://singlequantum.com/wp-content/uploads/2019/05/Single-Quantum-Eos.pdf (cit. on pp. 47, 50).

[40] KRISHNAN K. S RAMAN C. V. "A New Type of Secondary Radiation". In: (1928) (cit. on p. 4).

[41] Lord Rayleigh. "On the transmission of light through an atmosphere containing small particles in suspension, and on the origin of the blue of the sky". In: (1899) (cit. on p. 4).

[42] Sanathana Konugolu Venkata Sekar et al. "Frequency offset Raman spectroscopy (FORS) for depth probing of diffusive media". In: *Optics Express* 25.5 (2017), p. 4585. ISSN: 1094-4087. DOI: 10.1364/oe.25.004585 (cit. on p. 11).

[43] Karen E. Shafer-Peltier et al. "Raman microspectroscopic model of human breast tissue: Implications for breast cancer diagnosis in vivo". In: *Journal of Raman Spectroscopy* 33.7 (2002), pp. 552–563. ISSN: 03770486. DOI: 10.1002/jrs.877 (cit. on p. 13).

[44] Ewen Smith and Geoffrey Dent. *Modern Raman Spectroscopy-A Practical Approach*. Tech. rep. (cit. on p. 5).

[45] Nicholas Stone et al. "Subsurface probing of calcifications with spatially offset Raman spectroscopy (SORS): Future possibilities for the diagnosis of breast cancer". In: *Analyst* 132.9 (2007), pp. 899–905. ISSN: 00032654. DOI: 10.1039/b705029a (cit. on p. 14).

[46] Thorlab. *Thorlabs' 780-HP Spec Sheet*. URL: https://www.thorlabs.com/drawings/e156eb079f3e4341-D2D07ABF-B638-82BD-2FAE88DF663FC419/780HP-SpecSheet.pdf (cit. on p. 46).

[47] Thorlabs. *GIF50C - Graded-Index Multimode Fiber Spec Sheet*. URL: https://www.thorlabs.com/_sd.cfm?fileName=21947-S01.pdf&partNumber=GIF50C (cit. on p. 46).

[48] Xiao Yu et al. "Super Sub-Nyquist Single-Pixel Imaging by Total Variation Ascending Ordering of the Hadamard Basis". In: *Scientific Reports* 10.1 (2020), pp. 1–11. ISSN: 20452322. DOI: 10.1038/s41598-020-66371-5 (cit. on p. 68).